Nonlinear Optical Waves in Disordered Ferroelectrics

Candidate

Davide Pierangeli

ID number 1361119

Thesis Advisor

Prof. Eugenio Del Re

A thesis submitted in partial fulfillment of the requirements for the degree of Doctor of Philosophy in Physics

December 2016

Thesis defended on 17 February 2017
in front of a Board of Examiners composed by:

Prof. Mauro Carfora (chairman)
Prof. Sergio Caracciolo
Prof. Antonello Scardicchio

This thesis has been typeset by LATEX and the Sapthesis class.

Version: January 20, 2017

Author's email: pierangelidavide@hotmail.com; davide.pierangeli@roma1.infn.it

List of publications associated with this thesis

D.Pierangeli, M.Ferraro, F.Di Mei, G.Di Domenico, C.E.M.de Oliveira, A.J.Agranat and E.DelRe, Super-crystals in composite ferroelectrics, ***Nat. Commun.*** **7**, 10674 (2016).

D.Pierangeli, F.Di Mei, C.Conti, A.J.Agranat, and E.DelRe, Spatial Rogue Waves in Photorefractive Ferroelectrics, ***Phys. Rev. Lett.*** **115**, 093901 (2015).

D.Pierangeli, F.Di Mei, G.Di Domenico, A.J.Agranat, C.Conti, and E.DelRe, Turbulent transitions in optical wave propagation, ***Phys. Rev. Lett.*** **117**, 183902 (2016).

F.DiMei, P.Caramazza, D.Pierangeli, G.Di Domenico, H.Ilan, A.J.Agranat, P.Di Porto, and E.DelRe, Intrinsic negative mass from nonlinearity, ***Phys. Rev. Lett.*** **116**, 153902 (2016).

D.Pierangeli, M.Flammini, F.Di Mei, J.Parravicini, C.E.M.de Oliveira, A.J.Agranat, and E. DelRe, Continuous Solitons in a Lattice Nonlinearity, ***Phys. Rev. Lett.*** **114**, 203901 (2015).

D.Pierangeli, G.Musarra, F.Di Mei, G.Di Domenico, A.J.Agranat, C.Conti, and E.DelRe, Enhancing optical extreme events through input wave disorder, ***Phys. Rev. A*** **94**, 063833 (2016).

D.Pierangeli, F.Di Mei, J.Parravicini, GB.Parravicini, A.J.Agranat, C.Conti, and E.DelRe, Observation of an intrinsic nonlinearity in the electro-optic response of freezing relaxors ferroelectrics, ***Opt. Mater. Express*** **4**, 1487 (2014).

F.Di Mei, D.Pierangeli, J.Parravicini, C.Conti, A.J.Agranat, and E.DelRe, Observation of diffraction cancellation for nonparaxial beams in the scale-free-optics regime, ***Phys. Rev. A*** **92**, 013835 (2015).

F.Di Mei, J.Parravicini, D.Pierangeli, C.Conti, A.J.Agranat and E.DelRe, Anti-diffracting beams through the diffusive optical nonlinearity, ***Opt. Express*** **22**, 31434 (2014).

List of supplementary publications

D.Pierangeli, J.Parravicini, F.Di Mei, GB.Parravicini, A.J.Agranat, and E.DelRe, Photorefractive light needles in glassy nanodisordered KNTN, ***Opt. Lett.*** **39**, 1657 (2014).

J.Parravicini, D.Pierangeli, F.Di Mei, A.J.Agranat, C.Conti, and E.DelRe, Aging solitons in photorefractive dipolar glasses, ***Opt. Express*** **21**, 30573 (2013).

J.Parravicini, R.Martinez Lorente, F.Di Mei, D.Pierangeli, A.J.Agranat, and E.DelRe, Volume integrated phase modulator based on funnel waveguides for reconfigurable miniaturized optical circuits, ***Opt. Lett.*** **40**, 1386 (2015).

J.Parravicini, F.Di Mei, D.Pierangeli, A.J.Agranat, and E.DelRe, Miniaturized electro-optic infrared beam-manipulator based on 3D photorefractive funnels, ***J. Opt.*** **17**, 055501 (2015).

Abstract

This thesis describes an experimental, numerical and theoretical investigation of nonlinear optical phenomena in disordered photorefractive ferroelectrics in proximity of their phase-transition temperature. The work addresses different physical issues that find in nonlinear optics a common fertile research arena and are closely related to each other in the considered systems. Nonlinear wave dynamics in the spatial domain, where self-interaction of propagating waves generally results into non-spreading localized wavepackets such as spatial solitons, is extended in photorefractive ferroelectrics to non-equilibrium regimes characterized by stochastic instabilities and large material fluctuations. We discover the emergence of rogue waves, localized perturbations of abnormal intensity, whose understanding is challenging in various physical contexts and resides in the general problem of long-tail statistical distributions in complex systems. We identify their origin in spatiotemporal soliton dynamics in a saturable nonlinearity which can support scale-invariant waveforms. Properties and predictability of the observed extreme events are investigated, and, in particular, we demonstrate their active control through the spatial incoherence scale of the optical field. Moreover, we report how their emergence is sustained by turbulent transitions to an incoherent and disordered optical state triggered by modulational instability. The onset of strong turbulence for propagating optical waves has remained unobserved up to now and our results demonstrate a new experimental setting for its study. When the functional form of the nonlinearity is turned into a nonlocal one due to diffusive fields, this setting also exploits photonics to address fundamental physical problems and access to otherwise hidden phenomena. The natural spreading of waves during propagation, representing the wavelength-defined ultimate limit to spatial resolution, can be eliminated and reversed leading to diffraction cancellation and anti-diffraction of light. Since these behaviors on modifying the nature of underlying Schrödinger equation, we are the first to demonstrate how nonlinearity can make the spatial light distribution behave as the wavefunction of a quantum particle with negative mass. All these findings have roots in the nonlinear optical response of critical disordered ferroelectric crystals, which are also extremely interesting from the condensed matter point of view. In fact, competition of different microscopic structural phases and the associated polar-domain dynamics at the nanoscale results into non-ergodic dipolar-glass behaviors giving giant responses such as giant polarization, piezoelectricity and electro-optic effect. Disordered ferroelectrics crystals are investigated electro-optically across their ferroelectric phase-transition, where we report the observation of an anomalous electro-optic effect compatible with ultracold dipolar reorientation. In compounds presenting spatial inhomogeneity in their chemical composition, we discover a new ferroelectric phase of matter in which polar domains spontaneously coordinate into a mesoscopic coherent polarization super-crystals. This phase mimics standard solid-state structures but on scales that are thousands of times larger and represent the first spontaneous three-dimensional photonic crystal.

The thesis is structured in two main parts. The first one presents achievements in the electro-optic response and dipolar phases of critical disordered ferroelectric

crystals. The second reports results in spatial nonlinear wave dynamics supported by photorefraction in these media. The main experimental findings, together with numerical analysis and some novel theoretical approaches, are uniformly presented and connected to relevant studies in the various research areas according to the following chapters. Chapter 1 introduces the general context, the basic physical mechanisms and methods on which rely most of the phenomena investigated. In particular, photorefraction and nonlinear wave equations leading to photorefractive solitons are derived. Chapter 2 and Chapter 3 reports original experimental results on the electro-optic response of potassium-sodium-tantalate-niobate (KNTN) and potassium-lithium-tantalate-niobate (KLTN) single crystals in proximity of their ferroelectric phase transition. An anomalous electro-optic effect is observed and modelled in Chapter 2, whereas in Chapter 3 is described the discovery of spontaneous polarization super-crystals in microstructured samples. Chapter 4 reports the first observation of spatial rogue waves in photorefractive ferroelectrics. Experimental results are corroborated by numerical simulations of beam propagation in highly-nonlinear regimes and the first key points for their understanding are pointed out. Predictability of the observed extreme events is also addressed using analysis methods typical of nonlinear dynamical systems. In Chapter 5 evidence of turbulent transitions in optical wave propagation is reported. We study shot-to-shot fluctuations and correlations in the modulation instability process triggering the transition and in the incoherent optical turbulent regime supporting rogue waves. In Chapter 6 control of optical extreme events through spatial incoherence is demonstrated. This allows us to present the full understanding of abnormal waves in spatial propagation in terms of turbulent dynamics of non-stationary solitons. Chapter 7 describes the theory of scale-free optics and light anti-diffraction in diffusive nonlinearities, with experiments in photorefractives through which we demonstrate the phenomena from paraxial to sub-wavelength beam propagation regimes. In Chapter 7 we show through experiments, theory and numerics how anti-diffracting nonlinear waves evolving into an optical potential made by an integrated slab waveguide give rise to the dynamics of a negative-mass quantum particle.

Acknowledgments

Contents

Chapter 1

Beam propagation in photorefractive media

In this Chapter the general concept of nonlinear wave is briefly introduced and applied in detail to optical spatial propagation in photorefractive media. We present the photorefractive mechanism and the physics of photorefractive solitons, that is the basic physics on which rely part of the phenomena investigated in this thesis, focusing our attention on the specific aspects that characterize the experimental activity and the understanding of the results. The novel case of spatial solitons in a lattice nonlinearity, that we have recently introduced and addressed in this context [217], is also illustrated.

1.1 Introduction

Nonlinear phenomena are natural manifestations of a physical system whose evolution cannot be described in terms of oscillations around an equilibrium point. Generally, the dynamics of a system near a stationary configuration is studied expanding the relevant physical quantities around that equilibrium condition. This gives linear differential model equations, from which emerges the fundamental notion of normal mode as suitable concept to describe the dynamics. Due to the linearity of the system, any solution can be expressed as a superposition of its normal modes. Moreover, the system evolution when it is excited through a localized perturbation leads to the broadening of its own structure, since each mode is characterized by a specific eigenvalue or phase velocity. In optics this fact gives the diffraction and dispersion phenomena. On the contrary, when interactions in the system have energies comparable to that binding it in equilibrium, nonlinear phenomenology arises. Different modes can be made to interact and energy and momentum can be transferred from one mode to the other (wave-mixing) [44]. When the interaction strength is so large that also the concept of mode comes less, the system behavior can be understood only as a collective response, through universal physical entities constituted from elementary components but without an analogous in linear theories. Solitons [2, 3] and shock waves [296, 139, 117, 72, 116, 301] are the most important ones. Optical solitons are highly-localized electromagnetic perturbations that propagate in the supporting medium without spreading their

spatial or temporal structure [148]. In fact, nonlinear interaction exactly balances the dispersive character of the pulse. In the spatial domain they appear as self-trapped beams that remain localized transversely to the propagation direction [277, 60]. They arise as the optical intensity is able to change the index of refraction spatial distribution of the medium, a process generally referred to as Kerr effect and governed in centrosymmetric media by the susceptibility tensor $\chi^{(3)}$ [44]. Since the index variation is a function of the intensity itself, the soliton formation mechanism can be understood as light self-interaction: the optical beam modifies the hosting material, whose response changes beam propagation as to compensate its delocalization. The wave induces a waveguide and concomitantly is a guided mode of its own waveguide, whose stability strongly depends on the specific case considered. Hereafter all this picture is described for waves interacting through a saturable nonlinearity, as the one occurring in photorefractive media [245].

1.2   Photorefractive propagation

The photorefractive effect is the self-local modulation of the refractive index of a medium traversed by a light beam [21], a process occurring in materials manifesting both photoconductivity and electro-optic response [304, 129]. In these media interaction with optical radiation leads to local charge separation, with the corresponding generation of a space-charge field that modulates the index of refraction via an electro-optic effect induced by the electromagnetic field. As the resulting nonlinearity depends on the transport properties of the free carriers excited in the materials, it cannot be described in terms of a generic susceptibility tensor $\chi^{(m)}$ that implies a series expansion of the polarizability with respect to the optical field. However, this nonlinearity can support extensive nonlinear wave dynamics and different kinds of spatial optical solitons through different underlying mechanisms. Although a general approach is given, our interest is dedicated to self-focusing dynamics in centrosymmetric media.

1.2.1   Band-transport model

The standard model of photorefraction is based on semiclassical nonlinear rate equations [157]. The main properties pointed out by this approach are a substantial dependence from material impurities, slow response times $(10^{-3} - 10^2 s)$ and non-local features. As shown in Fig. 1.1, we consider a dielectric medium with deep donor impurities density N_D and acceptor impurities density N_A, with $N_D \gg N_A$. Light of wavelength λ excites locally free carriers that are subject to drift and diffusion fields and then recombines with acceptor impurities. As a result of this average response, a difference in charge distribution between bright and dark region is generated, with the corresponding electric field acting on the illuminated area. The dynamics of the system under the intensity flux $I(r,t)$ is described by the effective rate equation

$$\frac{\partial N_d^+}{\partial t} = (\beta + sI)(N_d - N_d^+) - \gamma N_e N_d^+, \tag{1.1}$$

where $N_d^+ = N_d^+(r,t)$ is the ionized donors density, $N_e = N_e(r,t)$ the local concentration of free carriers in the conduction band, β the thermal excitation rate, s the

photo-ionization coefficient associated with the absorption cross-section and γ is the electron-donor recombination constant. Under the hypothesis that the average carrier motion occurs on temporal scales much larger than the ones related to the electron free path, drift and diffusion processes gives the macroscopic electric current density

$$\mathbf{J}(r,t) = q\mu N_e \mathbf{E} + k_b T \mu \nabla N_e, \tag{1.2}$$

where q is the electronic charge, μ the electronic mobility, k_b the Boltzman constant, T the system temperature and $\mathbf{E} = \mathbf{E}(r,t)$ the quasi-static electric field distribution. The second term in Eq. (1.2) represents the diffusive current according with the Einstein relation $D = k_b T \mu / q$. The above relations are connected through the continuity equation,

$$\frac{\partial \rho}{\partial t} + \nabla \cdot \mathbf{J} = 0, \tag{1.3}$$

with the average charge density distribution ρ determined by

$$\rho = q(N_d^+ - N_a - N_e). \tag{1.4}$$

The electric field satisfies the Maxwell equations

$$\begin{cases} \nabla \cdot (\varepsilon \mathbf{E}) = \rho, \\ \nabla \times \mathbf{E} = 0. \end{cases} \tag{1.5}$$

The solution for the above set of nonlinear equations gives the field $\mathbf{E}$ that rules the nonlinearity acting on the optical beam. However, the system is not analytically solvable and a several approximations are needed. We address the issue in the next subsection through the space-charge field approach [80, 86]. In this regard, we note that two different time scales come into play: the free carriers recombination time, $\tau_r = 1/(N_a \gamma)$, and the dielectric relaxation time $\tau_d = \varepsilon/(q\mu N_e)$. In fact, τ_r takes into account local excitation events, whereas τ_d is related to the macroscopic dielectric response and is the average time needed to screen an arbitrary electric field distribution inside the material. Generally, it is $\tau_d \gg \tau_r$, so that the microscopic process can be considered at equilibrium with $\partial N_d^+/\partial t = 0$. Equation (1.1) therefore becomes

$$(\beta + sI)(N_d - N_d^+) \simeq \gamma N_e N_d^+. \tag{1.6}$$

Moreover, the scale τ_d is the basis of the temporal nonlocality characterizing nonlinear waves in photorefractives. Since N_e is proportional to the optical intensity, the relation between τ_d and N_e implies that the stationary state is reached in a characteristic time $\tau \propto 1/I$.

1.2.2   Self-induced space-charge field

We now derive from the band-transport model a single nonlinear equation relating the induced space-charge field $\mathbf{E}$ with the intensity distribution I. The first assumption, based on the typical experimental conditions, is the low intensity regime, in which N_e satisfies the condition $N_e \ll N_d, N_a$. Using Eq. (1.2) and the first relation of Eq. (1.5), $\mathbf{J}$ can be rewritten as

$$\nabla \cdot \left[\varepsilon \frac{\partial \mathbf{E}}{\partial t} + q\mu N_e \mathbf{E} + \mu k_b T \nabla N_e\right] = 0. \tag{1.7}$$
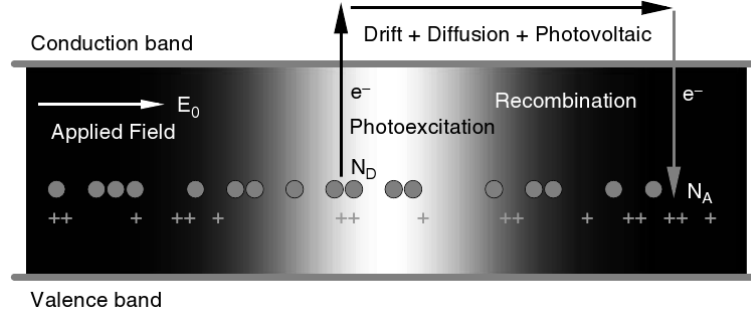
Figure 1.1. Band structure scheme and physical mechanism of charge separation in the standard model of the photorefractive effect. (From [129]).

The first Maxwell equation can also be exploited in Eq. (1.4) to have

$$
N_d^+ = N_e + N_a \left[1 + \nabla \cdot \left(\frac{\varepsilon \mathbf{E}}{q N_a} \right) \right],
\tag{1.8}
$$

in which N_e can be neglected respect to the second term. Substituting it in Eq. (1.6), the carriers density in the conduction band reads

$$
N_e = \frac{(\beta + sI)}{\gamma} \left[\frac{N_d - N_d^+}{N_d^+} \right],
\tag{1.9}
$$

that, through Eq. (1.8) for N_d^+, can be finally expressed as

$$
N_e = \frac{(\beta + sI)}{\gamma} \left[\frac{\frac{N_d - N_a}{N_a} - \nabla \cdot \left(\frac{\varepsilon \mathbf{E}}{q N_a} \right)}{1 + \nabla \cdot \left(\frac{\varepsilon \mathbf{E}}{q N_a} \right)} \right].
\tag{1.10}
$$

Introducing the parameter $\alpha = \frac{N_d - N_a}{N_a}$ ($\alpha \gg 1$) and substituting it in Eq. (1.7), we obtain the implicit equation for the space-charge field as a function of the optical intensity

$$
\begin{aligned}
\nabla \cdot \Bigg[\frac{\gamma \varepsilon}{q \mu s \alpha} \frac{\partial \mathbf{E}}{\partial t} &+ \mathbf{E}(\beta/s + I) \frac{1 - \frac{\nabla \cdot (\varepsilon \mathbf{E})}{\alpha q N_a}}{1 + \frac{\nabla \cdot (\varepsilon \mathbf{E})}{q N_a}} \\
&+ \frac{k_b T}{q} \nabla \cdot \left((\beta/s + I) \frac{1 - \frac{\nabla \cdot (\varepsilon \mathbf{E})}{\alpha q N_a}}{1 + \frac{\nabla \cdot (\varepsilon \mathbf{E})}{q N_a}} \right) \Bigg] = 0,
\end{aligned}
\tag{1.11}
$$

where $\beta/s \equiv I_d$ is the dark intensity, the light-independent thermal contribution to the ionization process. This term is generally included in the background intensity I_b, which take into account all the secondary illuminations on the material. The dielectric constant ε is referred at zero frequency since Eq. (1.11) holds on the time scales where the dielectric response is quasi-static. As $\alpha \gg 1$, the first term of Eq. (1.11) is negligible, so that in the quasi-stationary case ($\partial \mathbf{E}/\partial t \approx 0$) we have

$$
\mathbf{E}(I_b + I) \frac{1}{1 + \frac{\nabla \cdot (\varepsilon \mathbf{E})}{q N_a}} + \frac{k_b T}{q} \nabla \cdot \left((I_b + I) \frac{1}{1 + \frac{\nabla \cdot (\varepsilon \mathbf{E})}{q N_a}} \right) = g,
\tag{1.12}
$$

with g constant value to be determined by the boundary conditions, such as the external voltage applied to the material in the direction transverse to beam propagation. For instance, $V = 0$ implies $g = 0$, and the space-charge field reduces to

$$\mathbf{E} = -\frac{k_b T}{q} \frac{\nabla I}{I_b + I},\tag{1.13}$$

which is the diffusive electric field used in Chapter 7 and Chapter 8. In the general case where $g \neq 0$ Eq. (1.12) has a non-trivial structure. We start its perturbative treatment for one-dimensional waves (1+1D). We normalize the physical quantities to the dimensionless variables

$$\mathbf{Y} \equiv \frac{\mathbf{E}}{E_0}, \qquad Q \equiv \frac{I_b + I}{I_b}, \qquad \xi \equiv \frac{x}{x_q} = x\frac{qN_a}{\varepsilon E_0},$$

where E_0 is the intensity-independent local electric field and x_q is the saturation length. Since the illuminated region $l \ll L$, L being the transverse dimension of the medium, the field E_0 can be approximated as $E_0 \simeq V/L$. Through these variables Eq. (1.12) reads [86]

$$\frac{\mathbf{Y}Q}{1 + \mathbf{Y}'} + a\left[\frac{Q'}{1 + \mathbf{Y}'} - \frac{Q}{\left(1 + \mathbf{Y}'\right)^2}\mathbf{Y}''\right] = G,\tag{1.14}$$

with $a = N_a k_b T/\varepsilon E_0^2$ e $G = g/E_0 I_b$, the symbol $'$ indicating $(\frac{d}{d\xi})$. Eq. (1.14) can be formally rendered explicit

$$\mathbf{Y} = \frac{G}{Q} - a\frac{Q'}{Q} + \frac{G\mathbf{Y}'}{Q} + a\frac{\mathbf{Y}''}{1 + \mathbf{Y}'}.\tag{1.15}$$

The first term represent the local contribution, whereas the spatial derivative makes non-local the others. We note that a nonlinearity similar to that occurring in Kerr media (Kerr-saturated) emerges when non-local terms are weak. In conditions where $l \gg x_q$ nonlocal effects play a minor role and we can follow a perturbative approach [80]. Since the spatial derivatives scale as x_q/l and a is of the order of unity, $\eta = x_q/l$ represents a smallness parameter so that

$$\mathbf{Y}^{(0)} = \frac{G}{Q} + o(\eta).\tag{1.16}$$

A first correction is found iterating this solution in (1.15) and reads

$$\mathbf{Y}^{(1)} = \frac{G}{Q} - a\frac{Q'}{Q} - \frac{Q'}{Q}\left(\frac{G}{Q}\right)^2 + o(\eta^2).\tag{1.17}$$

The first term, which is the dominant in biased conditions, gives the so-called Kerr-saturated or screening nonlinearity at the basis of photorefractive solitons. It implies a decrease of the effective field $\mathbf{E}$ respect to E_0 ($G \simeq -1$) as a result of charge rearrangements. The second term can be identified with the diffusive field, whereas the third emerge from its coupling with the saturation (screening) field. Both gives an antisymmetric contribution to the space-charge field; for symmetric

pulses $I(x) = I(-x)$ this fact leads to counterintuitive effects such as ballistic light propagation [87].

The field **E** we have derived leads to a modulation of the index of refraction through the electro-optic effect. However, in order to have significant variations Δn, a large electro-optic response of the material is required. It can be obtained in non-centrosymmetric phases, such as in poled ferroelectrics, and in centrosymmetric paraelectric phases in proximity of the ferroelectric phase transition. In general, the optical properties of an anisotropic media are described through the coefficients $\left(\frac{1}{n^2}\right)_{ij}$ of the indexes ellipsoid [41]. The presence of an external quasi-static electric field **E** modify these indexes respect to their value in zero field. The variation $\Delta\left(\frac{1}{n^2}\right)_{ij}$ of the dielectric tensor is approximately local and can be expressed through the power series expansion

$$\Delta\left(\frac{1}{n^2}\right)_{ij} = \sum_k r_{ijk}E_k + \sum_{kl} s_{ijkl}E_k E_l + \cdots, \tag{1.18}$$

with r_{ijk} and s_{ijkl}, respectively, the linear and quadratic electro-optic tensor. In this section we focus our attention on the case of centrosymmetric media, where the linear response vanishes due to the system symmetry. The quadratic electro-optic effect can be observed only in crystals having a dielectric constant ε that strongly depends on the actual temperature. For this reason, instead of Eq. (1.18), it is more appropriate considering an expansion as a function the linear polarization $\mathbf{P} = \varepsilon_0(\varepsilon_r - 1)\mathbf{E}$. We have

$$\Delta\left(\frac{1}{n^2}\right)_{ij} = \sum_{kl} g_{ijkl}P_k P_l, \tag{1.19}$$

where g_{ijkl} are the elements of the electro-optical tensor that is now expressed through the **P** components. Contrarily to s_{ijkl}, these coefficients are independent from T. The response assumes a scalar form when the optical axes are chosen as reference system, so that g_{ijkl} is diagonal and the index of refraction variation $\Delta n(E)$ becomes

$$\Delta n(E) = -\frac{1}{2}n^3 g_{eff}\varepsilon_0^2 \left(\varepsilon_r - 1\right)^2 E^2. \tag{1.20}$$

Using this expression in Eq. (1.16) we obtain the Kerr-saturated nonlinearity

$$\Delta n(I) = -\Delta n_0 \frac{1}{\left(1 + I/I_b\right)^2} \tag{1.21}$$

with $\Delta n_0 = (1/2)n^3 g_{eff}\varepsilon_0^2 \left(\varepsilon_r - 1\right)^2 E_0^2$. This nonlinearity, depending on the sign of g_{eff}, has a focusing or defocusing effect on the propagating beam for $\Delta n_0 > 0$ and $\Delta n_0 < 0$, respectively. The fact that the intensity appears only through the ratio I/I_b relies in the cumulative response and is the basis for the low powers needed for nonlinear optics in photorefractive media.

1.2.3 Nonlinear wave equation

To understand nonlinear waves dynamics and soliton formation, we show how an index change induced by photorefraction as Eq. (1.21) modifies beam propagation.

We consider a monochromatic electromagnetic wave with frequency $\omega = \frac{2\pi c}{\lambda}$

$$\mathbf{E}_{opt}(\mathbf{r}, t) = \mathbf{E}_\omega(\mathbf{r}, t)e^{i\omega t} + c.c.. \tag{1.22}$$

From Maxwell equations its propagation in a media homogeneous on scales of order λ follows the linear differential scalar equation (Helmholtz equation) [41]

$$\nabla^2 \mathbf{E}_\omega + k_0^2 n^2 \mathbf{E}_\omega = 0 \tag{1.23}$$

where $k_0 = \omega/c$ and n is the refraction tensor, which depends on the spatial coordinates via the electro-optic effect ($n = n(\mathbf{r}, \omega)$). Assuming that it can be expressed as a small perturbation to the linear index of refraction, $n(\mathbf{r}, \omega) = n_0(\omega) + \Delta n(\mathbf{r}, \omega)$, con $\Delta n(\mathbf{r}, \omega) \ll n_0(\omega)$, we have: $n^2(\mathbf{r}) \simeq n_0^2 + 2n_0 \Delta n(\mathbf{r})$, where the ω-dispersion has been omitted. For propagation along the **z**-direction, the field reads

$$\mathbf{E}_\omega(\mathbf{r}) = \sum_{i=x,y} A_{(w),i}(x, y, z)e^{-ik_i z} \tag{1.24}$$

with $k_i = k_0 n_i$, n_i now indicating the generic diagonal term of n in zero external field. Under the slow-varying amplitude approximation, that implies $\partial_{zz} A_{(w),i}(x, y, z) \approx 0$, from Eq. (1.23) we thus obtain the paraxial wave equation

$$\sum_i \left[\frac{\partial}{\partial z} + \frac{i}{2k_i}\nabla_\perp^2 \right] A_{(w),i}(x, y, z) = -\sum_j \frac{ik_i}{n_i}\Delta n_{ij} A_{(w),j}(x, y, z). \tag{1.25}$$

The underlying assumption means that $A_{(w),i}(x, y, z)$ varies on scales much larger than λ, that is the beam is spatially localized in the transverse plane on scales $l \gg \lambda$ (paraxial regime). In an actually homogeneous media, the n_i values are degenerate and, for the one-dimensional case, we have

$$\left[\frac{\partial}{\partial z} + \frac{i}{2k}\frac{\partial^2}{\partial x^2} \right] A_w(x, z) = -\frac{ik}{n}\Delta n A_w(x, z). \tag{1.26}$$

This equation is known as generalized nonlinear Schrödinger equation (generalized NLSE) when $\Delta n = \Delta n(I = |A_\omega|^2)$ and describes paraxial nonlinear wave propagation in the spatial domain. An analogous equation also holds for temporal propagation [9]. The term $\left(\frac{i}{2k}\frac{\partial^2}{\partial x^2} \right)$ represent light diffraction and can be exactly balanced for specific values of the nonlinearity depending on the external parameters. This compensation leads to an amplitude solution A_ω spatially-localized and stationary: a spatial soliton. In particular, with a nonlinearity given by Eq. (1.21) we obtain photorefractive screening solitons. Since numerical simulations has been used to support different experimental results obtained in this thesis, we conclude this section briefly describing how beam propagation according to Eq. (1.26) can be numerically resolved using the split-step Fourier method [107, 281, 78]. Specifically, introducing the diffraction $\hat{D}$ and nonlinear $\hat{N}$ operators, Eq. (1.26) reads $\frac{\partial}{\partial z}A = (\hat{D} + \hat{N})A$. As we are dealing with slow amplitude dynamics along the propagation, there exist an interval h short enough to make separable the action of these two operators. This means $A(x, z + h) \approx e^{h\hat{D}}e^{h\hat{N}}A(x, z)$, with an $O(h^2)$ error related to $[\hat{D}, \hat{N}] \neq 0$ according with the Trotter expansion [281]. Moreover, the error reduces to $O(h^3)$

considering an intermediate step so that $A(x, z+h) \approx e^{\frac{h}{2}\hat{D}} e^{h\hat{N}_{h/2}} e^{\frac{h}{2}\hat{D}} A(x, z)$. Due to the linearity of the diffraction operator, the diffractive steps can be computed passing in the Fourier space; in the more general two-dimensional case with $h/2 = \Delta z$ we have

$$A(x, y, z + \Delta z) = \iint \tilde{A}(k_x, k_y, z) e^{\frac{i}{2k}(k_x^2 + k_y^2)\Delta z} e^{i(k_x x + k_y y)} dk_x dk_y. \tag{1.27}$$

Differently, nonlinearity is an algebraic operator and can applied in the direct space according to $A(x, y, z + \Delta z) = A(x, y, z) e^{-\frac{ik}{n}\Delta n \Delta z}$. Iterating this tecnique over a carefully selected number of steps results in numerical integration of the generalized nonlinear Schrodinger equation.

1.3   Photorefractive solitons

As anticipated, photorefractive solitons are localized waves supported by the Kerr-saturated nonlinearity in which beam self-focusing is mediated by the bias field. Two conditions can be identified: localization can be stationary (steady-state) [248] or transient (quasi-steady-state) [97]. Although temporal stability may be dependent on the experimental configuration [247], we show hereafter that also non-stationary spatial solitons are characterized by specific existence conditions, since their properties will result strictly related to rogue waves formation in photorefractives. Differently, steady-state photorefractive solitons in the one-dimensional centrosymmetric case can be identified as non-evolving solution of Eq. (1.26) with Eq. (1.21). Soliton amplitude depends on the propagation coordinate z only through a phase factor so that, using a self-consistent method, we look for solutions of the form

$$A(x, z) = u(x) e^{i\Gamma z} \sqrt{I_b}, \tag{1.28}$$

where Γ is the propagation constant. We renormalize the spatial coordinate x according to the following definitions

$$\xi \equiv \frac{x}{d} \qquad d \equiv (\pm 2kb)^{-1/2} \qquad b = \frac{k}{n}\left[\frac{1}{2}n^3 g_{eff}\varepsilon_0^2(\varepsilon_r - 1)^2\left(\frac{V}{L}\right)^2\right]$$

The quantity d is the so-called nonlinear length ant its sign reflect the focusing ($g_{eff} > 0$) or defocusing ($g_{eff} < 0$) character of the nonlinearity. From the paraxial equation we obtain the dimensionless nonlinear wave equation [246]

$$\frac{d^2 u(\xi)}{d\xi^2} = \pm\left[\frac{1}{1 + u_0^2} - \frac{1}{(1 + u(\xi)^2)^2}\right] u(\xi), \tag{1.29}$$

with the dimensionless intensity $u_0^2 = I/I_b$ ad the $\pm$ sign corresponding to that of $\Delta n(I)$ [59, 291]. We consider here the focusing case, which gives bright optical solitons. Since Eq. (1.29) is nonintegrable, its solutions identifying specific soliton waveforms are found via numerical integration. These solutions represent an attractor for the optical dynamics and the input beam profile reshapes itself to excite them. In experiments, the accessible parameters are the nonlinear length b, the beam full-width-at-half-maximum (FWHM) Δx and the intensity u_0^2. Therefore the fundamental role
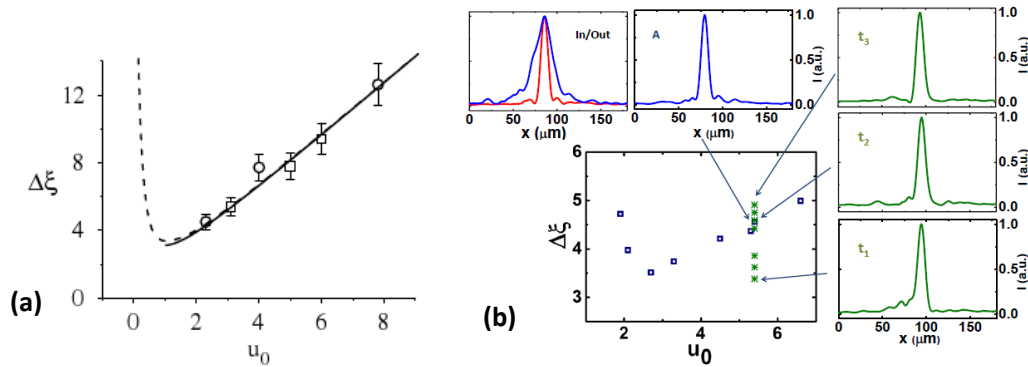
Figure 1.2. Photorefractive soliton existence curve. (a) Numerical prediction (dashed line), experimental results and analytical asymptotic result of segmented wave harmonic theory (black line). (From [82]). (b) Observed soliton waveforms in the steady-state case (blue points) and in non-stationary conditions (green points). (From [208]).

of Eq. (1.29) is to relate at each value of the nonlinearity the corresponding values of u_0 and $\Delta\xi$. The parameter space $(u_0, \Delta\xi)$ is the nonlinear wave phase-space and that points leading to z-independent solutions define the soliton existence curve. The attractive nature of the existence points can thus be rephrased affirming that the soliton will have approximately the same u_0 and $\Delta\xi$ of the gaussian input beam. In Fig. 1.2(a) is reported the theoretical existence curve with experimental data in photorefractive potassium-lithium-tantalate-niobate (KLTN) crystals [79]. For $(u_0 > 1)$ the behavior can be approximated as $\Delta\xi = (\pi/2)(1 + u_0^2)/u_0$, whereas in highly-saturated regimes $(u_0 \gg 1)$ segmented wave harmonic theory gives the asymptotic linear trait $\Delta\xi = (\pi/2)u_0$ [82]. In Fig. 1.2(b) soliton waveforms observed in a paraelectric sample of potassium-sodium-tantalate-niobate (KNTN) are shown in comparison with non-stationary self-trapped waves violating stationary existence conditions [208]. This picture can be partially extended to the (2+1)D (two-dimensional) case, where it becomes a three-dimensional nonlinear problem and assumes anisotropy and spatial nonlocality. In this case, nonlocal contribution in the space-charge field are crucial to soliton existence, since the circular symmetry is broken by the tensorial nature of electro-optic response via the direction of the applied external field. The added spatial dimension implies a field **E** with components in both transverse dimensions according with Eq. (1.11), although the electro-optic index modulation maintains its scalar form. Following the discussion in section 1.2.2, we have the nonlinear system

$$\begin{cases} \nabla \cdot (\mathbf{Y}Q) = 0 \\ \nabla \times \mathbf{Y} = 0 \end{cases} \tag{1.30}$$

Its numerical solution gives the nonlinearity spatial distribution reported in Fig. 1.3. When only the local contribution is taken into account anisotropic self-focusing occurs and symmetric light needles cannot form. Including nonlocal contribution of η-order gives symmetric index patterns supporting two-dimensional spatial solitons. However, a rigorous formulation of the existence curve is not possible in this case, although the phenomenology remains analogous in the $(u_0, \Delta\xi)$ space [216].
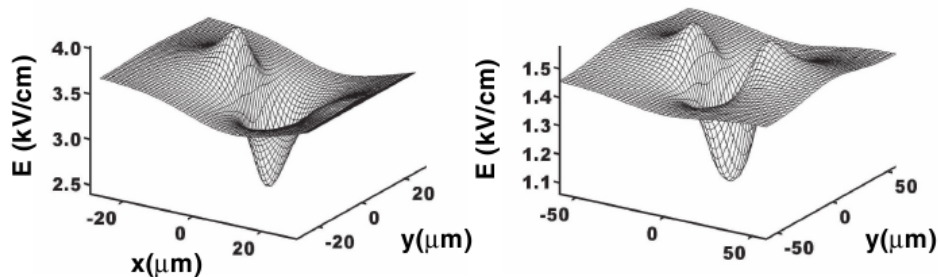
Figure 1.3. Two-dimensional space-charge field. Numerical solution for the local (left) and nonlocal case (right), in which a symmetric pattern allows soliton propagation. (From [83]).

1.3.1 Nonlocal effects and non-stationary dynamics

We extend the treatment to generic non-equilibrium conditions, that is the case in which the beam acquires a temporal dynamics and solitons are transient [111, 312]. Phenomenologically, the initially diffracting light beam undergoes a cycle during which it first progressively self-focuses and settles into a self-trapped wave; then it undergoes a decelerated evolution during which the actual transverse beam intensity changes slightly, but the balancing of self-focusing and diffraction is approximately maintained; finally, it decays into a distorted and once again diffracting beam, ending the cycle. To reveal the peculiar properties of the soliton state we have to reconsider the general case of Eq. (1.11). Introducing the so-called dielectric relaxation time $\tau_d = \varepsilon\gamma/(q\mu s\alpha I_b)$ so that the temporal variable is $\tau = t/\tau_d$, we can write the temporal-dependent counterpart of Eq. (1.16) as

$$\frac{\partial Y^{(0)}(\xi,\tau)}{\partial\tau} + Q(\xi,\tau)Y^{(0)}(\xi,\tau) = G. \tag{1.31}$$

Therefore, the dynamic space-charge field satisfies the integral equation

$$Y^{(0)} = Ge^{-\int_0^\tau Qd\tau'}\left[1 + \int_0^\tau d\tau' e^{\int_0^{\tau'} Qd\tau''}\right]. \tag{1.32}$$

Although the model relies on a specific scale τ_d related to charge mobility, the dynamics described by Eq. (1.31) manifest several time scales. In particular, a stretched exponential behavior characterizes the process leading to non-stationary solitons [76]. Time integration in Eq. (1.32) implies that Y at τ depends on Q at $\tau' < \tau$; the propagation have temporal nonlocality and allows memory effects. In proximity of the localization condition the normalized beam intensity Q becomes approximately time independent and, being $Q \gg 1$, Eq. (1.32) becomes

$$Y \simeq e^{-Q\tau} + \frac{1}{Q} - \frac{1}{Q}e^{-Q\tau} \longrightarrow Y \simeq e^{-Q\tau}. \tag{1.33}$$

The index variation associated to this space-charge field for a quadratic electro-optic response is the exponential nonlinearity $\Delta n = -\Delta n_0 e^{-2Q\tau}$. Generalizing the self-consistent approach of Eq. (1.28) with the spatiotemporal dimensionless variable
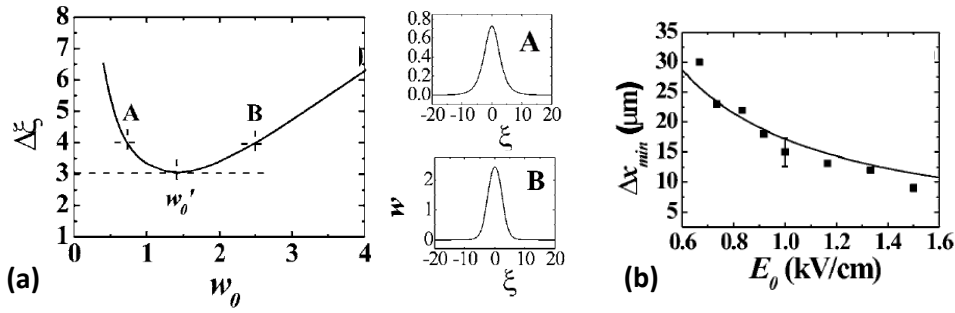
Figure 1.4. Properties of non-stationary photorefractive solitons. (a) Existence conditions with insets showing waveforms in specific points of the curve. Localization occurs at w_0'. (b) Predicted and measured dependence of the minimum soliton transverse size on the external electric field. (From [84]).

$w(\xi) = \sqrt{2\tau}u(\xi)$, the nonlinear soliton profile equation reads [84]

$$\frac{d^2 w(\xi)}{d\xi^2} = -\left[\frac{\left(1 - e^{-w_0^2}\right)}{w_0^2} - e^{-w^2}\right] w(\xi) \tag{1.34}$$

where $w_0 = w(\xi = 0) = \sqrt{2\tau}u_0$. The resulting generalized existence conditions are reported in the $(w_0, \Delta\xi)$ space in Fig. 1.4(a). Relevance of this curve is limited to the conditions for which waveforms are approximately independent of time, which means that the parameters of interest must be those for which the beam shape changes little as w_0 increases. This occurs in proximity of the minimum at w_0' corresponding to the onset of strong saturation in the nonlinearity, which also indicates a maximum value of nonlinear self-action. The minimum conditions in Eq. (1.34) gives a soliton width [84]

$$\Delta x_{min} = \frac{\Delta\xi_{min}\lambda}{2\pi n^2 \varepsilon \sqrt{g_{eff}}} E_0^- 1 \tag{1.35}$$

with $\Delta\xi_{min} \simeq 3.07$. The dependence on the bias field is reported in Fig. 1.4(b). This scale has the peculiar properties of being independent of the wave amplitude, a feature does not occurring in standard stationary solitons. These properties is the key to understand rogue waves statistics and its control, as described in Chapter 6. Another interesting case can also be derived from Eq.(1.32): an optical beam with random phase and amplitude variations on a fast spatial or temporal scale (coherence scale). Considering $Q = \bar{Q} + \Delta Q$, with fluctuations ΔQ having typical amplitude $\bar{Q}$ around zero, we found [86]

$$Y^{(0)} = Ge^{-\bar{Q}\tau} + \frac{G}{\bar{Q}}\left(1 - e^{-\bar{Q}\tau}\right), \tag{1.36}$$

that, for $\tau \gg 1/\bar{Q}$, reduces to the time-independent case $Y^{(0)} = G/\bar{Q}$. Therefore, the nonlinear response averages out fast intensity fluctuations leading to the steady state condition as for a coherent beam. This is the basis for incoherent spatial solitons and it can be further generalized to temporally incoherent (white) light [188, 63].

1.3.2   Continuous solitons in a lattice nonlinearity

In this section we describe a novel study we have addressed in the context of photorefractive solitons in discrete media [217]. Generally, the coupling between different and matched spectral components of the optical field is one of the fundamental effects governing propagation through periodic systems. The interplay between this coherent effect and nonlinearity has been extensively investigated allowing diffraction control [100, 108] and giving rise to self-localized states, such as discrete and gap solitons [146, 109, 181]. Experiments on discrete trapping are generally based on photonic lattices made from etched waveguide arrays [99, 180] or created through optical induction in photorefractive media [98, 172]. Studies have spanned a wide variety of physical mechanisms affecting these kind of solitons, such as nonconventionally biasing [309]. However, in all cases the soliton has always evolved in a fixed linear/nonlinear pattern, i.e., in conditions in which the underlying lattice is not appreciably affected by the wave. We here study theoretically and experimentally an entirely opposite condition: spatial solitons that form in a lattice nonlinearity. A lattice nonlinearity is a periodic variation in the nonlinear response that is in turn negligible in the linear response. This means the lattice itself depends on the soliton, and both lattice and soliton are strongly interacting during propagation. This fundamental difference with respect to previous studies is schematically illustrated in Fig. 1.5, where the optical propagation in a photonic lattice is compared with that in a lattice nonlinearity. The standard physical condition (Fig. 1.5(a)) consist in a media with a periodic index of refraction variation δn_{latt}, affecting parametrically the superimposed soliton nonlinearity δn_{sol}. So, while the nonlinear waves evolve into a lattice-dependent trapped state, δn_{latt} remains almost completely unaffected by the waves dynamics. On the contrary, if the beam and lattice are mutually nonlinear, $\delta n = \delta n(\delta n_{sol}, \delta n_{latt})$, the nonlinear propagation modifies spatially the
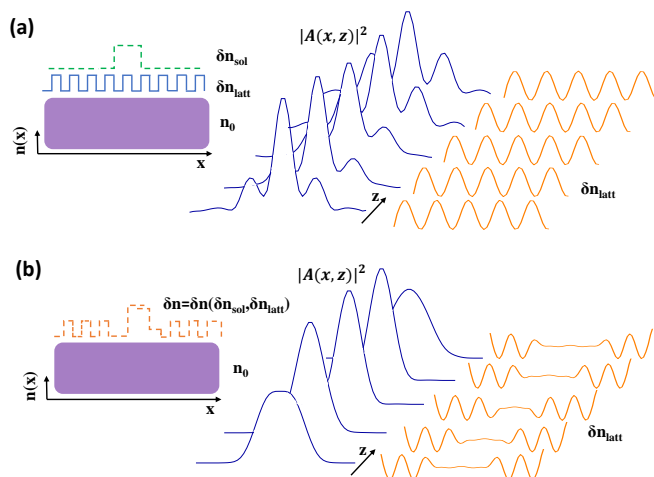

Figure 1.5. Nonlinear propagation in periodic systems. (a) Trapping in photonic lattices: the periodic pattern δn_{latt} affects the spatial propagation but is not affected by the wave. (b) Trapping in lattice nonlinearity: optical field and lattice are mutually coupled and δn_{latt} depends on the waveform. (From [217]).
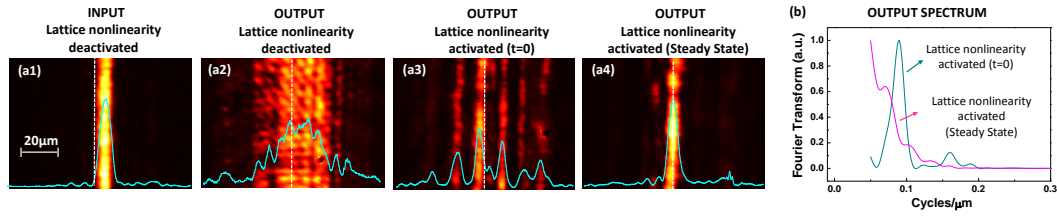
Figure 1.6. Light propagation in the lattice nonlinearity embedded in a microstructured KLTN. (a) Observed beam dynamics from the starting delocalized discrete pattern to the continuous soliton: (a1) input and (a2) output beam when the lattice nonlinearity is deactivated, (a3) output discrete spatial distribution as soon as the lattice nonlinearity is enabled and (a4) continuous soliton at the steady state. (b) Intensity Fourier transform of (a3) (cyan line) and (a4) (magenta line). (From [217]).

underlying periodic pattern itself (Fig. 1.5(b)).

We investigate the issue using spatial photorefractive solitons in a volume microstructured KLTN crystal with a built-in oscillating low-frequency dielectric constant. This systems is also the basis for discoveries presented in Chapter 3, where details on the crystal structure and properties are also reported. Here we consider how the pattern causes an oscillating electro-optic response that induces a periodic optical nonlinearity. In fact, the resulting on-axis propagation dynamically shows a transition from a discrete pattern to a soliton with the peculiar property of being continuous in the transverse dimension, irrespective of the beam size compared to the grating period. The effective continuous Kerr-saturated solitons form out of the combined compensation of diffraction and of the underlying periodic volume pattern. In particular, the lattice nonlinearity arising from the optically induced space-charge field reads

$$\Delta n(x) = \delta n \cos(Kx) - \frac{1}{2} n^3 g_{eff} \varepsilon_0^2 \varepsilon_r^2 \left[1 + \frac{2\delta T_C}{T - T_C} \cos(Kx) \right] \left(\frac{E_0}{1 + u(x)^2} \right)^2 , \quad (1.37)$$

where δn contains the linear contribution of the Sellmeier's refractive index grating, $K = 2\pi/\Lambda$ the grating number, being Λ the grating period, with the lattice amplitude δT_C that can be controlled through the critical temperature T_C. It should be noted that the first linear term only weakly affects propagation; differently, the field-dependent lattice term is not at all a perturbation to the screening nonlinearity. Beam propagation experiments are carried out with μW paraxial one-dimensional waves at $\lambda = 532$ nm in a transmission configuration with respect to the grating, with the main wavevector $\mathbf{k} = \mathbf{k}_z$ orthogonal to the grating vector $\mathbf{K}$ (grating period $\Lambda = 5.5 \pm 0.3 \mu m$) and to the bias field. Numerical results are obtained using the beam propagation method (BPM) to resolve Eq. (1.26) with the nonlinearity given by Eq. (1.37) and parameters that match those from our experiments.

The observed beam propagation dynamics is shown in Fig. 1.6(a). When the electro-optical response is not activated through the bias field, the input Gaussian beam with full width at half maximum FWHM$= 7\mu m$ experiences quasi-linear diffraction, resulting in an FWHM$= 26\mu m$ output distribution (Fig. 1.6(a1-a2)). In these conditions, only the liner part of the lattice is involved in the beam propagation and, from the spectrum (Fig. 1.6(b)), it seems to be negligible. However, when the
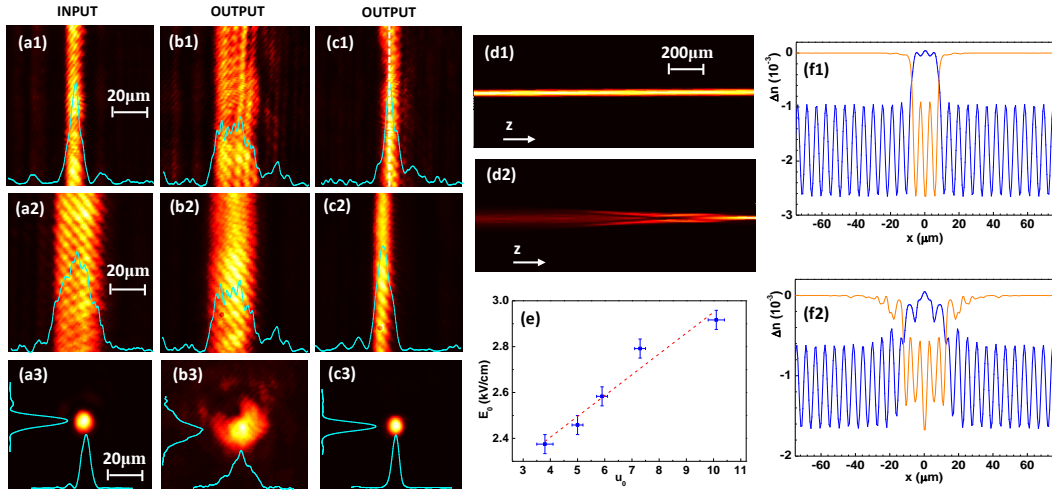
Figure 1.7. Soliton propagation: experimental and numerical results. Observed (a) input, (b) diffracted and (c) self-trapped output at applied bias field for (top) 1D beams and (bottom) 2D beams. In all the cases continuous localization emerge as confirmed numerically by (d) propagation and (f) associated spatial index of refraction modulation (blu line) compared with just the contribution of the photorefractive response in biased condition (orange line). (e) Experimental relation between normalized intensity and external field for 1D solitons with linear fit (dashed line).(From [217]).

beam is exposed to the lattice nonlinearity, that is, the sample is biased, it instantaneously (at fast electro-optic response times) rearranges itself over the periodic index of refraction pattern. Considering the μW power used in the experiments, the photorefractive response begins changing the pattern only approximately $10-20s$ after this initial stage. The discrete light distribution emerging in the first instants, before the light is able to produce the space-charge field, is shown in Fig. 1.6(a3), for $u_0 = \sqrt{I_{peak}/I_b} \simeq 8$ and $V = 400$V, and appears delocalized compared to the input beam distribution. The operational temperature in this case is $T = T_C + 2K$, so that, from Eq. (1.37), we expect a nonlinear lattice with the same amplitude of the "homogeneous" photorefractive nonlinearity (Δn of the order of 10^{-3}). The build-up of the space-charge field causes the progressive local screening of the periodic lattice until the continuous steady-state soliton forms after few minutes (Fig. 1.6(a4)). The soliton transverse profiles have no trace of a periodic feature, so the lattice nonlinearity allows the transition from a discrete delocalized pattern to a continuous soliton. In Fourier space (transverse spatial spectrum), the spectrum of the output intensity distribution passes from having a dominant peak compatible with $K = 2\pi/\Lambda$ to a monotonous decay without dominant resonances (Fig. 1.6(b)). This continuous soliton behavior is demonstrated in Fig. 1.7. When no bias field is applied the input beam with FWHM$= 7\mu m$ experiences homogeneous diffraction resulting in an FWHM$= 24\mu m$ output distribution (Fig. 1.7(a1-b1)). Applying a V$= 580V$ static potential a steady-state soliton propagation is obtained for an intensity ratio $u_0 \simeq 5$ (Fig. 1.7(c1)). This absence of discrete features is confirmed by numerical simulation revealing a soliton shape typical of continuous solitons, as
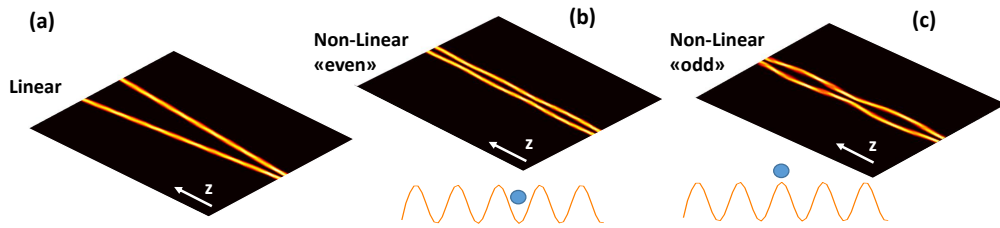
**Figure 1.8.** Soliton interaction in a lattice nonlinearity. Numerical results showing (a) repulsion in the linear regime, (b-c) bound state in a lattice nonlinearity for input beams in (b) even and (c) odd configuration respect to the underlying lattice, which is sketched in the insets with the beam center indicated by the blue dot.

reported in Fig. 1.7(d1). Interestingly, this finding does not match what is expected for photorefractive solitons in a fixed bulk grating, where waveforms satisfying a two-parameter existence condition are characterized by modulated components [67]. This underline the role of the lattice nonlinearity. The continuous property has roots in the coupling between periodic and non-periodic terms in the soliton supporting nonlinearity. Indeed, simulations demonstrate an index of refraction variation losing the sinusoidal shape in the soliton region (Fig. 1.7(f1)); the screening field locally leads the underlying lattice into a latent state. This effect is independent both of the grating amplitude and of the beam width. The first statement is verified spanning the experimental soliton parameters (u_0, E_0) (Fig. 1.7(e)) and changing the operational temperature; in particular, we note that even when the lattice amplitude is larger than the standard photorefractive term the continuous picture remains unchanged. Although experimentally we cannot access into this regime, simulations confirm this behavior, stressing the local interaction between wave intensity and nonlinear lattice. Independence from the beam waist is demonstrated launching beams whose size covers several grating periods (weak-binding). As reported in the middle row of Fig. 1.7, a FWHM$= 22\mu m$, $u_0 = 2.5$ input beam weakly diffracts when unbiased; it self-focuses up to $8\mu m$ in the nonlinear case. Even in this case the output lacks marked discrete features, as numerically verified. We also demonstrate that what has been achieved occurs in the same spatial lattice geometry for two-dimensional solitons; a 2D continuous soliton, $8\mu m$ sized, is shown in Fig. 1.7(c3) at $u_0 = 8.5$. Fig. 1.7(e) reports the relation between normalized intensity and external field for observed 1D solitons (existence conditions); the linear behavior is coherent with the general relationship at high saturation (section 1.3), even though the slope observed is considerably reduced, this underlining the fundamentally different nature of our present continuous solitons compared to conventional photorefractive nonlinear waves. The continuous picture is expected to change if the electro-optical lattice can be decoupled from the photorefractive nonlinear response. Since these two responses act on different time scales, being the electro-optic modulation instantaneous with respect to the photorefractive one, the grating can be decoupled dynamically. This is exactly the decoupling occurring in the first stages of propagation into the lattice nonlinearity and leading to a discrete pattern, as discussed and reported Fig. 1.6(a).

An interesting consequence of the lattice nonlinearity action relies in how it

affects soliton interaction. Unfortunately, our specific sample is not suitable for this experimental investigation due to the small fabricated lattice period Λ, that for solitons in adjacent lattice sites implies an ultra-tight regime where existence of photorefractive solitons is at risk [85]. However, from numerical simulations we predict an interesting phenomenon: we found the interaction properties typical of a discrete system [197, 103] but with continuous solitons. Numerically, we have considered the same nonlinear parameters describing our setup, except for the lattice period, that is $\Lambda = 10m$, and we set $\delta n = 0$, $dT_c = 1K$ and $T = T_c + 2K$. Results are reported in Fig. 1.8 and show the interaction dynamics of two adjacent π-out of phase spatial solitons. In the linear case, that is without the lattice nonlinearity, as expected there is repulsion between the π-out of phase solitons. On the other hand, a bound state exist in the presence of the nonlinear lattice, both when the beam is initially centered in a minimum of the lattice (we call this configuration "even" in Fig. 1.8(b)) or in a maximum of the lattice ("odd", Fig. 1.8(c)). In both these cases the discrete bound states have a continuous feature, a paradigmatic property ever found in other systems.

PART I

Electro-optics of disordered ferroelectrics

Chapter 2

Anomalous electro-optic effect

The electro-optical response of critical disordered ferroelectric crystals are investigated in this Chapter. The peculiar properties we have found not only form the basis for accessing unconventional regimes of nonlinear wave propagation but represent an insight in the rich and debated physics of these complex materials. We demonstrate electro-optics as an experimental method to probe dipolar dynamics in proximity of the ferroelectric phase transition. In particular, we report observations of the giant electro-optic effect in a potassium-sodium-tantale-niobate (KNTN) crystal and we unveil an anomalous behavior of its symmetry [218]. We relate these effects to a super-polarization of the medium, which is directly connected to an anomalously reduced thermal agitation in the reorientational response of the underlying polar-nanoregions.

2.1 Disordered ferroelectrics: an overview

Compositional disorder in ABO_3 perovskites can profoundly change their ferroelectric response [240]. The presence of different compounds at the atomic level introduces for specific composition concentrations competing structural phases that at the morphotropic phase boundaries [10, 175], such as low-symmetry bridging phases and ferroelectric-antiferroelectric ordering boundaries [40], result into unique polarization properties, examples being anomalously large capacitance and giant piezoelectricity [158, 272]. Moreover, disorder on the nanoscale can lead to dispersion in the dielectric response, thermal, electric-field and strain hysteresis, and anomalous relaxation times, traits that are typical of relaxor ferroelectric behavior [256, 37]. In many respects, the unique properties of the disordered ferroelectric state can be modelled as arising from a network of randomly interacting polar-nanoregions (PNRs) embedded in a highly polarizable medium [276, 122, 299, 300]. Although the microscopic origin of these PNRs and the role played by random fields is still an open question [11, 225, 151, 214, 183], it is established that they can lead to dipolar-glasses with non-ergodic properties when appropriately supercooled [38]. In fact, dipolar dynamics in some relaxor ferroelectric crystals is characterized by the so-called freezing temperature, a temperature at which the dielectric relaxation time diverges and polarization fluctuations result quenched [285, 143, 144]. Percolation of PNRs has been proposed as the physical mechanism underlying the dipolar-
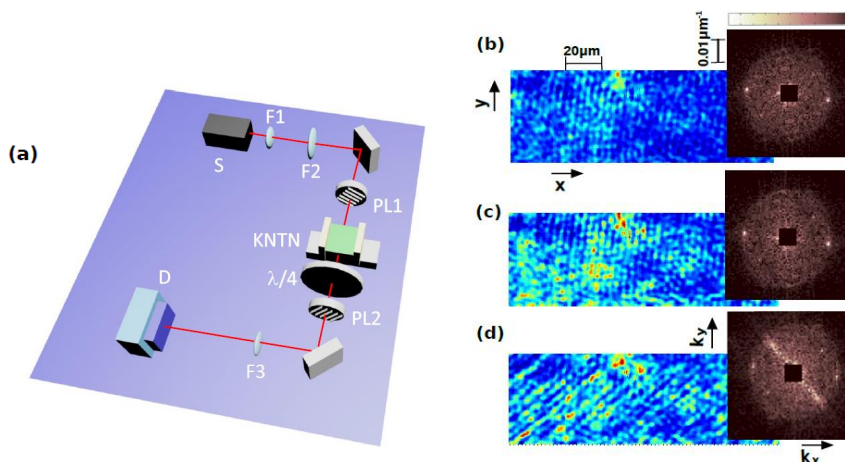
Figure 2.1. Electro-optical experiments in critical KNTN crystals. (a) Experimental
setup (see text). (b) Transmission microscopy images (intensity is in arbitrary units) in
zero-field-cooling at $T = 287K$ and (c) at $T = T_m = 285.5K$; (d) applying a $0.85kV/cm$
dc field the glassy state at T_m turns into ferroelectric domains with geometrically fixed
boundaries at $45°$ with respect to the principal axes of the crystal. Normalized intensity
of the two-dimensional Fourier transform (insets in (b), (c) and (d)) that highlights the
appearance of a diagonal feature in the spectrum associated to ferroelectric domains.
The added spectrum in (d) is continuous, with no fixed periodicity, typical of a globally
disordered state.(From [218]).

glass state [224, 228]. Moreover, in proximity of the Curie temperature, in the
nominally paraelectric (cubic) phase, PNRs greatly affects optical birifringence
[305, 229] and electro-optical response leading to giant electro-optical coefficients
[56, 57] and depolarization effects [128]. We have experimentally found that these
optical properties are manifestations of a more general anomalous electro-optic effect
strictly related to freezing of dipolar fluctuations. Part of our results has been
also confirmed by dynamical (time-resolved) electro-optical studies on analogues
KTN-based crystals [271].

2.2   Electro-optic experiments

In our electro-optic setup the KNTN crystal [237, 269, 137], $K_{0.89}Na_{0.11}Ta_{0.63}Nb_{0.37}O_3$,
is grown through the top-seeded solution method by extracting a zero-cut $1.17^{(x)}$ x
$1.90^{(y)}$ x $2.43^{(z)}$ mm optical quality specimen. In order to identify the relaxor-type
behavior, i.e., the temperature range where permanent dynamic PNRs affect the
response, we perform dielectric spectroscopy using a standard LCR meter setup for
different frequencies and a thermal chamber. Dielectric results are reported in section
2.3 to allow comparison with optical findings. The dielectric peak signaling a dy-
namic phase transition appear at the temperature $T_m = 285.5K$ and measurements
are performed for $T \gtrsim T_m$, where the PNRs allow an optimal optical transmission
but where glassy physics effects are still observed. The cross-polarizer set-up is
schematically illustrated in Fig. 2.1(a). A visible laser beam from a diode-pumped
doubled Nd-Yagg laser (wavelength $\lambda = 532nm$, $5mW$ continuous wave beam before
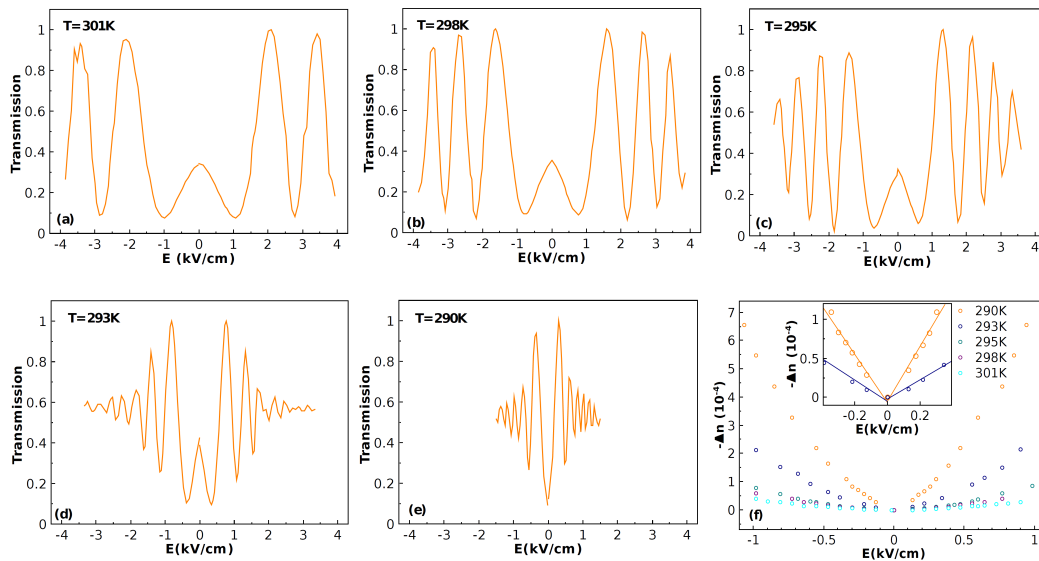
Figure 2.2. Anomalous electro-optic effect. Ligth transmission through crossed polarizers as a function of electric field E for different temperatures: (a) for $T = 301$K, (b) 298K, (c) 295K, (d) 293K, and (e) 290K. In the latter case the natural birefringence of the KNTN sample has been compensated with a $\lambda/4$ waveplate. (f) Summary and comparison of Δn versus E for the different temperatures signaling the spike-like distortion (highlighted in the inset for 290K and 293K, lines are fits with $-\Delta n \propto |E|$) of the expected parabolic dependence as T_m is approached.(From [218]).

the sample) **S** is expanded to an approximate plane-wave of $10mm$ radius by the two confocal lenses **F1** and **F2**. The beam passes through the first polarizer **PL1** that transmits light linearly polarized at 45°with respect to the plane of the experiment, then through the sample, and finally through the second polarizer **PL2** orthogonal to the first. The sample is zero-cut along its principal $m3m$ axes and is oriented parallel to the plane of the experiment with the input facet approximately orthogonal to the propagation direction z. It is biased by a static electric field E delivered through two plane electrodes sputtered onto the x-facets of the sample. The sample is housed in a thermal conductive holder whose temperature is controlled by a Peltier cell. Transmitted light is collected by the exit lens **F3** and the power is detected through power meter **D** or imaged through a CCD camera. We implement a plane-wave intensity of approximately $1.5\mu W/cm^2$, and no photorefractive effects associated with Cu impurities (~ 0.001 atoms per mole) for the duration of our experiments are detected. In Fig. 2.1(b-d) we report the cross-polarizer transmission images cooling the sample from $T^* = 305K$ to T_m at a cooling rate of $\alpha \simeq 0.1$K/s. A homogeneous and disordered weak transmission of light is observed in the whole temperature range for zero-field-cooling. For values of T in proximity of T_m ($T - T_m < 4$K), an external field causes organized ferroelectric structures to form [288, 121]. For example, at $T \simeq T_m$, a field $E \simeq 1$kV/cm causes the formation of large ferroelectric domains with geometrically fixed boundaries at 45° with respect to the principal axes of the crystal (2.1(d)).

We proceed to quantify polarization transmission properties $5 - 15$ K above T_m.

Light is transmitted because the sample changes the relative phase of the x- and y-polarized components of the optical field (respectively parallel and orthogonal to the external field E) through the relative electro-optic modulation of the index of refraction Δn. The output transmitted intensity I and the input intensity I_0 are connected to this field-induced relative phase-shift $\Delta \phi$ through the relationship $I/I_0 = \sin^2(\Delta \phi/2)$, where $\Delta \phi = \Delta n(2\pi/\lambda)L$, and L is the length of the crystal along the propagation direction. Analyzing the dependence of $\Delta \phi$ on E allows us to detect the macroscopic dependence of Δn on E and hence obtain the crystal P versus E response. The intensity transmission data at different temperatures T as a function of applied bias field E are reported in Fig. 2.2. The crystal is cooled to the operating temperature with a cooling rate of $\alpha \simeq 0.1\mathrm{K/s}$, and, in distinction to analogues experiments, during this cooling no external bias field is applied [56, 57]. We note that cooling rate have a profound impact on the response properties of the KNTN crystal [216, 207]. Data are taken for the decreasing field amplitude loop (the field amplitude is decreased during our experiments), and no residual polarization is detected at zero field. As testified by the rapid decrease in fringe period, the electro-optic response is seen to increase anomalously as T_m is approached. Moreover, fringe visibility is found to decrease for high fields and for lower temperatures, the signature that PNRs are dominating response [128, 269]. The sinusoidal fringe pattern is therefore modified by a field-dependent pre-factor M_d that depends on the PNR size via the operating temperature, cooling rate and applied field [128]. In Fig. 2.2(e) we report the fringe pattern measured with the $\lambda/4$ waveplate that compensates the non-zero value of transmission at $E = 0$. We are thus able to measure the natural birefringence to be $\Delta \phi_0 \simeq -0.36$ radians. In Fig. 2.2(f) we summarize the Δn versus E data for the different temperatures. We note that the index of refraction modulation gradually switches from the typical quadratic field dependence distinctive of a paraelectric phase (section 1.2.2) at $T = 301\mathrm{K}$ to a low-field strongly nonlinear (spike-like) dependence at $T = 290\mathrm{K}$, even though no macroscopic changes in the crystal symmetry occurred. However, the linear behavior typical of polar states signals that symmetry breaking are occurring at microscopic scales, a phenomenon recently observed also in liquid crystals [145].

2.3 Anomalous dipolar response

To investigate the physical underpinnings of this anomalous electro-optic behavior we proceed to reconstruct the P versus E relationship from the Δn versus E data, at the different values of T. We consider the relation (1.20) of section 1.2.2 with $n = 2.31$ and $g_{eff} \equiv (g_{11} - g_{12}) = 0.14$ C^{-2}m^4. The polarization curve we obtain represent an optical measurements of the response to bias fields usually obtained through capacitance measuraments [270].

2.3.1 Super-polarization

The optically measured P versus E curves are reported in Fig. 2.3(a), in the range between $T = 301K$ and $T = 290K$. We first note that, as expected for a system that has global inversion symmetry, no residual polarization or standard ferroelectric hysteresis behavior emerges (Fig. 2.3(c)). However, in distinction to a standard
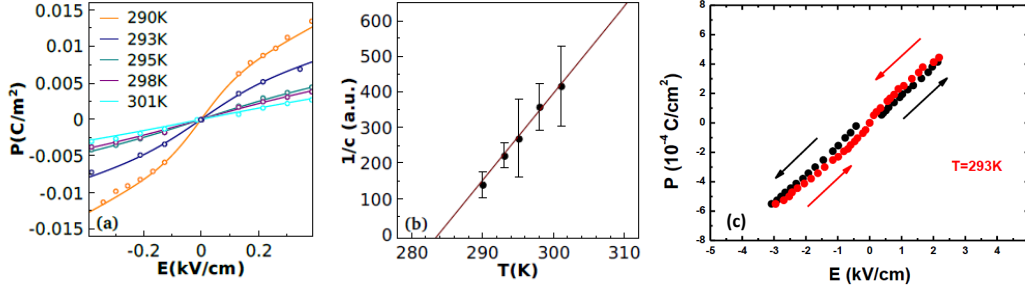
Figure 2.3. Super-polarization in KNTN. (a) The P versus E relationship as a function of T from the measured values of $\Delta n(E)$ ($P = \pm(-2\Delta n/n_0^3(g_{11} - g_{12}))^{1/2}$, the sign depending on the sign of E) indicates a temperature dependent distortion of linearity towards an S-shaped behavior. Full lines represent the fit with the super-polarization model of Eq. (2.1). (b) Linear temperature scaling of the inverse fit parameter c (see text) that gives the shift temperature $T_0 = (283 \pm 2)K$. (c) An example of slim-loop hysteresis and absence of residual polarization in agreement with the paradigm of weakly interacting dipoles as opposed to dipoles undergoing a standard, second-order, phase transition. (From [218]).

system with inversion symmetry, where the polarization should be predominantly linear in the electric field [302], here the polarization manifests a gradually increasing nonlinearity at low bias fields. Indeed, decreasing the temperature towards T_m, the polarization response passes from a linear function of the field to the peculiar S-shaped curve observed in non-optical freezing relaxors [286, 152]. Negligible hysteresis and zero-field residual polarization indicate that dipoles associated to the PNRs spontaneously flip during measurements, so that our starting model is that of Langevin reorientation. Considering the predominant role of PNRs, an ensemble of uniform noninteracting clusters having uniaxial symmetry has an average polarization [286] $\mathbf{p} = \rho p_0 \tanh\left[p_0|E|/kT\right]\mathbf{u}$, where ρ is the density of clusters with dipole moment p_0, kT the thermal energy and $\mathbf{u}$ the field unit vector. This behavior is, however, evidently incompatible with the observed data, since the large variations occur for an apparently negligible relative change in temperature $\Delta T/T \sim 0.03$. In turn, the curves are compatible with a shifted-temperature Langevin reorientation $\mathbf{p}_{PNR} = \rho p_0 \tanh\left[p_0|E|/k_B(T - T_0)\right]\mathbf{u}$, where T_0 is a phenomenological parameter hereafter assuming the meaning of a freezing temperature. The macroscopic polarization P is now composed of a dipolar contribution and a standard linear susceptibility χ_p due to the paraelectric host. Specifically,

$$\mathbf{P} = \mathbf{p}_{PNR} + \mathbf{p}_{\chi_p} = \rho p_0 \tanh\left[\frac{p_0|E|}{k_B(T - T_0)}\right]\mathbf{u} + \varepsilon_0 \chi_p \mathbf{E} \ , \qquad (2.1)$$

where the first term dominates the low-field response and the second prevails at high fields where the PNR response is saturated. The full lines in Fig. 2.3(a) are a fit of measured P to Eq. (2.1) for low values of E. Best fits provide values of the parameter $c = p_0/k_B(T - T_0)$ that, as reported in Fig. 2.3(b), give $T_0 = (283 \pm 2)K$. The resulting electro-optic response in the cross-polarizer configuration is hence

associated with

$$\Delta n = - (1/2)n^3 g_{eff}\varepsilon_0^2(\varepsilon_r - 1)^2 E^2 - n^3 g_{eff}\rho p_0 \tanh\left[\frac{p_0|E|}{k(T - T_0)}\right]\varepsilon_0(\varepsilon_r - 1)|E|$$
$$- (1/2)n^3 g_{eff}\rho^2 p_0^2 \tanh^2\left[\frac{p_0|E|}{k(T - T_0)}\right] \quad .$$

(2.2)

For values of $T - T_0$ such that $p_0|E|/k(T - T_0) \gg 1$, the second term describes the observed anomalous contribution $\Delta n \propto |E|$. This term is indeed dominant over the first, which is the standard quadratic term arising from the paraelectric host, whereas the third term can be neglected in a first approximation. We underline that the freezing response is intrinsically different from the standard linear $\Delta n \propto E$ and quadratic $\Delta n \propto E^2$ effects associated, respectively, to systems that are noncentrosymmetric and centrosymmetric. In a system with global inversion symmetry, spatial inversion causes $E \to -E$ but $\Delta n \to \Delta n$, and the leading response is congruently quadratic in the amplitude of E. In our freezing-PNR-dominated system, which has no globally-defined symmetry [122], spatial inversion causes $E \to -E$, $\Delta n \to \Delta n$, but the leading response is still *linear* in the amplitude of E. It can be referred as a symmetry-preserving electro-optic effect that emerge when different symmetric states are present on different physical scales. This anomalous electro-optic behavior has been confirmed by *H.Tian et al.* [271] probing in time at $kHz - MHz$ frequencies the dynamics of PNRs embedded in a KTN crystal. They report an analogues spike-like distortion of the elcetro-optic response in proximity of the dielectric peak temperature when a low-frequency AC field is used. The behavior observed in Ref. [271] is associated to asymmetric distribution of PNRs along the bias field direction and presents reduced temperatures fluctuations, as we have directly measured. The phenomenological model they propose further confirms our evidence of dipolar freezing ruled by the blocking temperature T_0. It means that the giant polarization response in disordered ferroelectrics in proximity of the phase transition can be understood through the classical picture of zero-temperature dipolar dynamics as illustrated in Fig. 2.4. As freezing is approached, all states but the minimum energy state become unpopulated, a form of classical condensation; an arbitrarily small external field will shift the ground state and with it, in unison, the entire system, without involving microscopic interaction, diffusion, or dissipation. The system manifests a natural tendency of allowing binary encoding: the macroscopic response is simply a combination of the two microscopic states. In general, this is superimposed to a standard susceptibility, and the signature will take the form of a characteristic twist in the overall input-output curve, as the one we observe (Fig. 2.3). Moreover, in the next section we report independent dielectric spectroscopy results showing how dipolar freezing emerge with the same freezing temperature also in dielectric fluctuations. In fact, dipole reorientation involves a well-defined external potential $-\mathbf{p} \cdot \mathbf{E}$, whereas relaxation is of microscopic origin with a built-in phenomenological potential barrier ΔU. To validate the picture we have to compare the freezing T_0 measured from the P versus E curves with the one eventually emerging from dielectric relaxation.
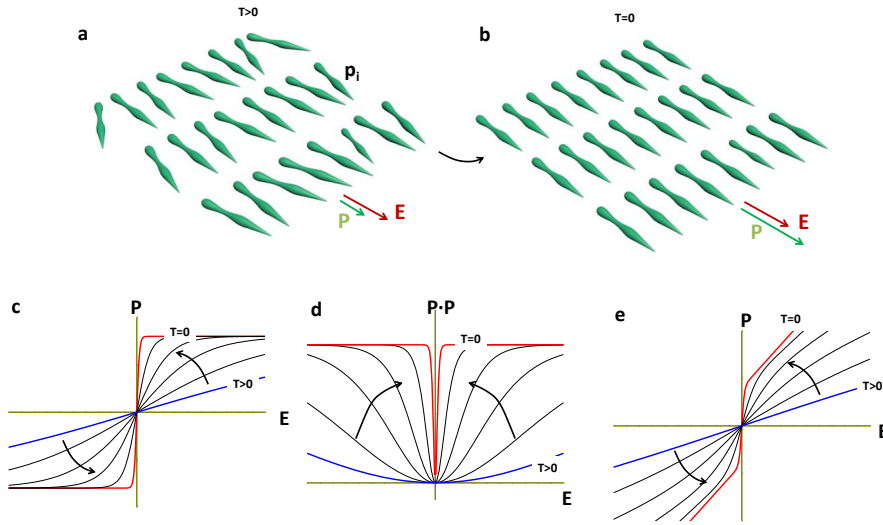
Figure 2.4. Effective ultracold classical dipolar response. (a-b) Representation of thermally agitated dipoles $\mathbf{p}_i$ at a given T compared to the ultra-low-temperature case. For finite T, the macroscopic response $\mathbf{P}$ is caused by the average alignment to the external bias field $\mathbf{E}$, compared to the $T \simeq 0$ case, where all single dipoles align, even when they are non-interacting. (c) Leading macroscopic response $\mathbf{P}$ at finite values of T (blue curve-standard linear response) compared to the leading macroscopic response in proximity of freezing (red curve-binary response). (d) Leading scalar response at a finite T (blue curve-parabolic response) compared to the case of spike-like response (red curves). (e) Signature of near-zero response superimposed to a standard linear response $\propto E$, that is according with Eq (2.1) and results in Fig. 2.3.

2.3.2 Freezing dielectric relaxation

We have discussed how disordered ferroelectrics cooled below a material-dependent temperature T_d (Burns temperature [49]) manifest a response that can best be described as dominated by randomly distributed PNRs. One flag to the onset of PNR-dominated response emerges in the dielectric response: for temperatures $T_m < T^* < T_d$, below the so-called intermediate temperature T^* and above T_m, the temperature for which the relaxor dielectric constant has its maximum, the Curie-Weiss law (mean-field theory) breaks down [287]. The breaking of mean-field behavior implies a local breaking of symmetry (on the nanometer scale), which can eventually expand into a true ferroelectric state with long-range order (micrometer scale) below T_m. Freezing occurs when the Arrenhius law governing dielectric thermal flutuations is violated and superseded by a Vogel-Fulcher-Tammann (VFT) relaxation law $\tau = \tau_0 \exp\left(\Delta U / k_B (T - T_0)\right)$, where T_0 is the so-called dipolar freezing temperature. Mesoscopically it can be associated to PNR percolation, where T_0 is the PNR percolation threshold [224]. To investigate these dielectric properties in our KNTN sample we use dielectric spectroscopy. Measurements are carried out using a precision LCR meter (Agilent 4284A) in a standard configuration. Temperature is controlled using a programmable thermal chamber and monitored through a calibrated silicon diode sensor ($0.01K$ in precision), while the sample in kept in vacuum. Dielectric data versus temperature are in a quasi-static regime, with a cooling/heating rate of
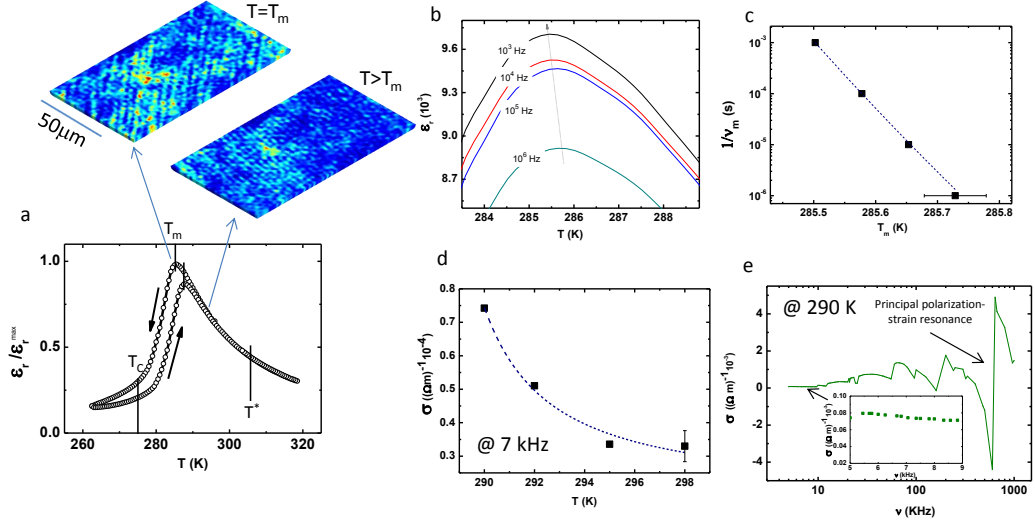
Figure 2.5. Dielectric freezing fluctuations in critical KNTN crystal. (a) Measurements of the real part of the dielectric constant ϵ_r (at 1KHz) normalized to the peak value ϵ_r^{max} versus T, indicating the measured intermediate T^* and Curie T_C temperature. Inset showing polarization microphotographs of the resulting optical transmission in analogy with Fig. 2.1. (b) Dispersion in ϵ_r in proximity of T_m and (c) shift of T_m as a function of ν. (d) Large increase of low-frequency (below resonance) conductivity on decreasing T towards $T_0 = (285 \pm 4)$K (fitting data with a phenomenological $\sigma = \sigma_0 \exp{(\Delta U''/k_B(T - T_0))}$). (e) Measured conductivity σ versus ν for $T = 290$K, revealing an almost flat response at low-frequencies and a series of polarization-strain resonances in agreement with other known disordered systems [211].

$1mK/s$ and single data acquisition time of $5ms$. The quasi-static measurement (for fields oscillating at 1 KHz) of dielectric constant versus temperature $\epsilon_r(T)$ is shown in Fig. 2.5(a). The thermal dielectric hysteresis pinpoints the region of considerable macroscopic non-ergodic behavior where glassy physics is expected. The diffuse peak of the ϵ_r is observed at $T_m = 285$ K (decreasing temperature loop) and $T_m = 288$ K (increasing temperature loop). The Curie temperature $T_C = 275$ K is evaluated fitting $\epsilon_r(T)$ with the Curie-Weiss law $\epsilon_r = C/(T - T_C)$ (for $T > T_m$). Anomalous dielectric behavior, typical of relaxors, is reported in Fig. 2.5(b-e). The sample is cooled below $T^* \simeq 305$K, temperature below which we detect a deviation from the mean-field Curie-Weiss law. In Fig. 2.5(b) we compare the measured values of ϵ_r for different electrical frequencies ν. The dotted line joins the corresponding values of T_m plotted in Fig. 2.5(c). Dispersion typical of relaxor response is such that the scaling of T_m versus $1/\nu$ follows a VFT relaxation law $(1/\nu) \equiv \tau = \tau_0' \exp{(\Delta U'/k_B(T - T_0))}$ with $T_0 = (282 \pm 3)$K. A giant increase in conductivity σ is also found as a function of T (Fig. 2.5(d)). However, in the diverging behavior of σ we cannot discriminate the contribution due to T_0 approaching respect to that given by the Curie peak at T_C. We also observe a flat spectral response below the polarization-strain-resonance, as shown in Fig.2.5(e) for $T = 290$K. To evaluate T_0 from relaxation data, we note that although the shift in T_m versus ν already indicates a VFT law, it is widely accepted that VFT relaxation requires the measurement of the temperature

dependence of actual resonances [211]. In our experiments, we make use of strong polarization-strain resonances, such as the one at $\nu = 640$ KHz at $290K$ reported in Fig. 2.5(d), tagged as principal polarization-strain resonance. Detecting this resonance frequency for different values of T allows the direct quantification of T_0 in the VFT law. We found $T_0 = (282 \pm 2)$K; this value of the freezing temperature is compatible with the optical one, implying that dipolar fluctuations are governed by an effective cold temperature, as observed through the anomalous electro-optic effect. However, the whole picture we have presented does not apply to any disordered ferroelectric crystal, since compounds with small variations in concentrations can manifest completely different behaviors [50]. In the next Chapter 3 we study a ferroelectric KLTN sample in which relaxor behavior play a minor role, especially because it is superseded by a completely new phenomenon having in macroscopic coherence its signature.

2.4 Future developments

To conclude, we point out some development points. A first perspective relies in the investigation of the electro-optics of disordered ferroelectric crystals presenting directional disorder [209]. This implies a polarization response strongly dependent on the direction of the applied field and propagation axis. Dipolar reorientation may be constrained on specific crystalline planes and optical experiments may give a mesoscopic insight in the directional-dependent macroscopic response. This is especially true if experiments are extended deep into the ferroelectric phase ($T < T_m$), where, in specific configurations, we have preliminary evidence of new electro-optical functional states with relevant applicative implications in the field of phase-change materials [298, 293, 307]. The main breakthrough would be the demonstration of the giant electro-optic effect in optically-integrated settings such as disordered ferroelectric waveguides [127, 141]. In fact, on-chip electro-optical modulators are of central importance in nonlinear optics, laser technology, quantum optics and optical communications and represent a challenge since high driving voltage are usually required [210, 306]. Although the response directly associable to PNRs is expected to decrease with the external field frequency [271], the giant electro-optic effect in KTN-based integrated structures may lead to efficient light modulation at GHz frequencies with low applied voltage.

Chapter 3

Super-crystals in composite ferroelectrics

In this Chapter we report the discovery of spontaneous polarization super-crystals in microstructured disordered ferroelectric samples [219]. Generally, textbook models of global symmetry breaking include a low-symmetry low-temperature state with a fixed infinitely extended coherence. In contrast, the spontaneous polarization observed as spatial inversion symmetry is broken during a paraelectric-ferroelectric phase-transition generally leads to a disordered mosaic of polar domains that permeate the finite samples [230]. Coherent and ordered ferroelectric states with remarkable properties of both fundamental and technological interest [62, 162, 114] can emerge when ferroelectricity is influenced by external factors, such as system dimensionality [77], pressure and strain gradients [52, 53, 32], electrostatic coupling [43, 51] and magnetic interaction [25]. We report the spontaneous formation of an extended coherent three-dimensional (3D) superlattice in the nominal ferroelectric phase of specifically grown potassium-lithium-tantalate-niobate (KLTN) crystals [6, 231]. Visible light propagation reveals a polarization "super-crystal" with a micrometric lattice constant, a counterintuitive mesoscopic phase that naturally mimics standard solid-state structures but on scales that are thousands of times larger. To grasp the phenomenon we consider disordered ferroelectrics presented in Chapter 2 but from a more general point of view. At one given temperature, these have the interesting property of a manifesting a single perovskite phase whose dielectric properties depend on the specific composition [295, 239]. For example, a compositional gradient along the pull axis leads to a position-dependent Curie point $T_C(\mathbf{r})$, so that for a given value of crystal temperature T a phase separation occurs, with the regions where $T > T_C$ being paraelectric and those with $T < T_C$ developing a spontaneous polarization [273]. Specifically tailored growth schemes are even able to achieve an oscillating T_C along a given direction, say the x-axis [7, 198]. In these conditions, we can expect that at a given T in proximity of the average (macroscopic) T_C, the sample will be in a hybrid state with alternating regions with and without spontaneous polarization. Crossing the Curie point, in conditions in which tetragonal polar-domains pervade the volume forming 90 °configurations to minimize the free-energy associated to polarization density charge [230], this oscillation can stabilize in the whole volume and form a full three-dimensional periodic structure.

3.1 Observation of a super-crystal ferroelectric phase

3.1.1 Experimental methods

We consider a compositionally disordered ferroelectric of $K_{1-\alpha}Li_\alpha Ta_{1-\beta}Nb_\beta O_3$ with $\alpha = 0.04$ and $\beta = 0.38$, grown through the top-seeded solution method by extracting a zero-cut $2.4^{(x)}x2.0^{(y)}x1.7^{(z)}mm$ optical quality specimen. It shows, through low-frequency dielectric spectroscopy measurements, the spatial-averaged Curie point, which signals the transition from the symmetric paraelectric phase to the low-temperature ferroelectric phase, at the room-temperature $T_C = 294K$. A one-dimensional seed microstructure is embedded into the sample as it is grown through the off-center growth technique with periodically oscillating niobium compositions so as manifest a sinusoidal variation in the low-frequency dielectric constant, and thus in the critical temperature T_C, along the growth-axis (x-direction) [198, 8]. We note that the composition amplitude of the periodic microstructure can be estimated from $\Delta\beta/\Delta T$, where $\Delta\beta$ is the amplitude variation in niobium composition and ΔT is the change in the growth temperature incurred by the off-center rotation. At the growth temperature of approximately $1470K$, the ratio $\Delta\beta/\Delta T \approx 0.35$ ‰·mol/K has been extracted from the phase diagram of KTN. The temperature variation incurred by the off-center rotation was measured to be $3K$, from which we obtain $\Delta\beta \approx 1.05$ ‰·mol. This dielectric volume microstructure causes an index of refraction oscillation of period $\Lambda = 5.5\mu m$, that is able to diffract light linearly and electro-optically as shown in section 1.3.2. In the present experiment the macroscopic linear and electro-optic diffractive properties of the crystal have been investigated launching low-power (mW) plane waves at $\lambda = 532nm$ that propagate normal and parallel to the grating vector $\boldsymbol{\Gamma}$ ($\Gamma = 2\pi/\Lambda$), that is along the x-direction (Fig. 3.3(a)). Light diffracted by the medium is detected using a broad-area CCD camera placed at $d = 0.2m$ from the crystal output facet or collected into Si power-meters. In real-space measurements (Fig. 3.2(d-h)) the output crystal facet is imaged on the CCD camera and a cross-polarizers setup (section 2.2) has been used to highlight contrast due to polarization inhomogeneities. The time needed to obtain a fully-correlated state corresponding to the 3D super-crystal depends on the cooling rate τ and on the details of the thermal environment, as well as on the specific crystal investigated. For instance, in another KNTN sample, despite the microstructure is characterized by a broader spatial spectrum, we have found this time greatly reduced. Considering, for instance, as a thermal protocol a cooling rate $\tau = 0.05K/s$ and an environment at $T = T_C + 1K$ (weak thermal gradients), we have found that the metastable 1D lattice state at $T = T_C - 2K$ (Fig. 3.2(b)), in which correlations involve mainly the direction including the $\boldsymbol{\Gamma}$ vector, lasts approximately 1hr. In this stage, although no macroscopic order occurs in the other directions [154], we observe optimal optical transmission of the sample; output light is not affected by scattering related to the existence of random domains and this further underlines the presence of a mesoscopic ordering process in which the typical domain size is set. As regards the inspected temperature range, we have found that the super-crystal forms for temperatures till to $T = 288K$, although correlations are weaker at the lower temperatures. This is consistent with the fact that at these temperatures also the regions with a lower local T_C are well below the transition point.
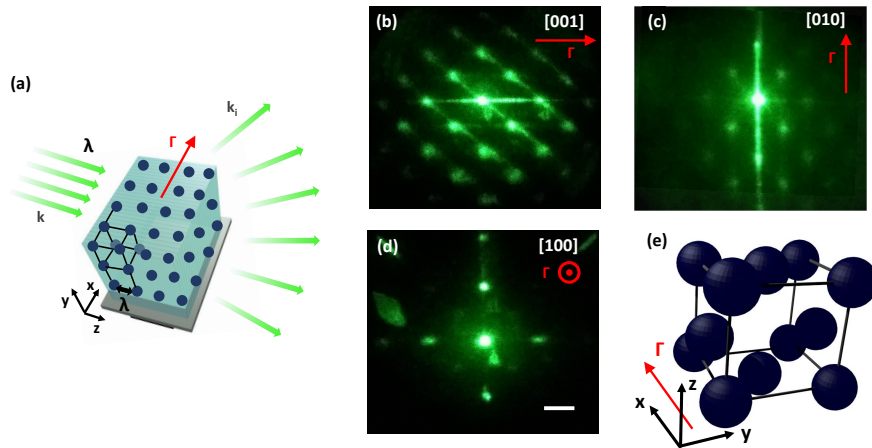
Figure 3.1. Super-crystal in the ferroelectric phase. (a) Sketch of visible-light diffraction from micrometric structures through a transparent crystal and (b-d) 3D superlattice probed at $T = T_C - 2K$ along the principal symmetry direction of the crystal, respectively with the incident wavevector **k** parallel to (b) z-direction, (c) y-direction and (d) x-direction. Crystallographic analysis reveals the elementary cubic structure of lattice constant Λ shown in (e). Scale bar corresponds to $1.2cm$. (From [219]).

3.1.2 Linear diffractive behavior

According with the experimental methods detailed herebefore, when the crystal is allowed to relax at $T = T_C - 2K$, i.e., in proximity of the spatially averaged room-temperature Curie point $T_C = 294K$, laser light propagating through the sample suffers relevant scattering with strongly anisotropic features. Typical results are reported in Fig. 3.1(b-d), and appear as an optical analogue of x-ray diffraction in low-temperature solids. This "optical diffractometry" provides basic evidence of a 3D superlattice at micrometric scales. Probing the principal crystal directions reveals several diffraction orders that map the entire reciprocal space. The large-scale super-crystal, that permeates the whole sample, overlaps - along the x-direction - with the built-in compositional oscillating seed. The superlattice extends in full three-dimensions, with the same periodicity $\Lambda = 5.5\mu m$ of the x-oriented compositional oscillation, also along the orthogonal y and z-directions. In particular, Fig. 3.1(d) indicates that in the plane perpendicular to the built-in dielectric microstructure **Γ** vector, i.e., where spatial symmetry should be unaffected by the microstructure in composition, the ferroelectric phase-transition leads to a spontaneous pattern of transverse scale Λ. The corresponding elementary structure on micrometric spatial scales is reported in Fig. 3.1(e); it can be represented as an fcc-cubic structure in which the occupation of one of the three faces ($z - y$ face) is missing [232]. The structure, which is, to our knowledge, not observed at atomic scales, can be reduced to a simple cubic structure with a three-fold basis and lattice parameter $a = \Lambda$. As the KLTN crystal is brought below the average Curie point, it manifests a metastable (supercooled) and a stable (cold) phase, as analyzed in Fig. 3.2 both in the reciprocal (Fourier) and direct (real) space. In the nominal
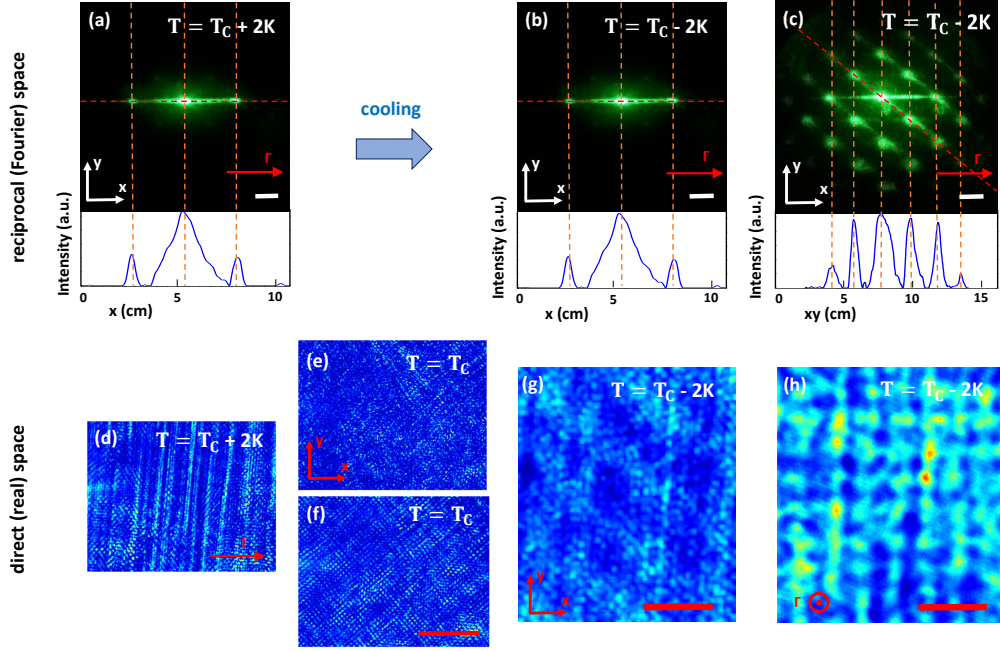
Figure 3.2. Light diffraction in microstructured KLTN above and below the Curie point: observations in Fourier (top) and real (bottom) space. (a) Reciprocal space probed at $T = T_C + 2K$, showing the first diffraction orders due to the one-dimensional sinusoidal compositional modulation. Cooling below the critical point results at $T = T_C - 2K$ in (b) a supercooled 1D superlattice with the same diffraction orders that relaxes at steady-state into (c) the super-crystals. Both in (b) and (c) the direction of incident light is orthogonal to $\mathbf{\Gamma}$, as in (a). (d-h) Corresponding transmission microscopy images revealing (d) unscattered optical propagation, (e-f) scattering at the phase transition, (g) unscattered optical propagation in the metastable superlattice and (h) periodic intensity distribution underlining the 3D superlattice. Metastable and stable (equilibrium) phases are inspected respectively at times $t \approx 1min$ and $t \approx 1hr$ after the structural transition at $T = T_C$. Bottom profiles in (a-c) are extracted along the red dotted line. Scale bars correspond to (a-c) 1.2cm, (d-f) 200μm and (g-h) 10μm. (From [219]).

paraelectric phase, at $T = T_C + 2K$ (Fig. 3.2(a)), we observe the first Bragg diffraction orders (± 1) consistent with the presence of the seed microstructure, a one-dimensional transverse sinusoidal modulation acting as a diffraction grating [242, 292]; the distance from the central 0-order fulfills the Bragg condition, that is, scattered light forms an angle $\theta_B = \lambda/2n\Lambda \simeq 7°$ with the incident wavevector $\mathbf{k}$. Crossing the ferroelectric phase-transition temperature T_C (see section 3.1.1) we detect a supercooled metastable state that has an apparently analogous diffraction effect (Fig. 3.2(b)) that is dynamically superseded by the stable and coherent cold superlattice phase (Fig. 3.2(c)), in which spatial correlations are extended to the whole crystal volume. In real space, transmission microscopy shows unscattered optical propagation through the paraelectric sample at $T = T_C + 2K$ (Fig. 3.2(d)), that turns into critical opalescence and scattering from obliques random domains at the structural phase transition (Fig. 3.2(e-f)), and in unscattered transmission
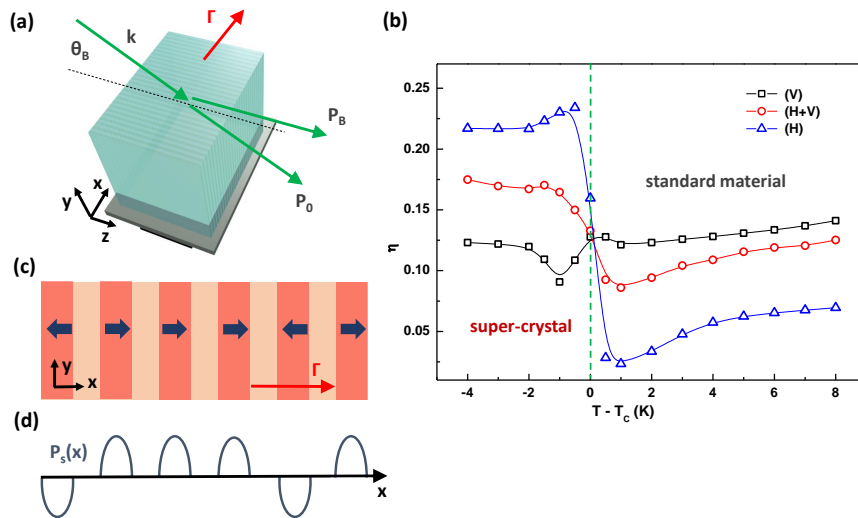
**Figure 3.3.** Diffractive behavior of the 1D supercooled superlattice. (a) Sketch of the experimental geometry and (b) detected diffraction efficiency (dots) as a function of temperature in proximity of ferroelectric transition for different wave polarizations. An anomaly appears crossing T_C for H-polarized light signaling the emergence of the super-crystal. Lines are interpolations serving as guidelines. (c) Scheme of the periodically-ordered ferroelectric state along the x-direction underlying the super-crystal for $T < T_C$ and giving the spontaneous polarization $P_S(x)$ sketched in the bottom inset. (From [219]).

in the metastable ferroelectric phase at $T = T_C - 2K$ (Fig. 3.2(g)). After dipolar relaxation has taken place, the cold super-crystal appears in this case as a periodic intensity distribution on micrometric scales, as shown in Fig. 3.2(h).

To further analyze these supercooled and cold phases, we inspect the supercooled one-dimensional phase (Fig. 3.2(b)) that is accessible through linear (unbiased) and electro-optic (biased) polarization-resolved Bragg diffraction measurements. In particular, referring to the setup illustrated in Fig. 3.3(a), we measure the diffraction efficiency $\eta = P_B/(P_B + P_0)$, where P_B and P_0 are respectively the diffracted and non-diffracted power, in the first Bragg resonance condition, i.e., with the incident wavevector **k** forming the angle θ_B respect to the z-axis. The diffraction efficiency η is reported in Fig. 3.3(b) for different input light polarization and temperature across the average Curie point. Diffraction strongly depends both on the nominal crystal phase and on the polarization of the incident wave: a large increase in η is found for light polarized in the x-z plane (H-polarized). For $T > T_C$ the dependence on light-polarization is consistent with what expected in standard periodically index-modulated media (wave-coupled theory), that is, a weak temperature dependence and a maximum η for light polarized normal to the grating vector (V-polarized). In this case, the difference in η_H and η_V can be related to the different Fresnel coefficient governing interlayer reflections and is congruently $\eta_V > \eta_H$ by an amount that decreases for larger θ_B [294, 153]. Consistently, the (H+V)-polarized curve, that is when the input linear polarization is at 45 °with respect to the H and V polarizations, falls between these two curves. Standard behavior is violated for $T < T_C$, where a

large enhancement in η_H rapidly leads to an anomalous regime with $\eta_V < \eta_H$. The physical underpinnings of this behavior can be grasped considering the simple model illustrated in Fig. 3.3(c). Here we consider the metastable 1D superlattice (Fig. 3.2(b)) before tensorial effects cause the full 3D superlattice relaxation (Fig. 3.2(c)). Specifically, for a given T, regions with a local value of T_C such that $T < T_C$ (dark shading) will manifest a finite spontaneous polarization $P_S \neq 0$, whereas region with $T > T_C$ (light shading) will have a $P_S \simeq 0$. Optical measurements are sensitive only to the square of the crystal polarization $\langle \mathbf{P} \cdot \mathbf{P} \rangle \simeq P_S^2$ through the resulting index pattern modulated via the quadratic electro-optic response $\delta n(P) = -(1/2)n^3 g P^2$ (section 2.2), where n is the unperturbed refraction index and g is the proper perovskite electro-optic coefficient [35]. Enhanced Bragg-scattering of light polarized parallel to the seed direction $\boldsymbol{\Gamma}$ (H in Fig. 3.3(b)) indicates that $P_S(x)$ is parallel to the seed direction (x-axis), where the electro-optic coefficient g have its maximum value $g = 0.16 m^4/C^2$. The resonant response at θ_B and the absence of higher harmonics indicates that this $P_S(x)^2$ distribution is sinusoidal with wavevector $\boldsymbol{\Gamma}$. Hence, although in general it may be that macroscopically $\langle \mathbf{P} \rangle \simeq 0$, it turns out that $\langle \mathbf{P}^2 \rangle \simeq P_S^2 \neq \langle \mathbf{P} \rangle^2 \neq 0$ on the micrometric scales, in analogy with the optical response emerging in crystals affected by polar-nanoregions that we have discussed in Chapter 2. Optical diffraction efficiency reported in Fig. 3.3(b) thus occurs considering $\eta = \sin^2\left(\frac{\pi d(\delta n)}{\lambda \cos \theta_B}\right)$, with resonant enhanced diffraction for $T < T_C$ caused by $\delta n = \delta n_0 + \delta n(P)$, where $\delta n_0 \sim 10^{-4}$ is the polarization independent index change due to the periodic composition variation (Sellmeier's index change).

3.1.3 Electro-optical diffraction analysis

To validate this picture we perform electro-optic diffractometry experiments, in which a macroscopic polarization activating the nonlinear periodic response is induced via an external static field E applied along x. Results are reported in Fig. 3.4; in particular, in Fig. 3.4(a) the polarization and field dependence of η is shown at $T = T_C + 2K$. We observe a nearly field-independent behavior for V-polarized light, that arises from its low electro-optic coupling (bias field and light polarization are orthogonal, $g = -0.02 m^4/C^2$); differently, η_H increases with the field showing a "discontinuity" at the critical field $E_C = (1.4 \pm 0.1)$ kV/cm. The strong similarity between this enhancement and those observed in unbiased conditions at T_C (Fig. 3.3(b)) indicates that E_C coincides with the coercive field and the discontinuity corresponds to the field-induced phase-transition [311, 288]. In fact, in Fig. 3.4(b) we repeat this experiment enhancing the experimental field-sensitivity and acquiring data also for decreasing field amplitudes. The result is a partial-hysteretic loop for the diffraction efficiency that demonstrates the field-induced transition and underlines that, both in the linear and nonlinear (electro-optic) case, the effect of the seeded ferroelectric ordering is to provide a periodic spontaneous polarization along x. We also note a slight asymmetry with respect to positive/negative fields; this is associated to a residual fixed space-charge field that may play an important role in the spontaneous polarization alignment process and hence in leading to a residual $\langle \mathbf{P} \rangle \neq 0$. The existence of a periodic spontaneous polarization distribution in the superlattice (Fig. 3.3(c)) is confirmed in Fig. 3.4(c), where electro-optic Bragg diffraction below T_C is reported. An oscillating full-hysteretic behavior is observed

as a function of the external field, consistently with the prediction

$$\eta(E) = \sin^2\left(\frac{\pi d(\delta n(E))}{\lambda \cos \theta_B}\right), \tag{3.1}$$

$$\delta n(E) = \delta n_0 + (1/2)n^3 g(P_S^2 + 2\varepsilon_0 \chi \langle P_S \rangle E + \varepsilon_0^2 \chi^2 E^2). \tag{3.2}$$

The increase in η due to the superlattice polarization allows us to explore its full sinusoidal behavior, that usually requires extremely large fields in the paraelectric phase and reduces to a parabolic behavior [292], as shown in Fig. 3.4(d). From this parabolic behavior detected at $T = T_C + 5K$ we estimate that the resulting amplitude in the point-dependent Curie temperature due to the compositional modulation is $\Delta T_C \simeq 2K$, a value consistent with that estimated from the growth process (section 3.1.1). Agreement with the periodic polarization model is further stressed by deviations emerging in $\eta(E)$ especially for low and negative increasing fields, where the dependence on $\langle P_S \rangle$ make observations weakly dependent on the specific experimental realization.
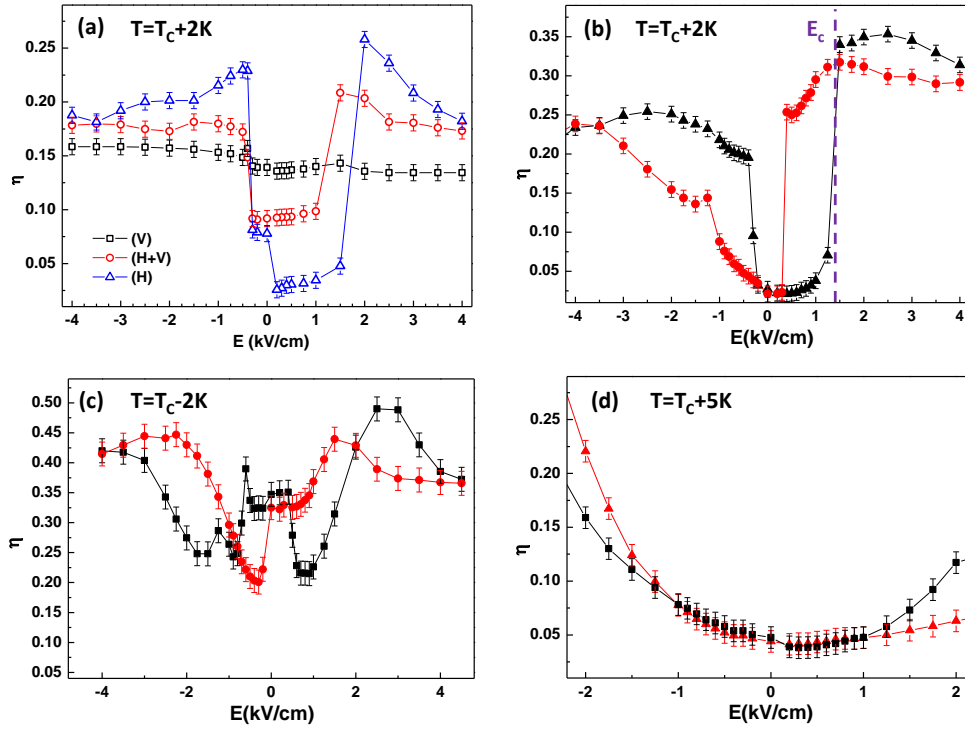
Figure 3.4. Electro-optic Bragg diffraction in the critical region. (a) Diffraction efficiency as a function of the external applied field for different light polarization at $T = T_C + 2K$; (b) hysteresis loop at the same temperature and (c) at $T = T_C - 2K$ for H-polarization. (d) Expected [7] weak-hysteretic paraelectric (parabolic) behavior at $T = T_C + 5K$. In (b-d) black dots and red dots indicates data obtained respectively increasing and decreasing the bias fields. Lines are interpolations serving as guidelines. (From [219]).
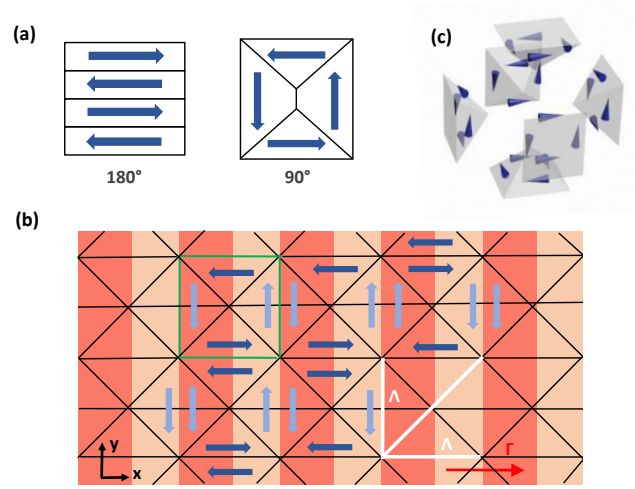
Figure 3.5. Polar-domain configuration underlying the 3D superlattice. (a) Typical 180°and 90°domain configurations in perovskites ferroelectrics. (b) Planar domain arrangement scheme in the stable super-crystal phase obtained with elementary blocks of 90°configurations (green cell). In this periodically-ordered ferroelectric state the compositional modulation (as for Fig. 3.3(c)), other domain walls ruling optical diffractometry (black lines), and periods along x,y and xy-axis (white bars) are highlighted. Vertical polarizations have a lighter color to stress their weak optical response in our KLTN sample. (c) Extension of the single "unit-cell" (green cell in (b)) in three dimensions. (From [219]).

3.2   Ordered polar-domain configuration

An interesting point arising from the experimental results and analysis is how the periodically-ordered polarization state along the x-direction leads to the super-crystal. Since we pass spontaneously from a metastable to a stable mesoscopic phase, polar-domain dynamics in presence of the fixed spatial scale Λ play a key role. In fact, we note that the 1D superlattice sketched in Fig. 3.3(c) involves the appearance of charge-density and associated strains between polar planes, so that the ferroelectric crystal naturally tends to relax into a more stable configuration. In standard perovskites, equilibrium configurations are mainly those involving a 180°and 90°orientation between adjacent polar domains, as schematically shown in Fig. 3.5(a). To explain the 3D polar-state and its periodical features underlying the super-crystal, we consider the 90°configuration, which is characterized by 45°domain walls that we observe in a disordered configuration during the ferroelectric phase transition at T_C (Fig. 3.2(f)). Due to the periodic constraint along the x-axis, this arrangement has the unique property of reproducing our observations, minimizing energy associated to internal charge-density, and transferring the built-in 1D order to the whole volume with the same spatial scale Λ. We illustrate the domain pattern in Fig. 3.5(b) for the $x - y$ plane, whereas in Fig. 3.5(c) the elementary cell is shown in the three-dimensional case, where it maintains its stability features in terms of charge-density energy. In particular, in Fig. 3.5(b), domain walls resulting in the diffraction orders of Fig. 3.1(b) are marked, as well as the 45°correlation

period, that agree with optical observations of the reciprocal space. We further stress that vertical domains (light blue in Fig. 3.5(b)) are optically analogous to paraelectric regions; moreover, 180°rotations in the polarization direction in each polar region has no effect on the optical response. In view of the symmetry of this arrangement, the observed diffraction anisotropy is then associated to the absence of grating-planes in the $y-z$ face. Further insight on the 3D domain structure requires numerical simulations based on Monte Carlo methods [166] and phase-field models [58, 167, 65, 168]; they may confirm our picture and reveal new aspects for ferroelectricity, such as polar dynamics, spontaneous long-range ordering and the role of polar strains in composite ferroelectrics with built-in compositional microstructures. In fact, the effect of the composition profile is here crucial in triggering the spontaneous formation of the macroscopic coherent structure, as it sets the typical domain size along the x-direction and so rules the whole dynamic towards the equilibrium state. We expect that a different amplitude and period of the modulation may affect the formation, stability, time- and temperature-dynamics of the super-crystal; indeed, these parameters of the compositional gradient may be important in determining the interaction between polar-regions. Advanced growth techniques [7] can open future perspectives in this direction, as well as towards composite ferroelectrics with different compositional shapes of fundamental and applicative interest. However, we have evidence that quasi-periodic microstructure in KNTN samples can also lead to analogues super-crystal phases ruled by their main spatial frequency. This suggest that a similar type of ordering is a general property of ferroelectric domains in potentials having a built-in periodicity. In this regards, we note that similarly ordered new ferroelectric phases has been recently observed through atomic scale imaging in layered oxide thin films [265]. Our results show how ferroelectricity can be arranged into new phases on macroscopic scales, a finding that sheds light on fundamental issues in strongly-correlated condensed matter systems and also suggests methods to predict and engineer new states of matter. They open new avenues in the optical exploration of critical properties and large-scale structures in disordered systems. In particular, we are developing two main activities in this direction. The first concerns direct investigation of domains structure through polarization-resolved transmission measurements, i.e., resolving local ferroelectric order and PNRs arrangement from the polarization state of light obtained through Stokes analysis. The other involves the nonlinear (inelastic) response of ferroelectric super-crystal phases, which can be probed via second harmonic generation (SHG) [30, 278, 283, 235, 106, 24]. In this case, the interplay between random quasi-phase matching and large-scale ferroelectric period can results into new interesting phenomena.

PART II

Nonlinear wave dynamics in photorefractive ferroelectrics

Chapter 4

Rogue waves in photorefractive ferroelectrics

Using the critical response of disordered ferroelectrics we investigate nonlinear optical propagation in unstable and stochastic regimes. This allows us to report the first observation of rogue waves in nonlinear wave propagation in photorefractive crystals [220], which is the subject of this Chapter. The basis for spatial rogue waves understanding are placed through numerical and theoretical considerations. Predictability of the observed extreme events is analyzed in comparison with hydrodynamics data using statistical mechanics methods and reveals an analogous correlated stete characterized by highly-complex dynamics.

4.1 Rogue waves in different physical contexts

Processes that lead to long-tail statistics are of great interest in physics because they allow the observation of events with giant amplitudes that would otherwise be truly rare and unobservable in systems that follow standard distributions. This typically occurs in phenomena that manifest complex dynamics, such as in the appearance of earthquakes in plate motion or in large-scale breakdowns in networks [69]. Extreme events profoundly affect properties and response of complex systems, such as in financial market [310], data stream [282], biological reactions [274] and human vision [187]. Long-tail statistics are also observed in waves, in which case the giant perturbations with extreme amplitudes are known as "Rogue Waves". Originally studied in ocean dynamics where their origin and properties are largely unknown [150], they have now been observed in a variety of different wave-supporting systems and have been shown to present common features also when different physical mechanisms specific for each system are involved in their generation [199]. Universal statistical traits and general model equations based on the generalized NLSE have fuelled particular research efforts in optics [258, 95, 13], where abnormal pulses can be exploited for applications [163] and various systems promise to be used as test benches to study the origin and properties of their not well understood oceanic counterpart [4, 102]. In particular, long-tail statistics have been observed in various optical systems, from nonlinear pulse propagation in optical fibers [259, 112, 194, 66] to beam filamentation [177, **?**, 33] and dissipative resonators [161, 70, 202, 173].

Several physical ingredients underlying the occurrence of long-tail statistics have been identified, such as interacting coherent structures emerging form stochastic instabilities [200, 201, 252, 12, 20, 275], interference for inhomogeneous random wave fields [19, 140, 170, 186], wave-turbulence in incoherent nonlinear propagation [115, 133, 233, 290, 234, 71, 263, 267] and spatiotemporal chaos in cavity dynamics [39, 226, 203, 184, 250]. In spatially extended systems, instabilities have been shown as key in leading to rogue events in the transverse plane of the optical light beam. Here, the presence of blocked or induced disorder or, generally speaking, of an interplay between a non-equilibrium state and a nonlinear mechanism, appears a crucial ingredient to extreme event generation, providing interaction and coupling of different spatial regions [191]. The central role of disorder seems to rule out rogue waves in systems that form the technological basis of photonics, that is, optical crystals with χ_2, χ_3, and photorefractive response, since a stochastic component is in principle absent [44]. To date, no rogue waves have ever been detected in any of these crystals. Considering photorefractives, without feedback mechanisms [185], disorder is known to play a minor role in light propagation in standard crystal phases [262]. However, we have seen how a disordered ferroelectric cooled to its Curie point, possess long-range fluctuations leading to transient out-of-equilibrium states characterized by reorienting polar-nanoregions that affect light through a strongly enhanced electro-optic response. In these conditions, characterized by disorder and nonlocality in light self-interaction, the complexity of multi-soliton spatial dynamics has also been predicted [73]. This combination of disorder and giant nonlinearity allows us to observe spatial rogue waves in photorefractive crystals of potassium-lithium-tantalate-niobate (KLTN). The localized and anomalously intense light spots form when the crystal is biased at the ferroelectric phase-transition, where optical Kerr-saturated nonlinear propagation is affected by huge stochastic response.

4.2   Spatial rogue waves in photorefractive ferroelectrics

We discuss the observation of rogue waves as light propagates in the extreme nonlinear regime that occurs when a photorefractive ferroelectric crystal is in proximity of its structural phase-transition. The transmitted spatial light distribution contains bright localized spots of anomalously large intensity that follow a signature long-tail statistics that disappears as the nonlinearity is weakened. The isolated wave events form as out-of-equilibrium response and disorder enhance the Kerr-saturated nonlinearity at the critical point. Numerical simulations of the generalized nonlinear Schrödinger equation suggest that dynamics of soliton fusions can microscopically play an important role in the observed rogue intensities and statistics, whereas a study of the self-similarity associable to the individual observed filaments revealas that the expected scale-invariance condition does not hold for these solitons.

4.2.1   Observation of optical extreme events

Light propagation at the phase-transition is investigated focusing cylindrical (1D) gaussian beams ($\lambda = 532nm$, P= $0.1mW$, FWHM= $8\mu m$) on a photorefractive disordered crystal of KLTN, $K_{1-\alpha}Li_\alpha Ta_{1-\beta}Nb_\beta O_3$, with $\alpha = 0.04$ and $\beta = 0.38$, illuminated through uniform background intensity I_b. The zero-cut optical quality
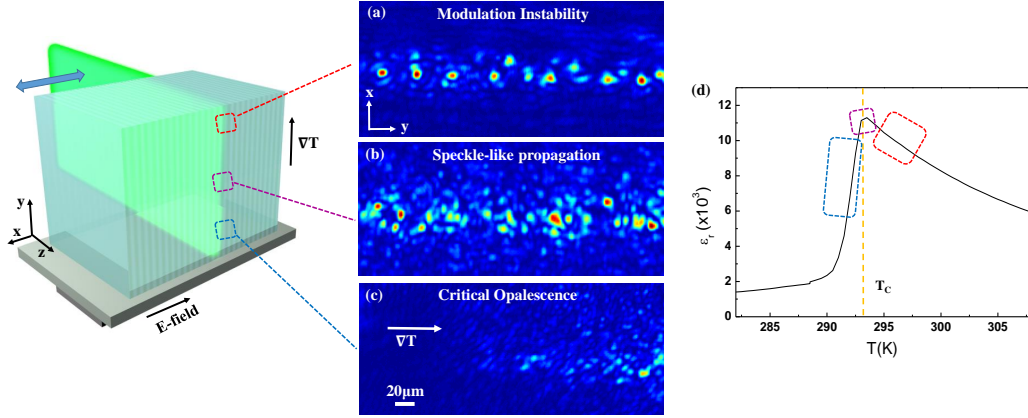
Figure 4.1. Nonlinear beam propagation in photorefractive KLTN biased in proximity of the ferroelectric phase-transition. (left) Sketch of the experimental geometry and (right) different local nonlinear propagation regimes selected by the thermal gradient. Transmission microscopy images revealing (a) quasi-periodic pattern (modulation instability), (b) speckle-like propagation and (c) critical opalescence. (d) Corresponding temperature-dependent dielectric response of the sample (temperature hysteresis is omitted). (From [220]).

specimen is $2.4^{(x)}$x$2.0^{(y)}$x$1.7^{(z)}mm$ sized and presents the paraelectric to ferroelectric phase-transition at the room-temperature Curie point $T_C = 294K$, measured and characterized using low-frequency dielectric spectroscopy (Fig. 4.1(d)). In our experiment, we keep the KLTN crystal at $T = T_C + 1K$ through a Peltier junction; then, an external static electric field is applied along the x-direction, parallel to the polarization of the propagating beam (Fig. 4.1(left)), via an applied voltage V=500V. In proximity of T_C an electric field larger than the coercive field is able to induce ferroelectric ordering (field-induced transition). The crystal manifests a temperature gradient in the vertical y-direction caused by the setup geometry (as in Fig. 4.1(left) the Peltier junction is placed on the bottom facet and the thermal capacity is large in proximity of T_C). Launching a z-directed beam with a spatial extension in the y-direction hence allows the inspection of light propagation for different temperature regimes in a single experiment. The nonlinearity is thus controlled through the local temperature and nonlinear beam propagation is explored detecting the transmitted beam intensity distribution through an imaging system and a CCD camera. Results indicate a strong dependence on the local temperature. In fact, the spatial scale of the thermal gradient ($\approx 300\mu m$) is such that three qualitatively different regimes of light propagation can be identified, as shown in Fig. 4.1(right). When the crystal is warmer the bias field is too weak to induce the ferroelectric transition and the local phase remains paraelectric; here modulation instability associated to the strong photorefractive response governs nonlinear dynamics, breaking, along the initially symmetric y-direction, the beam into a periodic pattern of (2+1)D beams and inhibiting (1+1)D soliton formation (Fig. 4.1(a)). The properties of this stage are investigated in Chapter 5 with a setup that allows finest control of the nonlinearity. When the crystal is slightly colder, ferroelectric ordering occurs and
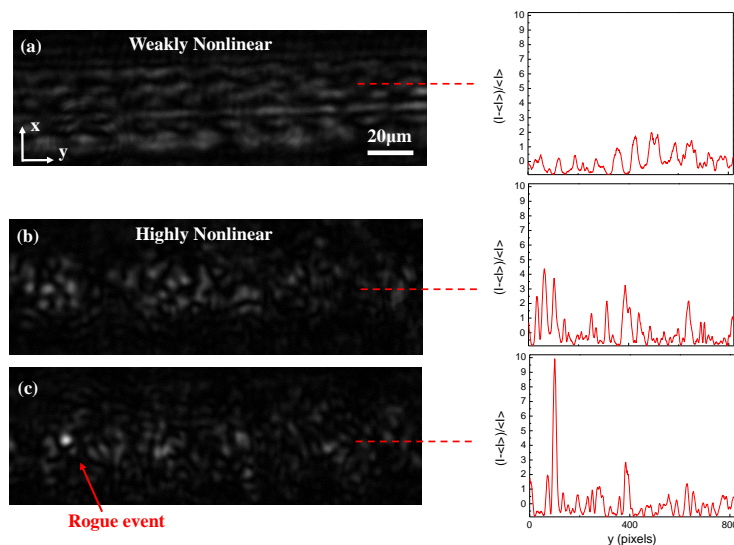
Figure 4.2. Light intensity distribution transmitted through the biased photorefractive crystal exactly at the critical point. (a) Disordered pattern in the weakly nonlinear regime with the inset showing spatial intensity fluctuations along the red dashed y-line. (b-c) Speckle-like pattern in the highly nonlinear regime, where the effect of large intensity fluctuations strongly affects the nonlinear dynamics. In (c) is reported an observation involving a bright spot with extreme intensity (approximately twenty times the averaged intensity), specified as rogue event. (From [220]).

light transmission is inhibited by critical opalescence (Fig. 4.1(c)). Between these two conditions we find propagation associated to the coexistence point, corresponding to an effective local temperature that is exactly T_C. In this case, a disordered index of refraction pattern forms over spatial scales comparable with λ, introducing scattering and fragmentation in the nonlinear propagation, with the formation of narrower interacting filaments. What emerges is a disordered output intensity distribution $I(x, y)$ with micrometric spots of various intensity that is "speckle-like" [119]. In order to study the statistical properties of the speckle-like intensity pattern, we first quantify the intensity fluctuations amplitude in the spatial light distribution introducing the deviation $(I(x, y) - \langle I \rangle)/\langle I \rangle$ from the spatial mean value $\langle I \rangle$. Large deviations are observed in the disordered output of this highly nonlinear regime with the appearance of bright micrometric spots of extreme intensity. In Fig. 4.2(b-c) we report, as an example, two measured speckle-like outputs with the associated fluctuations along a y-direction in the insets; in Fig. 4.2(c) we show an instance of an extreme event, spatially localized, with a peak intensity of approximately twenty times larger than the averaged intensity. The measured transverse dimension (FWHM) of this exceedingly bright micro-beam is $3 \mu m$, according with the enhanced self-focusing picture in critical conditions [68]. Further analysis reported hereafter indicates this event as a rogue wave. The disordered pattern with rogue fluctuations is observed at steady state after an initial transient stage that lasts $t \approx 10s$ for the μW beam power used. During the transient, the beam diffracts in an inhomogeneous setting, associated to linear sample disorder, as it reaches the crystal output facet. The typical spatial distribution in this "weakly" nonlinear regime is shown in Fig.

4.2(a), with the inset showing the smaller intensity fluctuations in this condition. This regime is superseded at subsequent times by the appearance of modulation instability and break-up, where disorder appears to have a dynamic and strongly amplified effect on light, which then leads to the final steady-state highly nonlinear regime, at $t \approx 100s$, where rogue waves are detected. This transient nature is related to the physics of the photorefractive nonlinearity, which involves a build-up of a photogenerated space-charge field, so that the beam-induced index of refraction modulation accumulates in time. In Chapter 5 we exploit this property to study in details the whole process as a function of the nonlinearity. However, once the steady condition has been reached, the beam continues to experience stationary continuous spatiotemporal fluctuations associated to the non-equilibrium features and long-range correlations in the refractive index at the Curie point. So we observe the speckle-like pattern to vary dynamically under the action of different disorder configurations.

We have acquired a large set of uncorrelated images (approximately 10^3) in the same experimental conditions but with different intrinsic disorder landscapes. Histograms of the intensity values in a transverse region of the image for linear and nonlinear propagation then allow us to measure the corresponding probability distribution functions $P(I)$. Results are shown in Fig. 4.3, where the intensity statistics observed for the highly nonlinear speckle-like pattern is compared to that observed for the weakly nonlinear regime. In both cases the so called incoherent part, which is related to random correlations between independent measurements [119], is of the order of the background intensity I_b and is not shown. Long-tail statistics characterize the steady-state highly nonlinear condition, as reported in Fig. 4.3(a). The experimental behavior strongly deviates from a gaussian distribution, that implies a decay according to $P(I) = \exp(-I/\langle I \rangle)/\langle I \rangle$ that we have evaluated
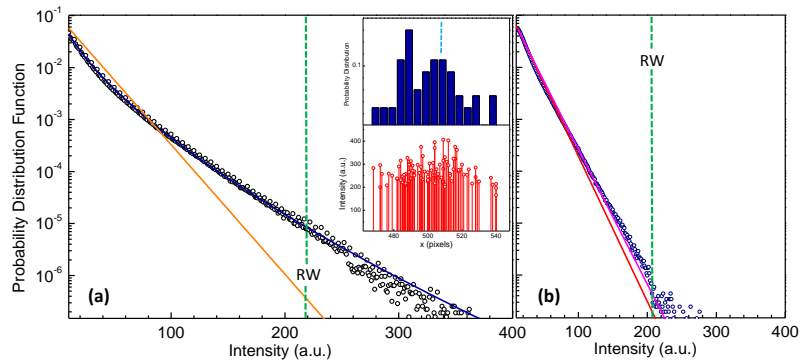
Figure 4.3. Intensity distribution statistics. (a) Long-tail statistics in the highly nonlinear regime: experimentally revealed (black circles), fitting function (blue line) and consistent gaussian distribution for comparison (orange line). The inset shows the spatial x-position of several observed rogue events (bottom) with the corresponding counts histogram (top). (b) gaussian statistics in the weakly nonlinear regime: experimentally revealed (blue circles), fitting function (magenta line) and consistent gaussian distribution for comparison (red line). The vertical green dotted lines indicate the rogue waves (RW) thresholds. (From [220]).

with the measured $\langle I \rangle$ value (orange line) [19]. In particular, the observed intensity distribution is well fitted by a stretched exponential decay (blue line) in the form of $P(I) = \exp\left(-cI^b - a\right)$. The stretching parameter b quantifies the deviation from gaussianity and long-tailed behavior is indicated by $b < 1$ [69]. We obtain $b = 0.65 \pm 0.02$ demonstrating that extreme intensity occurs with heavy-probability. To further analyze the "rare" events, we calculate the significant wave height, defined as the mean amplitude of the highest one-third of detected waves. Events of amplitude exceeding at least by a factor of two this value are commonly referred to as rogue waves (hydrodynamic threshold) [95]. Setting the threshold in Fig. 4.3 (green dotted line) we identify a large number of events as spatial rogue waves, among which the one reported in Fig. 4.2(c). The extension of such oceanographic criterion, which is associated to the wave amplitude [199], to our optical system, where we observe the envelope intensity pattern, is here validated by the fact that the threshold approximately coincides with the end of the normal statistics. Taking several recorded extreme events, we then consider the spatial point at which they appear to achieve information on the role of anisotropic field effects in their generation. Counts as a function of the peak transverse x-position are reported in the inset of Fig. 4.3(a); the distribution is qualitatively centered near the beam averaged midpoint (blue reference line) without a shifted prevailing component. This means that in our system the effect of self-bending, associated to diffusive and displacement fields, plays a negligible role in the emergence of rogue waves. This is an intriguing finding since these effects are, in the spatial domain, the counterpart of Raman-shift in optical fiber propagation [87] and rogue temporal events are usually associated to the most red-shifted soliton in supercontinuum generation [96, 20]. Here, the spatial lateral shift (along x) is observed for the whole beam profile and it amount approximately to $20\mu m$ at the crystal output. Results in the weakly nonlinear regime are reported in Fig. 4.3(b). The statistical distribution loses its long tail in this case, showing only a small deviation from the gaussian behavior, evaluated as previously (red line). For comparison with the highly nonlinear case, we fit the detected data with $P(I) = \exp\left(-cI^b - a\right)$ (magenta line). The stretching exponent is now close to one, $b = 0.99 \pm 0.07$, confirming the normal scenario. This fact is quite interesting since it implies that, through the strength of the nonlinear interaction, long-tail statistics can be deterministically generated and controlled. It also associates a fundamental role to the nonlinear response in the appearance of rogue waves.

4.2.2   Numerical and theoretical modelling

To grasp the origin of each single rogue event and how the amount of nonlinearity can affect microscopically its formation, we perform a numerical (2+1)D split-step Fourier method analysis of the generalized nonlinear Schrödinger equation describing the paraxial spatial evolution of the optical field envelope $A(x, y, z)$ in centrosymmetric photorefractive media (section 1.2.3). We consider the two leading terms in the model of Eq. (1.17), that is a nonlinearity containing a Kerr-saturated component and a saturated Raman-like component due to the charge diffusive field. The generalized
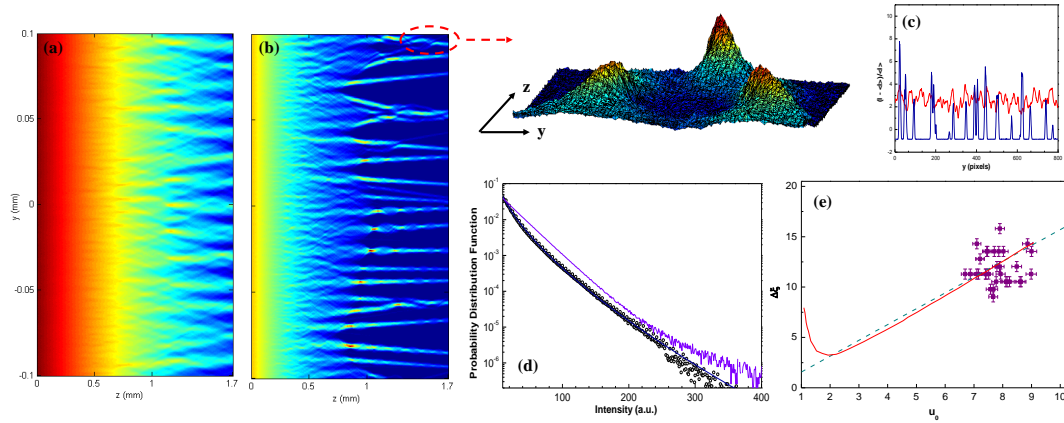
Figure 4.4. Numerical simulations of the beam intensity evolving along the propagation. Typical wave dynamics in the y-z section in (a) nonlinear conditions ($\chi = 5 \times 10^4$) and (b) highly nonlinear conditions ($\chi = 10^5$), where soliton collisions and mergers take place leading to giant peak intensities (detail in the inset). (c) Comparison between output deviations in (a) and (b) along y. (d) Numerical long-tail statistical distribution in the highly nonlinear regime (purple line) compared with the experimental data. (e) Existence conditions for Kerr-saturated photorefractive solitons. Observed extreme events (purple points), linear asymptotic behavior predicted by wave harmonic theory (dashed blue line) and exact (numeric) existence conditions (see section 1.3) (red line). (From [220]).

NLSE in this case reads as

$$
\begin{aligned}
i\partial_z A &= -\frac{1}{2k}\nabla_\perp^2 A + \frac{k}{n}\Delta n(\bar{I})A, \\
\Delta n(\bar{I}) &= \frac{1}{2}n^3 g\varepsilon_0^2\chi^2\left[\frac{E_0^2}{(1+\bar{I})^2} - a\frac{(\nabla\bar{I})^2}{(1+\bar{I})^2}\right].
\end{aligned}
\tag{4.1}
$$

Here $\bar{I}$ is the intensity normalized to the background ($\bar{I} = |A|^2/I_b$), a the diffusive nonlinear parameter, $E_0 = V/l_x$ the bias field and χ the dielectric susceptibility, coupled to the electric field via the electro-optic coefficient g. Following previous studies in the temporal domain [20], the regime of intense filament formation was found from Eq. (4.1) adding a spectrally random seed noise to the input gaussian beam. Scattering during propagation was found numerically to not alter the single rogue wave kinematics and only weakly affect the high-intensity statistical properties of the field, and was rendered negligible. This means that, although in experiments time-dynamics and turbulence associated to the out-of equilibrium state of the medium is a key ingredient to trigger extreme events, in numerics, where such turbulence-mediated disorder is absent, input disorder amplification is sufficient to generate rogue waves. The values of the parameters are selected so as to match those for the KLTN sample and optical setup, except for χ, that is the parameter through which we fix the strength of the nonlinearity. In details, we have $\bar{I} = 30$, $n = 2.4$, $g = 0.16 m^2/C^4$, $E_0 = 2 \times 10^5 V/m$ and a weakly intensity-dependent absorption is used, with average value $\alpha = 2cm^{-1}$; moreover, the susceptibility χ is known

assuming local giant values, of the order of 10^5, during the phase-transition in similar photorefractive ferroelectric crystals [142, 88]. Results are in good agreement with the experimental kinematics of intense light filaments and show how, due to the strong nonlinear response, instabilities grow up during propagation eventually leading to the breaking of the beam waveform. We are able to identify two distinct regimes increasing the nonlinearity: the first condition precedes the onset of modulation instability, while the second is characterized by randomic solitons fusion. In Fig. 4.4 are reported a simulated beam propagation in both cases, respectively with $\chi = 5 \times 10^4$ and $\chi = 10^5$. We find multi-soliton formation in the highly nonlinear conditions (Fig. 4.4(b)); here, collisions and mergers dynamically lead to an intensity distribution with larger spatial fluctuations (Fig. 4.4(c)) and localized structures with giant amplitudes emerge. As shown in Fig. 4.4(d), the output probability distribution function reveals a characteristic long-tailed behavior in good agreement with the experimental statistics and confirms the rogue waves scenario. Moreover, consistently with the experiments, such scenario of nonlinear origin results weakly affected by the Raman-like component in Eq. (4.1). In particular, the simultaneous occurrence of interaction processes and extreme intensity fluctuations in numerics suggest that filament mergers may be the microscopic mechanism at the basis of extreme intensity waves. Recent studies in multi-filamentation [33] and in optical fiber [20, 194] have also pointed out similar conclusion, and this places our results in a general context that may relate rogue waves to soliton collisions in nonlinear Schrödinger model.

To further investigate the role of soliton mergers in rogue waves appearance, we analyzed the experimental extreme intensity spots in terms of soliton physics, casting the normalized-width/amplitude of the filaments in the soliton parameter plane. Considering the reduced (1+1)D model as in section 1.3, solutions of the type $A(x,z) = u(x)e^{i\Gamma z}\sqrt{I_b}$ must satisfy specific existence conditions expressed in terms of the normalized input peak amplitude $u_0 = \sqrt{max\{\bar{I}\}}$ and soliton FWHM $\Delta\xi = \Delta x \left[kn\sqrt{g}\varepsilon_0\right]\chi E_0$ (soliton existence curve). The observed $(u_0, \Delta\xi)$ values for a set of rogue waves are reported in Fig. 4.4(e) and compared to the theoretical soliton existence conditions. The experimental points are analyzed assuming a constant $\chi = 10^5$, coherently with the numerical simulations. Two facts are evident. First, the filaments do in fact fall in proximity of the existence conditions, even though, a single averaged value of effective χ is used. Second, the filaments appear to populate the highly saturated region of the soliton existence curve. The first fact confirms the role played by instabilities in giving rise to general complex spatial structures of solitons [73]. The second, may suggest a role played by scale-invariance. In fact, in highly-saturated conditions ($u_0 \gg 1$), photorefractive solitons are known to manifest self-similarity in the form of a scale-invariance relationship $A(x,z) \rightarrow q^{-1}A(qx, q^2z)$ [82]. Remarkably, scale-invariance is one of the fundamental ingredients thought to play a key role in the emergence of extreme events with heavy-probabilities, as occurs for disordered fields through the integration over multiple spatial scales and in the long-correlated random model [204]. However, data appear as homogeneously distributed around the self-similar trait of the existence plain, implying that the scale-invariance relationship is not well verified for rogue waves. Specifically, the strict relation between width and amplitude that is the distinctive feature of any

nonlinear wave seems to be missing. This fact weakens the understanding based on soliton mergers pointed out by numerical results, since localized waves emerging from the interaction of less intense structures should still satisfy the steady-state soliton conditions. A possible reason for unreliability of the numerical suggestions lies in its time-independent character that is a fundamental aspect in conditions dominated by spatio-temporal fluctuations. The fundamental controversy is resolved in Chapter 6, where the role of scales is specifically investigated through partially-incoherent beams and waveforms of extreme events are resolved with high-resolution.

4.3 Predictability of rogue events

The main point in the study of extreme phenomena is their predictability, especially for those we would like to avoid such as ocean rogue waves [17, 14]. Optical rogue events can be useful for this purpose if common and universal traits exist in their underlying dynamics. Unfortunately, up to now the analogy between hydrodynamic and optical rogue waves does not involve properties residing in their statistical mechanics and remains based only on the anomalous statistics and model equations with just qualitative agreement on the resulting waveforms. In fact, Birkholz et al. [34] have recently shown through nonlinear time series analysis how the dynamical features of various optical extreme events, such as the chaotic nature and the predictability of the process, are generally different. The inspected optical systems are shown to support rogue waves through a time process that appear either completely stochastic or completely deterministic, whereas the ocean dynamics presents small-scale predictable traits and large-scale unpredictability [34]. In particular, stochastic dynamics is associated to systems largely affected by noise such as optical fibers [258], whereas determinism characterizes both conservative [33] and dissipative systems that do not admit a wave-type description [308, 123]. In this section we examine, through nonlinear series analysis and standard methods used for dynamical systems, correlations and predictability of optical rogue wave data that occur in photorefractive beam propagation in comparison with ocean and hydrodynamic extreme events. We found an analogous behavior in terms of correlations and statistical mechanics properties, which consists in an high-dimensional correlation dynamics whose complexity hampers long-range prediction.

4.3.1 Nonlinear series analysis

In our analysis we consider a data series containing a total number of samples $N \simeq 2.5 \times 10^4$, part of which is shown in Fig. 4.5(a). This series represents detected intensities as a function of the free spatial coordinate (here renamed as x) and exhibits a marked long-tail statistics (Fig. 4.5(d)). In Fig. 4.5(b) we report a sub-segment of the experimental spatial series obtained as described in section 4.2.1 and sampled along the white-dotted line, which includes a rogue wave with its extreme intensity spot. The averaged autocorrelation function obtained considering the whole series of N points is shown in Fig. 4.5(c). The autocorrelation length of the series represents the typical spatial scale of the disordered intensity distribution and is $\ell \simeq 9.5 \mu m$, more than one order of magnitude greater than the experimental resolution. The presence of chaotic and predictable features in the series is explored
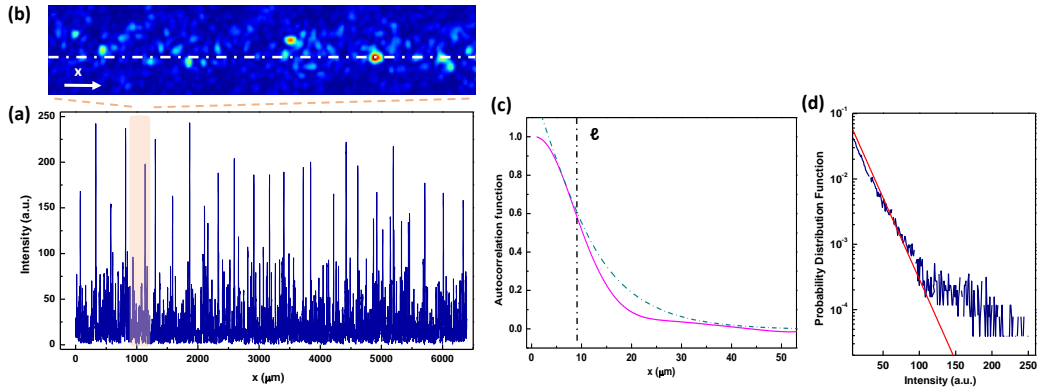
Figure 4.5. Spatial series of intensities detected in a photorefractive ferroelectric with rogue events. (a) Data series with the shaded region underlining the observation shown in (b) and containing a rogue event as an anomalously-bright localized spot. (c) Spatial autocorrelation functions of the full N-points data series; dotted line is a decay fit giving the correlation length ($1/e$ width) ℓ. (d) Long-tail statistics of the series (blue line) compared with a normal probability distribution with the same spatial-averaged intensity (red line). (From [221]).

in analogy with previous studies [34] using the Grassberger-Procaccia embedding method [124, 1, 54]; specifically, from the N-point series $\mathbf{x} = \{x_1, x_2, ..., x_N\}$ we consider all the subseries $\mathbf{x}_{im} = \{x_i, x_{i+1}, ..., x_{i+m}\}$ of dimension m (embedding dimension). The statistical distance

$$r_{ijm} = \sqrt{\sum_{k=i}^{i+m} |x_k - x_{k+j-i}|^2},\tag{4.2}$$

that quantifies the difference between values assumed in two generic subseries, is evaluated for all i and $j > i$ to compute the correlation histogram $c_m(r)$ as:

$$c_m(r) = \frac{2|r_{ijm} : (r + \delta r) < r_{ijm} \le r|}{(N - m)(N - m - 1)}.\tag{4.3}$$

The behavior of $c_m(r)$ at small r reflects the possible appearance of specific subseries with high (non-random) frequency, i.e., it is sensitive to possible "deja-vu" phenomena when the series are sampled with a given scale m. To extract the predictable or stochastic features in our series, we improve the embedding analysis with the method of surrogates, which allows the comparison of the detected dynamics with the corresponding dynamics that would emerge from a pure random process. Starting from physical random data [130], we compile surrogate data sets identical to the original series as regards for the linear statistical properties. These surrogates have the same probability distribution function (long-tail statistics), autocorrelation functions and Fourier spectrum of our original series, and appear as reordered copies of the observed spatial sequence $\mathbf{x}$ [268, 243, 244]. Evaluating $c_m(r)$ with surrogate data sets and comparing it with results for the original series we expect small differences if our data comes from a stochastic process. In contrast, as shown
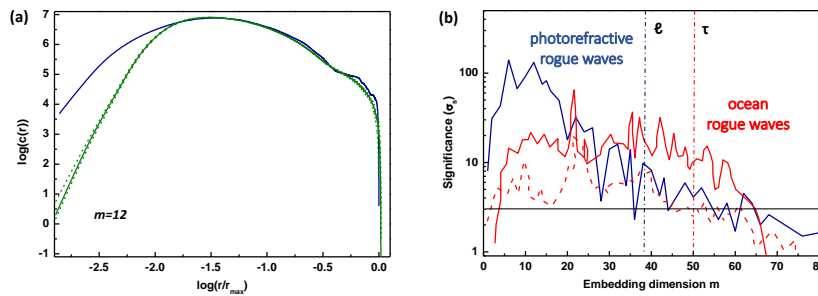
Figure 4.6. Predictability of rogue waves. (a) $c_m(r)$ at $m = 12$ for photorefractive extreme events, showing a large deviation of the rogue waves data (blue line) from the average of surrogates (green line), whose spread is indicated by the standard deviation over fifty independent realizations of surrogates (green-dotted lines). (b) Significance of deviations from surrogates as a function of m for optical data (blue line) and for the temporal dynamics of Draupner ocean data (red and red-dotted lines stays respectively for Draupner2 and Draupner1 data, as in Ref. [34]). The horizontal black line indicates the minimum confidences of $3\sigma_s$ separating predictable and unpredictable dynamics; ℓ and τ are respectively the autocorrelation length and time for the optical and ocean series. (From [221]).

in Fig. 4.6(a) for $m = 12$, large deviations are observed at low r, with the rogue series that leads to enhanced recurrence frequencies compared to the average ones in the surrogates. The observed intensities with extreme events are more correlated than a random process, meaning that the optical field in a point of space is directly related to that existing at least at distances smaller than m. We quantify this kind of predictability giving the significance of the discrepancy between $c_m(r)$ for original and surrogate data; this is reported in Fig. 4.6(b) (blue line) in units of surrogate standard deviations σ_s and has been evaluated as an average difference at low r. Deterministic traits characterizes the series on small and intermediate scales m, then they disappear as the autocorrelation length ℓ is reached, in proximity of $m = 42$ (corresponding to $10\mu m$). In other words, on larger scales the spatial dynamics of photorefractive rogue waves lose traces of determinism and appear indistinguishable from a re-ordered random series in which the same values of intensity appears. This scale-dependent behavior is at odds with other reported optical data in the temporal domain [34], but, as shown in Fig. 4.6(b), it remarkably mimics the features of the temporal dynamics of Draupner data sets [134, 135], the prototype of ocean rogue waves. As observed in our spatial series, these ocean data have a behavior that for long time-scales turns indistinguishable from their surrogates. This feature may be due to an intrinsic property, that is, data are actually stochastic on these scales and correlations rules only locally the spatial dynamics. On the other hand, it may be a "practical" unpredictability related to the use of the embedding method for such dynamics.

4.3.2 Analogues correlations in optical and hydrodynamic data

To further understand this statistical behavior and to eventually set it as universal property of rogue states we carry forward the Grassberger-Procaccia analysis and

we extend it to hydrodynamic series with a large number ($N \simeq 5 \times 10^4$) of samples. These data are measurements of the water wave height and are carried out in a wave tank for different environmental and nonlinear conditions [201]. Part of the time series of the wave envelope are shown in Fig. 4.7 with their autocorrelation function and long-tail statistics. They are labeled as $g1$-$g6$ and rogue waves populate especially the $g6$ series. For both optical and hydrodynamic data, dynamical analysis is performed evaluating the correlation integral

$$C_m(r) = \frac{1}{N^2} \sum_{j>i} \Theta(r - r_{ijm}), \tag{4.4}$$

where $\Theta(r)$ is the Heaviside step function. The correlation integral for small distances r is predicted to increase monotonically according to $C_m(r) \propto r^\nu$, with an exponent ν that, for large embedding dimensions m, characterizes the fractal correlation dimension of the attractor $D(2)$ describing the possible chaotic dynamics [124, 54]. As reported in Fig. 4.8(a-d), both optical and hydrodynamic data in log-scale show a linear behavior of $C_m(r)$ at low r with a slope that increases with the embedding dimensions m. The extracted exponents ν as a function of m are reported in Fig. 4.8(b-e). The behavior is characterized by a well-defined linear growth at low m, as typically occurs in dynamical processes both of chaotic and stochastic origin [54], since, basically, similarities in subseries are much less likely increasing the subseries size. In general, chaos is highlighted by a saturation of ν at large m and the approached value corresponds to the fractal correlation dimension of the attractor $D(2)$. We observe that starting from $m = 20$ and $m = 16$, respectively for the optical and hydrodynamic case, the linear behavior is damped and seems to saturate to a constant value in proximity of $\nu \approx 6$ and $\nu \approx 4$ ($g1$), $\nu \approx 5$ ($g6$). However, a careful analysis is needed in deducing the correlation dimensions. Noise in experimental data, emerging from the physical realization of the process and from its detection, affects especially the estimate of ν for long subseries, that consequently present a larger uncertainty. More importantly, a crucial role is played by the amount of available data N [257, 236]. Because the number of completely independent subseries $\mathbf{x}_{im}$ used in the embedding method scales as N/m, the information that can be extracted is limited when considering long scales. For a series of N points, numerical criteria set the maximum observable value of ν approximately at $2logN$ [236] (horizontal line in Fig. 4.8(b)), implying that only values sufficiently below this threshold are reliable. Dimensions higher than $4 - 5$ are generally considered too high for describing deterministically the dynamics [54]. In fact, to resolve the long-range dynamics up to m, the Grassberger-Procaccia method needs an amount of data N that grows exponentially with m [257]. Therefore, the reported saturation of ν does not demonstrate the presence of a low-dimensional attractor but it implies a high-dimensional attractor that underlies the complexity of the dynamics ruling both optics and hydrodynamics data [36]. We note that the dynamics seems much more complex (larger saturation ν value) as more relevant is the presence of extreme events. We also analyze the scale dependence of the dynamics using the generalized entropies

$$h_m(r) = ln\left[C_m(r)/C_{m+1}(r)\right], \tag{4.5}$$
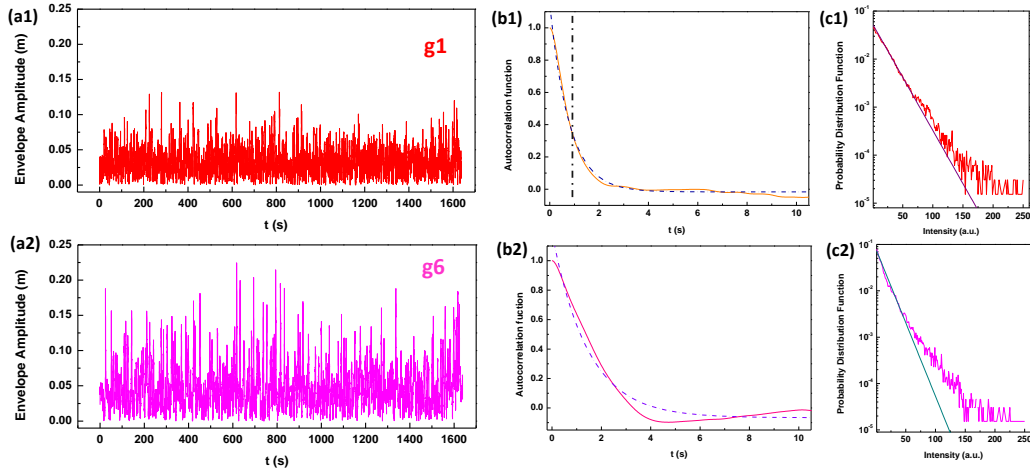
Figure 4.7. Time series from hydrodynamic experiments in wave tank [201]. (a) Measured time dependence of the wave envelope, (b) its intensity autocorrelation function and (c) probability distribution function for the (1) $g1$ and (2) $g6$ setting. Rogue waves appearance in particularly enhanced in the $g6$ experiment. Lines in (b) and (c) are decay fits and exponential functions, respectively.
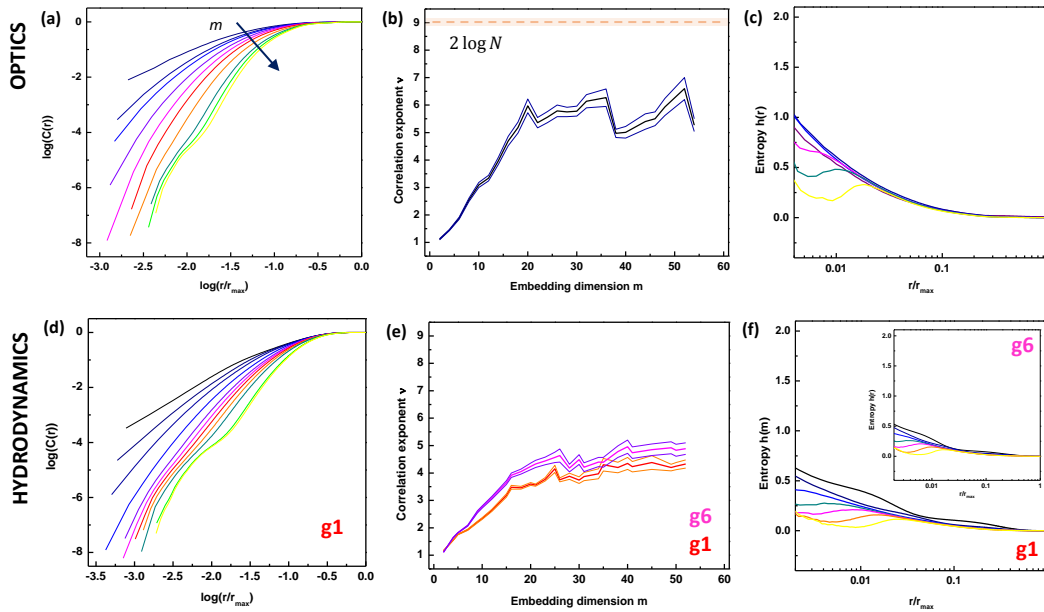
Figure 4.8. Chaotic dynamics of optical and hydrodynamic rogue wave data. (a-d) Correlation integrals $C_m(r)$ and (b-e) Grassberger-Procaccia exponents ν as a function of the embedding dimension m. (c-f) Generalized entropies $h_m(r)$ at different m, underlining finite-size effects at large m. The red-shaded line in (b) indicates the maximum observable value of ν following Ref. [236] for the total length N of the optical series.
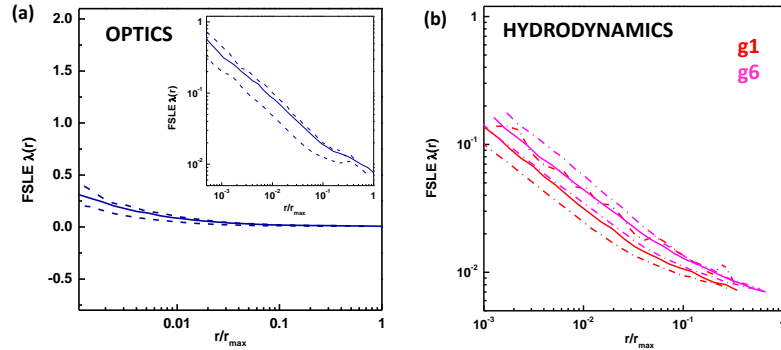
Figure 4.9. Finite-size Liapunov exponents in different rogue regimes. (b) $\lambda(r)$ computed for subseries with $m = 40$ for (a) optical and (b) hydrodynamic data series $g1$ and $g6$. Continuous lines are values averaged over several thousands of realizations, dashed lines indicates their standard deviations. Inset in (a): detail of the low-r region.

that measure the information produced by the dynamical system and in which a plateau to a constant value indicates the chaotic origin of the signal [55]. As shown in Fig. 4.8(c-e), increasing m leads to entropies $h_m(r)$ approaching a flat behavior al low r (deterministic signal). However, considering for instance the optical case, for $m \gtrsim 42$, $h_m(r)$ exhibits a noisy and non-monotonic behavior, consistent with the absence of predictable traits on these scales. Very interesting is that even the hydrodynamic series give analogous results. Therefore, the large-scale unpredictability for rogue waves has roots in the extremely complex behavior of the dynamical process occurring in optical spatial propagation as in water waves evolution. Another interesting point is that we are here comparing different dynamics in space and time; results are consistent with the fact that complex chaotic dynamics in spatially-extended systems generally affect all the degrees of freedom. We expect that further understanding can be obtained considering simultaneously more than one dynamical variable. Practical unpredictability holds for the entire state of the system and it not a property of the single extreme event. This "complexity" [36], that masks properties of the effective underlying dynamics, may be the reason of the common statistical mechanics behavior observed in very different optical states and sea conditions. Moreover, it can also occurs in conditions leading to only small deviations from gaussian statistics, as pointed out in the $g1$ hydrodynamic series and in Ref. [31] for sea states.

Since the generalized entropy $h_m(r)$ is the dynamical counterpart of the Lyapunov exponents characterizing the rate of error growth between initially close trajectories, we conclude our study with the Lyapunov analysis. In fact, provided an high-dimensional and in principle predictable chaotic behavior of rogue wave states, their actual predictability is limited to a distance related to the first Lyapunov exponent. The finite-size Lyapunov exponent (FSLE) $\lambda(r)$ quantifies its value for experimental signals, where finite resolution and non-infinitesimal perturbations are crucial. Using the metric distance of Eq. (4.2) we compute $\lambda(r)$ with the error-doubling method, detailed in Ref. [55, 22], as an averaged quantity over several thousands of subseries that start from the same detected intensity value. Results for $m = 40$ are reported

in Fig. 4.9 and show an almost constant $\lambda(r)$; the analogy between light and water waves is straightforward also in this case. Considering the optical data, the averaged value at the smallest r is $\lambda = 0.58$. Moreover, the expected $h(r) \approx \lambda(r)$ [55] is verified by our results. The value λ we have found implies that, given an initial uncertainty δ, it is possible to predict the wave intensity with a tolerance Δ only up to an averaged predictability distance $x_p = \frac{1}{\lambda} ln(\frac{\Delta}{\delta})$ [22]. In our case, for example considering the experimental resolution $\delta = 0.5$ and $\Delta = 10$, we have $x_p \approx 5 \approx 2.5 \mu m$, that is much less than the distance over which the series appears as predictable following Fig. 4.6(b). Therefore, the complexity of the dynamics make useful extreme event prediction based on standard methods just as difficult in the optical case as in ocean and hydrodynamic rogue waves. However, the existence of intrinsic correlation in the process, that make it different from a stochastic evolution, is crucial because it justifies efforts aimed at developing a probabilistic approach to prediction [131, 132]. From this point of view, our results represent the statistical mechanics completion of the analogy between ocean, hydrodynamic and optical extreme events previously based qualitatively on the probability distribution function and on the NLSE description.

Chapter 5

Transitions to turbulence in optical wave propagation

In this Chapter we investigate the optical state underlying the formation of spatial rogue waves in photorefractive ferroelectrics. Exploiting the cumulative property of the nonlinearity, we report experiments proving evidence that such state is triggered by a fully-developed transtion to optical turbulence. The result represents the first observation of turbulent transitions for propagating optical waves [222]. In particular, the onset of turbulence occurs as the disordered hosting material passes from being linear to one with extreme nonlinearity, so that increased wave interaction causes a modulational unstable quasi-homogeneous flow to be superseded by a chaotic and spatially incoherent one with emergence of concomitant rogue waves. To introduce the topic, we note as turbulence is a universal phenomenon in which a system is characterized by many out-of-equilibrium degrees of freedom [159]. Turbulent transitions attract great interest because the onset of spatiotemporal disorder profoundly changes the physical features of a system, the paradigm being the transport and drag properties of a fluid in a pipe and channel flow [125, 23, 241]. Manifestations of turbulence can also occur in waves, these including acoustic [115], spin [45] and optical waves [215]. In fact, when nonlinear interaction involves the excitation of a large number of waves, phase and amplitude fluctuations may lead to a stochastic field described statistically using wave turbulence theory [195]. Wave turbulence usually refers to weakly nonlinear wave systems in which the linear evolution scale can be separated from the nonlinear one. Generally these systems are dominantly influenced by some external noise and have negligible intrinsic (internal) disorder. On the other hand, as linear and nonlinear scales are comparable, strongly nonlinear coherent structures may also emerge and interplay with the incoherent wave field (strong wave turbulence). In optics the onset of strong turbulence greatly alters coherence and statistics of light, as observed for pulse trains in a ring resonator [190], semiconductor lasers with feedback [192], and, recently, in tailored Raman fiber lasers [280, 279, 18, 289]. However, experimental studies of wave turbulent behavior in the spatial domain, where light is not trapped and actually propagates in space, are especially challenging [254, 253, 42, 160, 266]. In particular, direct evidence of a fully-developed turbulent transition for propagating waves has remained elusive. As anticipated, here we report its observation for nonlinear beam propagation in

photorefractive ferroelectric crystals. We stress that the detected transition involves the coupling of two stochastic effects: external noise associated to the initial condition and internal fluctuations of the nonlinear response.

5.1   Exploiting the cumulative nonlinearity

To reveal transitions to turbulence in the spatial domain we make use of experimental setup e methods extending the ones discussed in section 4.2.1. Specifically, a line (1D) gaussian beam ($\lambda = 532nm$) of waist $\omega_0 = 7\mu m$ along the x-direction and quasi-homogeneous along the y-direction (Fig. 5.1(a)) is launched in a photorefractive ferroelectric crystal of KLTN, $K_{1-\alpha}Li_\alpha Ta_{1-\beta}Nb_\beta O_3$, with $\alpha = 0.04$ and $\beta = 0.38$. The sample is a zero-cut optical quality specimen with size $2.4^{(x)}$x$2.0^{(y)}$x$1.7^{(z)}mm$ (l_x x l_y x l_z) and with the structural transition occurring at the Curie temperature $T_C = 294K$. Since large dielectric fluctuations generally persist also above this point, in the present case nonlinear light dynamics is studied systematically with high accuracy at $T = T_C + 2K$. The input wave copropagates along the z-axis of the crystal with an uniform background intensity and nonlinearity sets in when an external bias field is applied parallel to the polarization of the propagating wave (maximum electro-optic coupling). The spatial intensity distribution is measured at the input and then at the output of the crystal along the initially quasi-homogeneous y-direction in different nonlinear conditions by means of an high-resolution imaging system composed by an objective lens ($NA = 0.5$) and a CCD camera at $15Hz$. As a physical parameter to study the transition to turbulence we consider the physical time ruling light dynamics at the crystal output. In fact, in Chapter 1 we have discussed how the photorefractive nonlinearity has the peculiar property of being noninstantaneous and accumulates in time, since it involves a build-up of a photogenerated space-charge field. In this way, observations at different times correspond to beam propagation for increasing nonlinearity up to saturation [174]. A typical time scale τ for beam dynamics is fixed through its symmetry breaking
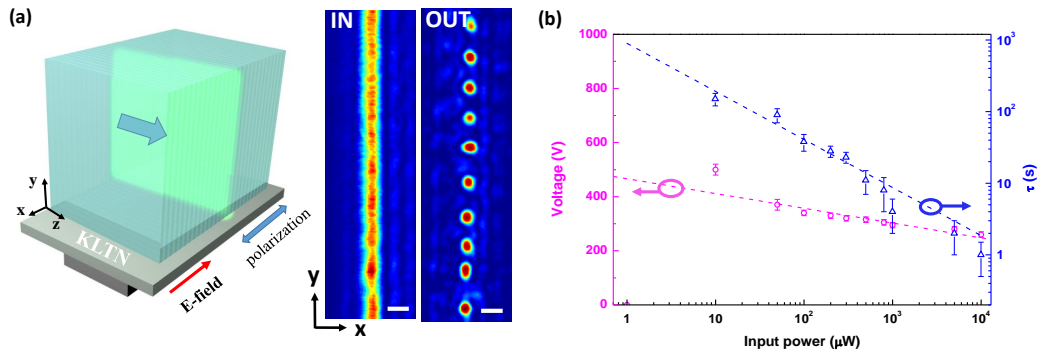
Figure 5.1. Beam symmetry-breaking in unstable photorefractive ferroelectric crystals. (a) Sketch of the setup geometry adopted. Scale bars for input and output intensity distributions correspond to $20\mu m$. (b) Characterization of transverse breaking: intensity dependence of the process, with the minimum required voltage and the average time scale τ providing the formation of periodic structures. Lines are linear fits. (From [222]).
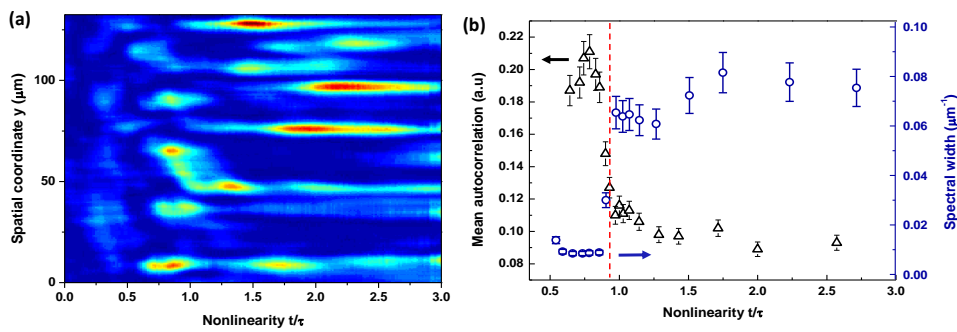
Figure 5.2. Observation of the turbulent transition in one-dimensional beam dynamics. (a) Detected output spatial intensity distributions as a function of the nonlinearity expressed through the continuous dimensionless control parameter t/τ. (b) Corresponding width of the spatial Fourier spectrum and mean intensity autocorrelation (see main text) increasing the nonlinearity. Red line serves as guide at the sharp transition signaling the onset of optical turbulence. (From [222]).

into periodic coherent structures (Fig. 5.1(a)), a process that inhibits stable spatial (1+1)D soliton formation also for different type of nonlinearity [149, 178, 113, 91, 110]. In fact, this stage can be accurately identified experimentally and we first characterize it varying the accessible experimental parameters. In particular, changing the input power, we measure the threshold voltage to observe transverse break-up and filaments formation. Results are reported in Fig. 5.1(b) and show how, increasing the input power, an almost linear scaling is found. Moreover, fixing the bias field to V=500V and varying the input power, we measure the averaged time τ, that is the effective nonlinearity at which the periodic break-up is observed. τ is found to decrease also linearly with the input power, in agreement with the fact that the photorefractive nonlinearity build up rate is inversely related to the peak intensity. The dimensionless continuous control parameter of the nonlinearity is thus t/τ, where t is the evolving time. Hereafter we consider a laser power $P = 0.5\mu W$, with $\tau \approx 8$ s (Fig. 5.1(b)). We estimate local variations of the refractive index up to 10^{-3} at $t/\tau \simeq 1$ and up to 10^{-2} for $t/\tau \simeq 2$.

5.2 Evidence of turbulent transitions in beam dynamics

Direct evidence of the onset of turbulence as the nonlinearity increases is reported in Fig. 5.2. Once that the quasi-homogeneous input line beam has experienced symmetry-breaking via modulational instability, a sharp transition into a chaotic state with pseudo-recurrent patterns occurs for $t/\tau \gtrsim 1$ (Fig. 5.2(a)). Some of these filaments can have an extremely large intensity, as we discuss hereafter. This transition corresponds to the loss of spatial coherence that persists only on small scales. Measuring the width of the spatial Fourier spectrum, we found a sharp increase of almost one order of magnitude (Fig. 5.2(b)). Correspondingly, the long-range autocorrelation of the intensity light distribution $I(y)$ abruptly decreases, as shown in Fig. 5.2(b), where we have averaged over large r distances the absolute value of the quantity (autocorrelation function) $g(r) = \langle [I(y)-\langle I\rangle] \times [(I(y+r)-\langle I\rangle] \rangle$ normalized to $g(0)$. We stress that detecting the onset of turbulence as a sharp
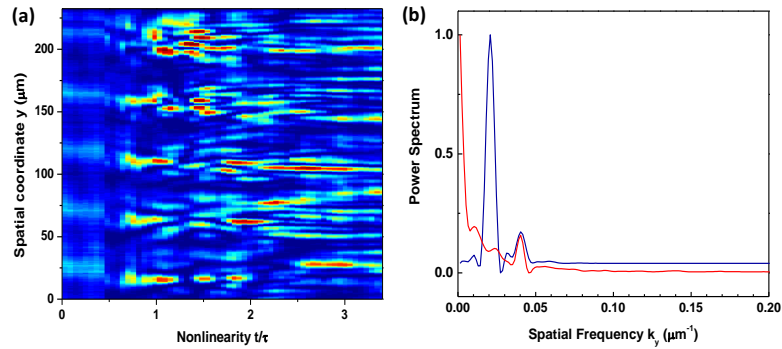
Figure 5.3. Onset of optical turbulence for spatially-modulated input waves. (a) Output intensity distribution increasing the nonlinearity t/τ. (b) Input power spectrum for spatially-modulated beams (blue line) in comparison with the quasi-homogeneous case of Fig. 5.2 (red line). (From [222]).

transition signaling departure from coherence is a method that goes beyond the stability properties of the input flux. In fact, an analogous transition has been reported in conditions where the homogeneous state of the dynamics is stable [280] and unstable [289] with respect to perturbations. We note that a behavior similar to Fig. 5.2 has been numerically observed studying the nonlinear stage of modulation instability in the framework of the nonlinear Schrodinger Equation [5]. Here, the incoherent state generated during wave evolution is referred as integrable turbulence [5]. However, our results depart from this scenario since the presence of a saturable nonlinearity makes wave dynamics non-integrable. This means that the observed turbulent transition weakly depends on the input wave and can occurs also without the modulational instability process. We demonstrate this repeating the experiments with an inhomogeneous coherent input wave; using a spatial light modulator (SLM) the input field is modulated along the y-direction with a periodic component. As shown in Fig. 5.3(a) a transition to turbulence is observed at $t/\tau \approx 1$. In this case, beam breaking is dominated by the input spatial frequency $k_y = 0.02 \mu m^{-1}$ and modulation instability is only weakly involved, as noise experiences small amplification on this scale. In Fig. 5.3(b) the input power spectrum is shown in comparison with the quasi-homogeneous case. The picture can be easily extended to generically modulated input waves.

5.3 From instabilities to optical turbulence

In order to study statistical and stochastic properties of the optical state before and after the transition to turbulence, we consider the quasi-homogeneous input case and we collect data for approximately two hundred uncorrelated experiments in the same conditions used in Fig. 5.2. Each realization naturally presents a different noise configuration, which is caused by fluctuations of the input wave arising from the experimental setup (Fig. 5.3(b)) and by local variations of the electro-optic response. These two stochastic effects are coupled, since local intensity fluctuations are amplified by the giant response of the material and inhomogeneity in the nonlinearity strongly affects light dynamics. We underline that fast material fluctuations are crucial in
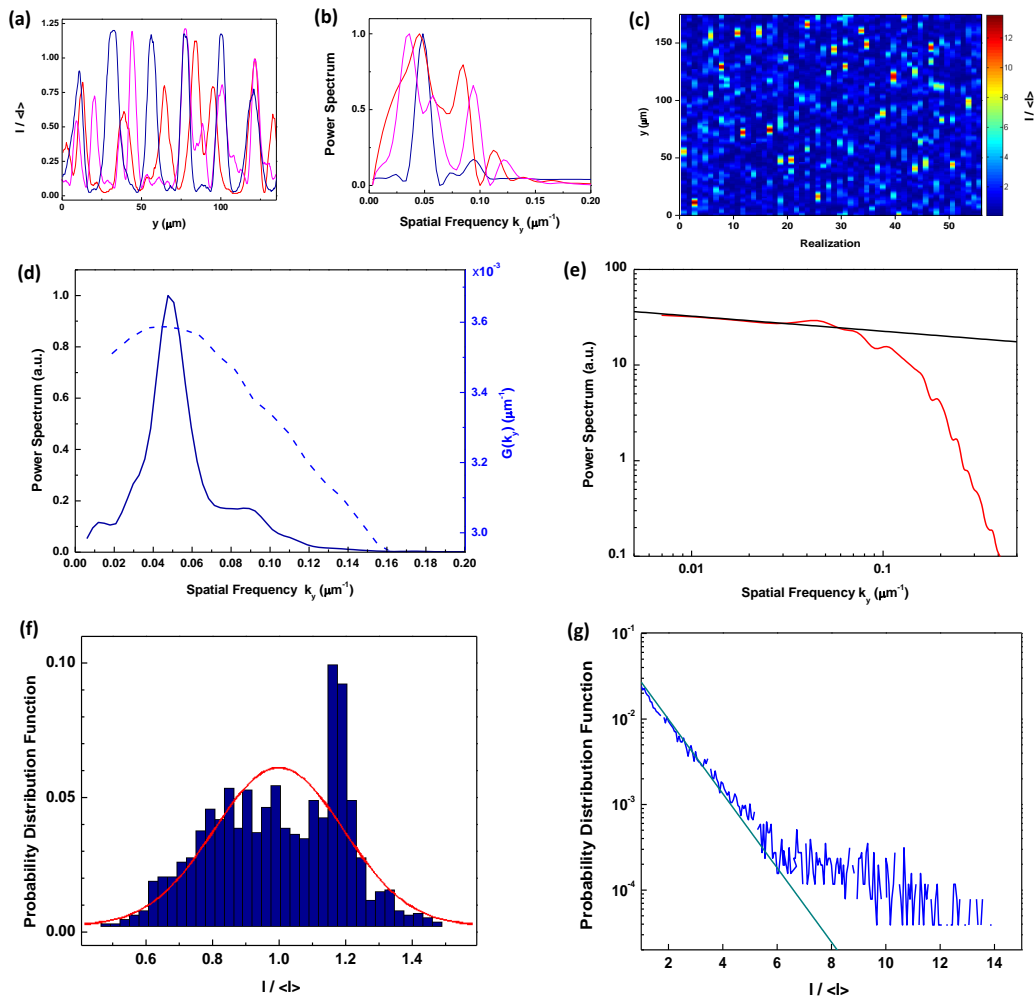
Figure 5.4. Spectral and statistical properties of the optical state before and after the turbulent transition. (a-b) Intensity and spectral sample distributions of single-shot measurements at moderate nonlinearity ($t/\tau \approx 1$) showing the excitation of the spatial frequency $\bar{k}_y = 0.05\mu m^{-1}$ (blue line), spectrally-broad noise amplification (red line) and simultaneous development of well-defined low and high frequency modes (magenta line). (c) Single-shot disordered intensity distributions detected in the turbulent regime at $t/\tau \simeq 2.5$. (d) Ensemble spectrum of modulational instability before the transition ($t/\tau \approx 1$) with the instability gain function (blue-dashed line). (e) Measured wave-turbulent power spectrum (red line) fitted on large spatial scales with the scaling behavior $\propto k_y^{-\gamma}$, $\gamma = 0.15 \pm 0.01$ (black line). (f) Peak-intensity PDF of localized structures emerging from instability at $t/\tau \approx 1$, experimental counts (blue bars) and gaussian trend of the distribution tails (red line). (g) Measured long-tail statistics in optical turbulence at $t/\tau \approx 2.5$ (blue line) and consistent gaussian exponential scaling showing spatial rogue wave generation in the turbulent regime. (From [222]).

observing the onset of turbulence; the transition is found to disappear as the crystal is heated to a few degrees above the operational temperature, further confirming results of Chapter 4, in which a thermal gradient is used to select different nonlinear and stochastic regimes of propagation. Moreover, since disorder in the material is

not fixed on the time-scale of the experiment and it is furthermore modified by the wave, Anderson localization effects cannot occur in our case [249, 164].

5.3.1   Spectral and statistical properties

An ensemble spectral analysis at moderate nonlinearity preceding the transition reveals the modulational unstable regime. The well-defined peak in Fig. 5.4(d) shows that the typical spatial frequency experiencing maximum gain is $\bar{k}_y = 0.05 \mu m^{-1}$. Since in centrosymmetric photorefractive media the transverse instability problem can not be resolved easily with linear stability methods [179], we compare this result directly with numerical simulations. We perform a numerical (2+1)D split-step Fourier method analysis of the generalized nonlinear Schrödinger model describing the paraxial spatial evolution of the normalized optical field envelope in centrosymmetric ferroelectrics. Following the treatment in Chapter 1, with $\psi(x, y, z) \equiv A(x, y, z)/\sqrt{I_b}$, the model is rewritten as

$$i\partial_z \psi = -\frac{1}{2k}\nabla_\perp^2 \psi + \frac{k\Delta n_0}{n}\left[\frac{1}{(1+|\psi|^2)^2} - 2\alpha(\frac{\nabla_\perp|\psi|^2}{1+|\psi|^2})^2\right]\psi, \qquad (5.1)$$

where the parameters notation is the one already used. The value of the diffusive nonlinear parameter $\alpha < 1$ set the weakly-nonlocal regime of the model. We solve Eq. (5.1) adding a spectrally-random seed noise to the input gaussian beam, whereas values of the parameters are selected so as to match those for the KLTN sample and optical setup. Following previous studies [48], the modulation instability gain function $G(k_y)$ is computed evaluating the amplitude of the Fourier spectrum $\hat{\Psi}(k_y, z)$ at the input, $z = 0$, and output, $z = l_z$, as $G(k_y) = 1/l_z \ln\left[\hat{\Psi}(k_y, 0)/\hat{\Psi}(k_y, l_z)\right]$. The numerical spectral gain is shown in Fig. 5.4(b) as an average over several independent realizations; its maximum well agrees with experimental results. However, the broadening of $G(k_y)$ around the maximum amplified spatial frequency indicates that, during the single-shot dynamics, higher/lower frequencies can also emerge easily and compete with the characteristic one. In fact, modulational instabilities are generally known to possess a strong dependence on the specific noise-realization, with properties varying from shot-to-shot [260]. In Fig. 5.4(a-b) we show single-shot measurements, each as an example characterizing a particular type of fluctuation. We note that as the frequency $\bar{k}_y$ is mainly excited, localized structures have a weakly-varying peak intensity and there is equipartition of power across the generated mode (see also inset in Fig. 5.1(a)). On the other hand, broad and double-frequency amplification results into a coherent pattern presenting large intensity fluctuations. Completely different is the scenario in the turbulent regime. Intensity distributions vary stochastically from shot-to-shot, as shown in Fig. 5.4(c) for several independent realizations acquired at $t/\tau \simeq 2.5$, where we expect the nonlinearity to be fully saturated. Waves are characterized by random phases in analogy with optical realizations of wave turbulence theory [42], although from the statistics discussed hereafter we realize that some correlations between modes actually exist. In Fig. 5.4(e) we report the ensemble power spectrum; it is extremely broad and without specific resonances, with the peak associated to the amplification of $\bar{k}_y$ before the transition that results fully relaxed towards lower spatial frequencies. The spectrum

results well-fitted at low frequencies by a power law behavior $\propto k_y^{-\gamma}$, with the scaling exponent $\gamma = 0.15 \pm 0.01$. Therefore, we observe evidence of an inverse cascade as the nonlinearity increases, since the majority of the wave action is now located at low transverse wavenumbers. However, this flux of wave action towards large scales should be distinguished from the one occurring in wave-turbulence theory. In weak turbulence, an inverse cascade occurs for random waves at weak nonlinearity under forcing at intermediate scales [42, 160]; here, it occurs in highly nonlinear conditions and after the modulational instability stage.

In the disordered regime, part of which is shown in Fig. 5.4(c), we also note the appearance of several bright localized spots. Statistical analysis shows that they are rogue waves. We first consider the probability distribution function (PDF) of peak-intensity values of localized structures emerging from instabilities before the turbulent transition. We analyze more than 10^3 events, so as to populate the histogram reported in Fig. 5.4(f). This PDF contains a high-intensity peak embedded into a broad distribution. The peak, at $I/<I> \simeq 1.2$, is deterministic and closely related to the peak in the gain spectrum of Fig. 5.4(d), as it arises from structures belonging to the maximally amplified frequency $\bar{k}_y$. Random fluctuations in this stage populate the rest of the distribution, with tails compatible with a gaussian decay, implying that extreme events occur here with low probability. This allows us to conclude that in our system giant perturbations not arise in coherent structures generated by stochastic fluctuations in instability. On the contrary, as reported in Fig. 5.4(g), the PDF measured deep into the turbulent regime at $t/\tau \simeq 2.5$ presents the long-tail anomalous behavior defining rogue wave phenomena, as reported in Chapter 4. In fact, for large intensities it deviates from the gaussian distribution expected for incoherent fields. We note that in the present case the setup is able to detect with high-resolution the formation dynamics of each rogue wave. We found that extreme events suddenly disappear as t/τ further varies, so that no traces are found after their passing. Moreover, from our data, inelastic interactions between less intense structures in the wake of extreme events are not so evident. This fact may involve the presence of a different saturation-dependent microscopic process in rogue wave appearance, as discussed in Chapter 6. Further developments include the study of two-dimensional space phenomena, as well as the building of a nonlinear wave model that, taking into account fluctuations in the nonlinear response of the medium, can properly describe the observed turbulent regime. The possibility of varying the modulation of the input field opens new perspective for the study of optical turbulent regimes.

5.3.2 Shot-to-shot fluctuations and correlations

We also investigate shot-to-shot fluctuations and correlations of the optical state before and after turbulent transitions. This allows us to understand the presence of correlations between the spectral properties of different realizations of the stochastic dynamics, i.e. modes interaction. This fact is particularly important in the turbulent regime where rogue waves may be related to phase-locking of different spontaneous modes. We make use of an analogous KLTN crystal but with an embedded slab waveguides [127, 141], which allows us to repeat the experiments in a strictly 1D geometry, further increasing capacity and reliability of our analysis. In analogy
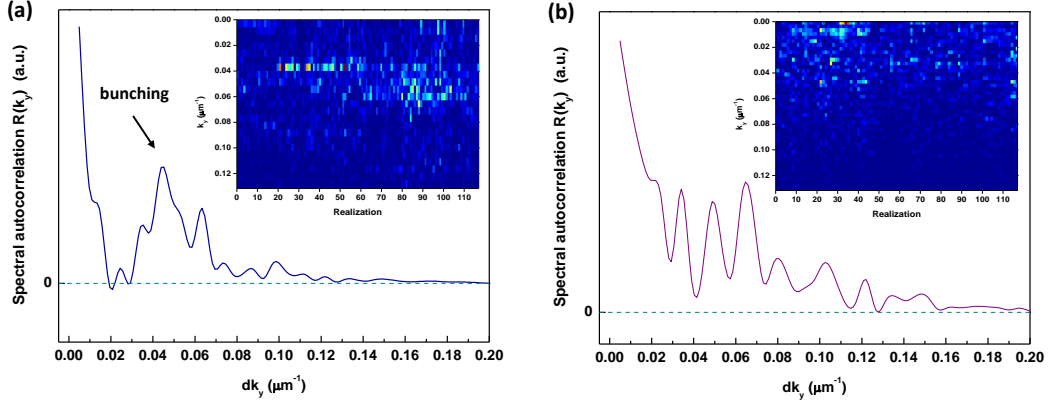
Figure 5.5. Shot-to-shot spectral correlations in turbulent dynamics. (a) Background-free spectral autocorrelation function in the modulational unstable regime showing bunching between different spatial frequencies experiencing amplification. (b) $R(k_y)$ for optical turbulence, where no typical interaction between modes is found. Insets are the spectral maps considered in the analysis.

with a recent study on modulation instability in the temporal domain, where anti-bunching and preferred spacing between adjacent frequency modes emerging from noise amplification is found [260], we first compute the background-free spectral autocorrelation function $R(k_y)$. It is sensitive to those correlations that are present in the individual spectra and removes the background from the overall spectral shape. We obtain it forming the average of the spectral autocorrelations $\langle S_i(k_y)\cdot S_i(k_y+dk_y)\rangle$ of all single-shot experimental spectra S_i and subtracting the autocorrelation of the averaged spectrum $\langle S_i(k_y)\rangle \cdot \langle S_i(k_y + dk_y)\rangle$. Simply put, we compute the average autocorrelation minus the autocorrelation of the average. Results are reported in Fig. 5.5(a) for the modulational unstable regime at $t/\tau \approx 1$ and in Fig. 5.5(b) for the turbulent regime after the transition ($t/\tau \simeq 2.5$). The correlation function display a positive central peak at zero spatial frequency shift arising from the fact that all individual spectra consist of narrow lines that are absent in the average spectrum, whereas the features at larger frequency shift originate from the interaction between different modes. If the separate excitations were uncorrelated, the analysis would yield only a central peak on a flat background because each feature would only be correlate with itself. In turn, negative values signify the fact that such peak spacings are underrepresented in the individual events (anti-correlation). In the modulation unstable regime, contrarily to the optical fiber case [260], we observe bunching between modes. Although correlation between adjacent frequency results strongly suppressed, with $R(k_y)$ reaching negative values, the main feature in the correlation behavior reported in Fig. 5.5(a) is a second peak at $dk_y \simeq 0.045 \mu m^{-1}$ indicating bunching in the gain process. The origin of this interaction may be related to spatial beating. Specifically, when two high-frequency modes develop and compete for their amplification, they generate beating on the quasi-homogeneous beam giving a modes lying in the maximum gain region. Therefore, at the output only a low-frequency and an high-frequency line is found. The typical features of modulation instability are lost during the turbulent transition; $R(k_y)$ in the turbulent regime presents the central peak and only fast and disordered oscillations. This means that in such case

significant bunching and anti-bunching does not take place for any spectral shift. However, these oscillations may be the signature of the chaotic interaction between the large number of modes emerging in turbulence.

The absence of mode-locking in the turbulent regime with rogue waves can be further investigated considering the overlap between shot-to-shot spectral correlations. This specific analysis has been recently used to demonstrate experimentally replica symmetry breaking in random lasers [118, 120]. Each realization of the dynamics represents a replica whose fluctuations of the power spectrum at a given spatial frequency reads as $\Delta_i(k_y) = S_i(k_y) - \langle S_i(k_y) \rangle$, with $\langle S_i(k_y) \rangle$ the average over replicas of each mode power spectrum. The overlap between shot-to-shot spectral fluctuations is defined as

$$q_{ij} = \frac{\sum_{k_y} \Delta_i(k_y)\Delta_j(k_y)}{\sqrt{\sum_{k_y} \Delta_i^2(k_y)}\sqrt{\sum_{k_y} \Delta_j^2(k_y)}}. \tag{5.2}$$

From the measured spectra (insets in Fig. 5.5) we calculate the set of all values q of q_{ij} for each different realization, determining their distribution $P(q)$, which is a leading quantity for the description of disordered and glassy phases. Results are reported in Fig. 5.6 and show standard (gaussian) overlap distribution, implying that no replica symmetry breaking occurs. In fact, the majority of overlaps are centered around the zero value, meaning that spatial optical modes are independent and do not interact significantly; consistently, their fluctuation are randomly correlated. We note that the asymmetry in $P(q)$ (depletion of large negative q values) results from the fact that large part of the single-shot spectra vanishes, i.e., positive fluctuations respect to the mean spectrum are favored. The normal overlap distribution occurs for the modulational unstable regime, where large positive overlap are partially detected in agreement with the bunching in Fig. 5.5, as well as in the turbulent state. The first result confirms the prevailing stochastic nature of the modulation instability phenomenon. The second prove that mode-locking in the mechanism leading to rogue waves is absent or not detectable in our case [20].
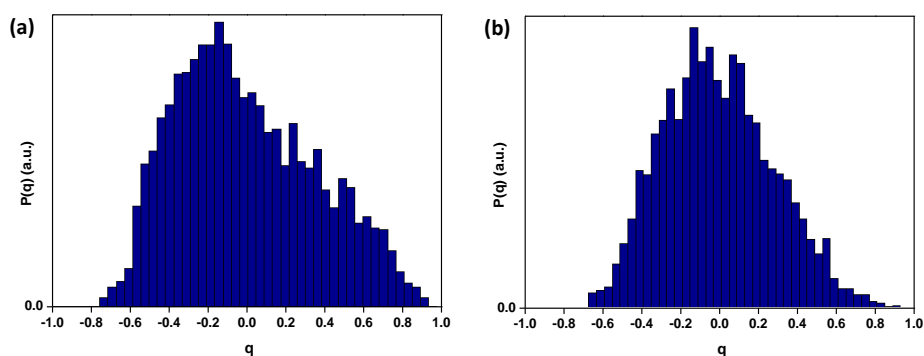
Figure 5.6. Overlap distribution of shot-to-shot spectral correlations. (a) $P(q)$ for the modulational unstable regime ($t/\tau \approx 1$) and (b) in the optical turbulent state at $t/\tau \simeq 2.5$. In both cases overlap is normally (stochastically) distributed and no replica symmetry breaking occurs, although the presence of large positive q values for modulational instability stresses the presence of an interaction between spectral excitations (bunching in Fig. 5.5).

Chapter 6

Control of rogue waves through spatial incoherence

Active control of extreme events emerging in photorefractive wave dynamics is demonstrated through spatial incoherence of the optical field [223]. Varying the correlation length of the input beam, we observe a scale-dependent statistics in which rogue wave appearance can be suppressed or strongly enhanced. These results allow us to point out a comprehensive understanding of rogue waves formation in nonlinear beam propagation. Specifically, using high-resolution measurements of the rogue waveforms, we prove that their statistical behavior relies on the existence of a typical spatial scale in rogue waves appearance. Intensity results to be independent from this preferred size that coincides with the minimum soliton size permitted by the saturation in the response. The findings suggest that in spatially-extended saturable systems the emergence, properties, and control of extreme events are intimately connected to non-stationary solitons typical of a saturable cumulative nonlinearity. This said, we should note that, in spite of the different mechanism underlying extreme events in physics, only a small subset of its have allowed the possibility of controlling rogue waves [261, 96, 46]. Control of rogue waves stands as the fundamental goal and remains challenging especially for high-dimensional systems with spatial extension, such as beam propagation, where many degrees of freedom come into play.

6.1 Incoherent excitations and extreme events control

In our experiments we make use of partially-incoherent beams propagating in photorefractive ferroelectrics, in the same conditions in which turbulent states with rogue waves have been observed starting from coherent and quasi-homogeneous one-dimensional input excitations (Chapter 4 and Chapter 5). Changing the spatial coherence of the input conditions, we can study the effects of the optical correlation scale on rogue waves formation. Setup and methods are shown schematically in Fig. 6.1(a). They are based on the peculiar nonlinear optical properties of disordered ferroelectric crystals in proximity of their structural phase transition previously investigated and on the photorefractive propagation of partially-incoherent beams [189, 61]. Light at a wavelength $\lambda = 532nm$ from a $150mW$ continuous-
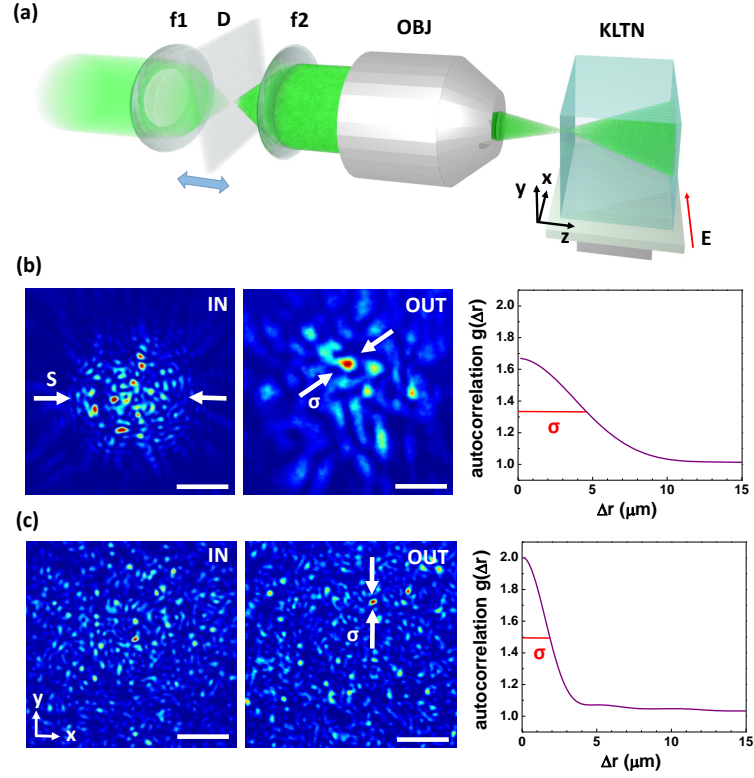
Figure 6.1. Partially-incoherent beams in photorefractive ferroelectric crystals. (a) Sketch of the experimental setup with lenses ($f1 = f2 = 50mm$), adjustable glass diffuser D (average particle size of $2\mu m$), long-working-distance objective OBJ ($NA = 0.55$) and KLTN sample. (b-c) Input and output intensity distributions with the corresponding spatial autocorrelation function $g(\Delta r)$ for two different positions of the scatterer. σ indicates the output autocorrelation length and S is the corresponding input source size. Scale bars correspond to $30\mu m$. (From [223]).

wave laser is expanded and focused on a glass diffuser plate, where transmitted radiation is collected producing a collimated speckle field. A long-working-distance objective ($NA = 0.55$) launches this field at the input facet of a KLTN crystal, $K_{1-\alpha}Li_\alpha Ta_{1-\beta}Nb_\beta O_3$ ($\alpha = 0.04$, $\beta = 0.38$). The partially-incoherent beam, linearly polarized in the experimental plane, copropagates with a background intensity along the z-axis of the crystal and is detected at the output facet through a high-resolution imaging system ($NA = 0.50$) and a CCD camera. The sample is a zero-cut optical quality specimen with size $2.4^{(x)}x2.0^{(y)}x1.7^{(z)}mm$ (l_x x l_y x l_z) and with the ferroelectric transition occurring at the Curie temperature $T_C = 294K$. As in Chapter 5, turbulent light dynamics can be studied and controlled with high reproducibility at $T = T_C + 2K$. The incoherence properties of the input beam are achieved placing the diffuser inbetween two confocal lenses ($f1$ and $f2$) and varied changing its position along the propagation axis, whereas small tilts and rotations on it generate different disordered realizations of the optical field. Examples of partially-incoherent beams at the crystal input and output are reported in Fig. 6.1(b-c) for two positions of the scatterer along the propagation axis. For the output
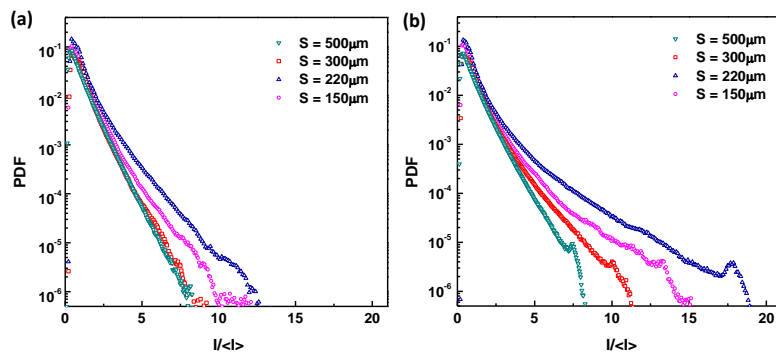
Figure 6.2. Controlling extreme events: scale-dependent behavior of the intensity statistics. (a) PDF measured in linear conditions ($E = 0$, $P = 400\mu W$) for beams with different coherent length expressed through the input parameter S. (b) Corresponding distributions for nonlinear propagation ($E = 2kV/cm$, $P = 400\mu W$), showing a long-tail behavior depending on the specific correlation length, with a large enhancement in rogue waves appearance for $S = 220\mu m$. Suppression of the tail occur for highly-incoherent fields ($S = 500\mu m$). (From [223]).

intensity distribution we consider the spatial autocorrelation function

$$g(\Delta r) = \frac{\langle \int d^2 r I(r) I(r + \Delta r) \rangle}{\int d^2 r \langle I(r) \rangle \langle I(r + \Delta r) \rangle},\tag{6.1}$$

whose width defines the spatial correlation length σ, i.e. the average speckle size. Since σ varies as nonlinear effects are involved in wave dynamics [47], we use the input source size S as a parameter characterizing the spatial incoherence of the input beam. We have $S \simeq 2\lambda l_z/g(0)\sigma$, which generalizes to nonlinear conditions optical speckle propagation [47, 90].

Extreme event control is shown in Fig. 6.2, where the detected probability distribution function (PDF) of the output intensity is reported varying the beam incoherence both in the linear and nonlinear case. In linear conditions, where no external field is applied, we observe (Fig. 6.2(a)) no significant deviations from the gaussian statistics as expected for completely-random interfering waves [119]. The exponential scaling $PDF = \exp(-I/\langle I \rangle)/\langle I \rangle$ is well verified in particular for beams presenting spatial coherence only on small scales ($S \approx 500\mu m$, $S \approx 300\mu m$). For more correlated beams ($S \approx 220\mu m$, $S \approx 150\mu m$), the PDF slightly deviates at large intensities, consistently with the presence of weak inhomogeneities in the phases of the elementary interfering waves [19, 170]. Rogue waves occur as the nonlinearity is activated by means of the external field $E = 2kV/cm$. In the nonlinear case, in analogy with coherent and quasi-homogeneous beams, the incoherent field experiences strong self-interaction and spatiotemporal fluctuations so that we observe the speckle intensity dynamically varying in a turbulent fashion. The nonlinear regime appear completely different from that observed in Ref. [47] where single speckles simply focus, although in this case we cannot establish the threshold corresponding to the turbulent transition from the loss of coherence. To study the statistics in this stage, we acquire more than two hundred independent spatial distributions for a fixed $400\mu W$ input power and sample conditions. Results as a function of the

coherence length are shown in Fig. 6.2(b) and demonstrate how extreme events can be controlled through this parameter. We found the long-tail statistics defining rogue waves and a peculiar scale-dependent behavior. Specifically, the spatial correlation scale of the optical field strongly affects its PDF, with a large enhancement in extreme event appearance that occurs for incoherent beams of size $S \approx 220\mu m$ and their complete suppression at $S \approx 500\mu m$. We note that the effect is approximately independent of the input power and of the value of the applied field, provided that both are above a certain threshold ensuring the highly-nonlinear turbulent dynamics (section 5.1). Therefore, we observe that small-scale random intensity fluctuations inhibit rogue wave generation, whereas a peculiar increase in their probability is triggered by a specific beam coherence scale. We note that a similar inhibition for highly-incoherent waves has been also reported in the temporal turbulent dynamics of passive optical fiber ring cavity [71]. On the contrary, enhancement for a specific excitation scale has never been observed.

6.2 The characteristic scale of rogue waveforms

To investigate the mechanism underlying the correlation between abnormal wave statistics and incoherence scale, we use our ability with the present setup to resolve the spatial waveform of each event with $0.3\mu m$ resolution (for typical wave features of 10 μm). We first consider the data set with incoherence corresponding to the maximum statistical-tail enhancement and, in particular, we analyze the rogue wave peak intensity I_P and its full-width-at-half-maximum ΔX. Examples of spatially-resolved rogue waveforms emerging from partially-incoherent intensity distributions are shown in Fig. 6.3(b) as giant pulses. In Fig. 6.3(a) we report an interesting behavior that is found for the two analyzed parameters: even though the abnormal waves span different peak intensities, their width is almost constant. Localized events appear with the same transverse size irrespective of the fact that they populate the gaussian portion of the PDF or the extreme one of its abnormal tail. This feature persist also at different bias fields and, as further shown in the following, it amounts to a general property of rogue waves in the saturable nonlinearity. Therefore, we
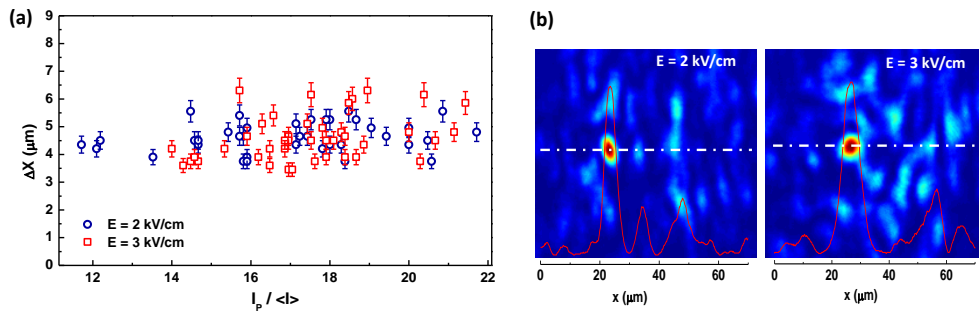

Figure 6.3. Unveiling optical rogue waveforms. (a) Detected transverse width ΔX and peak intensity I_P of extreme events for data at different applied fields. (b) High-resolution spatial intensity distributions containing localized abnormal waveforms. Red curves are x-profiles along the dotted lines. (From [223]).
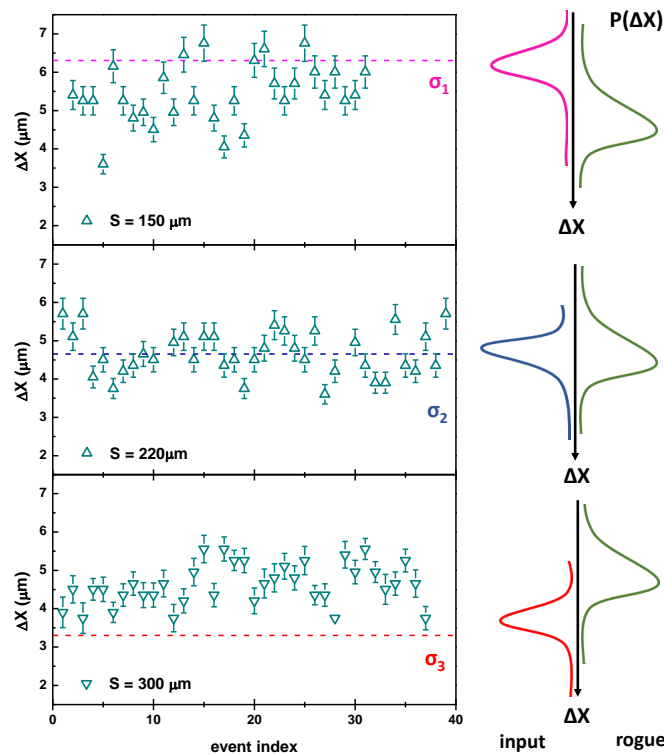
Figure 6.4. Evidence of a typical scale in rogue waveforms. Measured extreme events widths at different coherence length σ (dashed lines). The two scales are resonant for $S = 220\mu m$, where a large increase results in the probability of rogue wave appearance (see main text and Fig. 6.2(b)). The diagram on the right illustrates how results imply the presence of a typical spatial scale for rogue events. (From [223]).

extend our analysis taking into account the width of the extreme events as a function of the degree of incoherence of the corresponding optical field. Specifically, we compare their typical scale ΔX with the correlation scale σ of its entire intensity distribution, obtained in the nonlinear regime according to Eq. (6.1). This allows us to inspect whether the rogue wave has a size determined by the mean autocorrelation length of the speckle beam or an intrinsic properties is involved. The whole picture is presented in Fig. 6.4. Extreme events are found to emerge on a typical scale that is significantly lower or higher than the coherence one, respectively, for beams of size $S = 150\mu m$ and $S = 300\mu m$ (see Fig. 6.2(b)). Moreover, matching between these two scales is evident at $S = 220\mu m$, that is exactly the case in which the large enhancement in the long-tail statistics is detected. The findings prove that the key feature providing extreme event control is the existence of an intrinsic scale for rogue waves. We estimate it to approximately $\overline{\Delta X} = 4.5\mu m$. In fact, as schematically illustrated in Fig. 6.4, the coherence length distribution of the input beam acts as a probe for the probability $P(\Delta X)$ of finding extreme events with a certain width ΔX. Their overlap, in terms of sizes, sets the amount of emerging extreme events, so that the enhancement at $S = 220\mu m$ appears as a resonant interaction.
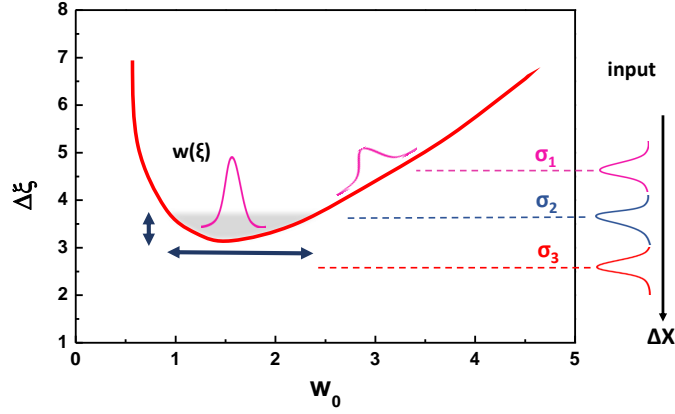
Figure 6.5. Mechanism underlying appearance and control of extreme intensity fluctuations. Existence curve of non-equilibrium solitons in saturable nonlinearities (red line) on which the waveform $w(\xi)$ is schematically shown. Arrows indicate the magnitude of width and amplitude fluctuations in the gray region, which is in proximity of the localized, self-trapped, wave solution. For comparison with Fig. 6.4 and Fig. 6.2, input correlation lengths used in experiments are also reported. (From [223]).

6.3   Origin of rogue waves in photorefractive dynamics

The existence of a preferential size for extreme waves provides an active method to set statistically their appearance. In particular, once the nonlinear propagation conditions are fixed, the spatial correlation of the optical field can be tuned to arbitrarily modify the intensity distribution tail. The generality of this mechanism relies on the physical basis that leads to a typical size for rogue events [199]. We address the fundamental question on its origin starting from the consideration that the main properties of the photorefractive nonlinearity underlying our turbulent optical dynamics is its saturable character. Since saturation turns out in the response of any real system for large excitations, the finding may represent a universal trait in abnormal wave events, at least in this limit condition. For our system, we here provide a physical picture that not only explains the presence of a peculiar spatial scale, but also the observed insensibility to wave intensity. We note that such feature of the rogue waveform is consistent with observations in our first experiments (section 4.2.2), where it was noted as an anomaly in their self-similarity and has led us to consider numerical results as controversial. The framework we consider remains based on spatial solitons, whose structural and interaction properties are candidate to play a key role for rogue waves. However, motivated by the spatiotemporal dynamics of the turbulent regime underlying extreme events, we focus our attention on their non-equilibrium counterpart, i.e., transient self-trapping waves in non-stationary conditions as treated in section 1.3.1. As detailed in Ref. [84], in the present case, transverse localization occurs on a size (Eq. (1.35))

$$\Delta x \simeq \frac{3\lambda}{2\pi n^2 a_{eo}} E^{-2}, \tag{6.2}$$

where we rename a_{eo} the parameter quantifying the electro-optical response of the media. For our experimental realization, we have $\Delta x = 5 \pm 1\mu m$, where the

uncertainty is related to the uncertainty in a_{eo} in proximity of the ferroelectric phase transition for biased condition. This value of Δx is consistent with the typical scale of rogue waveforms $\overline{\Delta X}$ we have found. Moreover, Eq. (6.2) possess the fundamental property of being independent on the wave intensity, in agreement with our observations of extreme events (Fig. 6.3(a)). Dependence on the external electric field E is predicted as very weak at high values (compare with Fig. 1.4) and the result in Fig. 6.3(a) with different bias fields verifies also this feature. Therefore, observations strongly suggest that control of long-tail statistics with spatial incoherence and their spontaneous emergence in optical turbulence can be explained with the mechanism illustrated in Fig. 6.5, where the phase-space of the nonlinear waves in terms of normalized amplitude w_0 and width $\Delta \xi$ (existence curve) is recalled. Non-equilibrium self-trapped waves form across the minimum of the existence curve according to Eq. (6.2) triggered by fast temporal fluctuations of the beam intensity distribution, which are mediated by fast fluctuations in the nonlinear response. As chaotic time evolution locally brings the specific nonlinear wave in this phase-space point, a localized mode is observable. Here, a small variation in $\Delta \xi$ can lead to large fluctuations of the wave amplitude, with peak intensities reaching the giant values that populate the extreme regions of the total PDF. Extreme events are enhanced when the input coherence scale falls in this region, whereas their excitations and suppression implies, respectively, that matching with the input autocorrelation is partial or does not occur at all. These results open important routes for control and management of abnormal intensity localization in spatially-extended optical systems and demonstrate the role of scales in nonlinear turbulent dynamics as a key point to its understanding.

Chapter 7

Scale-free optics and anti-diffraction of light

In this Chapter we report nonlinear optical wave phenomena in which beam self-action is mediated by the giant diffusive nonlinearity provided by out-of equilibrium disordered ferroelectrics. In particular, we discuss regimes in which the diffraction of light can be cancelled using an intensity independent nonlinear response that acts in the form of an anti-diffraction. Diffraction cancellation, discovered by *DelRe et. al.* [88], implies that beams do not spread because diffraction is absent, and not simply because it is compensated by an index of refraction pattern, such as in a waveguide, or because of a nonlinear index change, such as in spatial solitons. In both these cases, diffraction compensation introduces limits on the non-spreading waves, such as the optical modal structure of the waveguide and the soliton existence conditions, that require specific solutions to allow effective field transfer. In diffraction cancellation, these strict laws are absent and the optical propagation occurs without any limit associated to the optical wavelength [206], a condition termed scale-free optics [88]. This regime is here observed for the first time from wide plane-wave-like beams that obey geometrical optics down to ultranarrow beams with widths of the order of a single wavelength, a single unified light behavior that spans across the entire hierarchy of standard optical spatial scales [92]. Moreover, the unique features of the system allow us to observe anti-diffraction of light, that is beams shrinking below their diffraction-limited size [93]. The anti-diffracting behavior can be extended to sub-micrometrer-sized light beam that can be focused to dimensions smaller than the diffraction limit [89]. In this regime the propagation of the electromagnetic fields is no longer governed by the Helmholtz equation but instead is modified into a Klein-Gordon-type equation, a property with profound implications for wave dynamics.

7.1 Diffraction cancellation for non-paraxial beams

Light beams confined to widths comparable to their wavelength are no longer described by ray optics and diffract. Light spreads during propagation with an angle that is proportional to the ratio between the wavelength λ and the transverse size of the beam w_0, i.e., $\Delta\theta \sim (w_0/\lambda)^{-1}$ [196]. Beyond scale-free optics, diffraction can
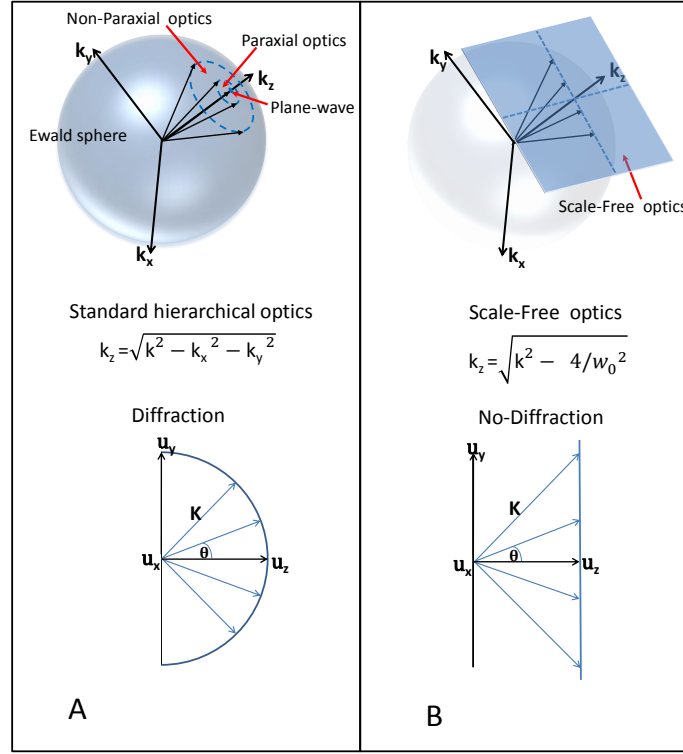
Figure 7.1. Comparing standard optics and scale-free optics. In the *k*-vector space, the plane-wave, the paraxial, and non-paraxial regimes can be schematically represented as regions of respectively increasing surface in the Ewald sphere $\mathbf{k} \cdot \mathbf{k} = (2\pi/\lambda)^2$ (a). Different plane-wave components emerging from a point-like source have different phase-velocities along a given direction of propagation $\mathbf{u}_z$, since their projection k_z is different, so as to causes diffraction. In the scale-free regime (b), in turn, the allowed k-vectors are on a plane orthogonal to the propagation direction $\mathbf{k}_z$, so that $\mathbf{k}_z$ does not depend on the angle of the plane-wave components with respect to the z-axis, and the wavefront suffers no diffraction. (From [92]).

be cancelled in periodic index of refraction patterns [155, 264] and electromagnetic-induced transparency [104]. The problem with all these approaches is that they are limited to paraxial conditions, where $\Delta\theta \ll 1$ and diffraction causes only limited distortion. Theoretical models indicate that, in principle, scale-free optics supported by the diffusive nonlinearity [63, 75, 81] should allow diffraction-cancellation also in the non-paraxial regime [74].

7.1.1   The scale-free optics model

According to the macroscopic Maxwell equations, a linearly polarized optical field $\mathbf{E} = \hat{\mathbf{x}} E \exp{(i k_z z)}$ propagating inside an inhomogeneous transparent material obeys the Helmholtz equation

$$\nabla^2 E + (\omega n/c)^2 E = 0, \tag{7.1}$$

the basic wave equation $\nabla \wedge \nabla \wedge \mathbf{E} = (\omega n/c)^2 \mathbf{E}$ where coherent vectorial coupling is neglected ($\nabla\nabla \cdot \mathbf{E} \simeq 0$). Here ω is the optical angular frequency and c is the speed of

light in vacuum ($2\pi/\lambda = \omega/c$). When in photorefractive crystal electronic diffusion is the main transport mechanism associated to light absorption, the space-charge field assumes the form in Eq. (1.13). This electric field $\mathbf{E}$ give rise to a scalar change $\Delta n = -(n^3/2)g\epsilon_0^2\chi_{PNR}^2|\mathbf{E}|^2$, where we indicate low-frequency susceptibility with χ_{PNR}, since in out-of equilibrium conditions in proximity of the ferroelectric phase transition the local dielectric response can results strongly affected by polar-nanoregions (Chapter 2). Therefore, the nonlinearity Δn is given by

$$\Delta n = -\frac{n^3}{2}g\varepsilon_0^2\chi_{PNR}^2\left(\frac{K_bT}{q}\right)^2\frac{(\partial_x I)^2 + (\partial_y I)^2}{I^2}. \tag{7.2}$$

When $g > 0$ (focusing nonlinearity), the generalized NLSE describing paraxial wave propagation (Eq. (1.26)) becomes

$$(2ik\frac{\partial}{\partial z} + \nabla_{xy}^2 - \frac{L^2}{\lambda^2}\frac{(\partial_x I)^2 + (\partial_y I)^2}{4I^2})A = 0, \tag{7.3}$$

where $L = 4\pi n^2\varepsilon_0\sqrt{g}\chi_{PNR}(K_bT/q)$ is the spatial scale used to factor out the wavelength scale. The nonlinear term is not truly an anti-diffraction operator $\propto \nabla^2 A$, since the response will amount to a term $\propto (|\nabla I|/I)^2A$. However, both terms are independent of peak intensity, and both have the same fundamental scaling in terms of the spatial extent of the beam, i.e., both are $\propto 1/w_0^2$. These two facts guarantee a diffraction cancellation for arbitrary waveforms, and an exact mathematically rigorous cancellation for the solutions that we discuss in what follows. For all cases, in conditions in which the nonlinear length scale $L \simeq \lambda$, scale-free optics is observed. In the nonparaxial regime, Eq. (7.1) should be explicitly considered instead of Eq. (7.3), and for the diffusive nonlinearity it reads [74]

$$-\frac{\nabla^2 E}{E} + \left(\frac{L}{\lambda}\right)^2\left(\frac{\nabla|E|^2}{2|E|^2}\right)^2 = k^2, \tag{7.4}$$

where L is the characteristic nonlinear length above introduced. The scale-free condition holds when $L = \lambda$ for which Eq. (7.4) retains a trace of λ only through a constant in the second term. In this case, one has the analytic approximated solution $E = E_0\exp\left(-(x^2 + y^2)/w_0^2\right)\exp\left(-ik_z z\right)$ which is scale free, i.e., it forms for an arbitrary amplitude A_0 and waist w_0, with

$$k_z = \sqrt{\left(\frac{\omega n}{c}\right)^2 - \frac{4}{w_0^2}}. \tag{7.5}$$

This solution exists, i.e., k_z is real, as long as $w_0 > 2c/\omega n = 2\lambda/\pi n$. Since it holds directly for the Helmholtz equation, it is valid irrespective of whether the beam is plane-wave-like ($w_0/\lambda \gg 10$), paraxial ($w_0/\lambda \sim 10$), or non-paraxial ($w_0/\lambda \sim 1$) (scale-invariance). The comparison between standard optics and scale-free optics is schematically represented in Fig. 7.1.

7.1.2 Diffraction management through thermal shocks

Here we report the observation of scale-free propagation across the entire range of possible propagating beam widths, from plane-waves to non-paraxial waves, for
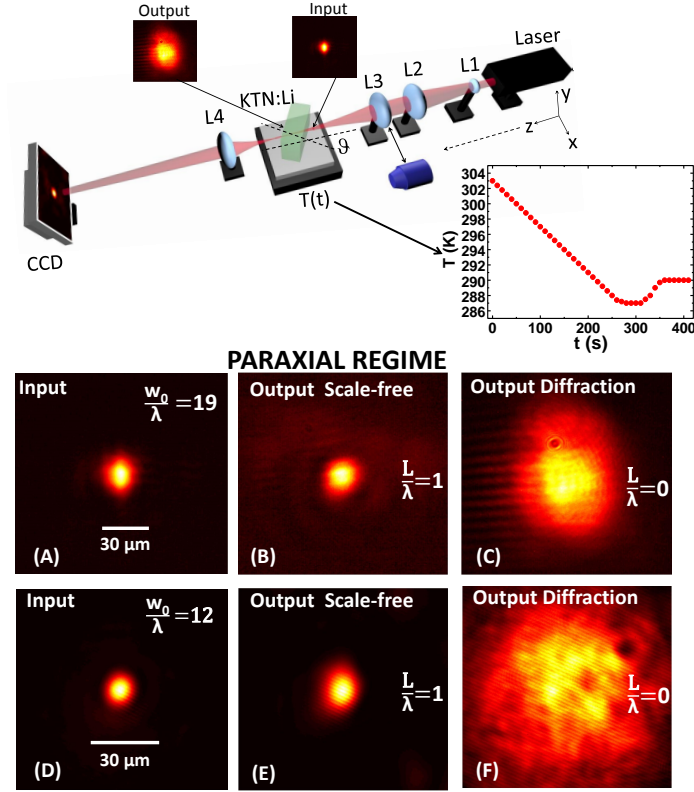
Figure 7.2. Diffraction cancellation in the paraxial regime. Top, experimental setup and thermal shock protocol (temperature cycle $T(t)$). Bottom, paraxial scale-free propagation. In the highly paraxial regime ($w_0/\lambda \gg 10$), the $12\mu m$ Gaussian beam input (a) is compared with the $13\mu m$ scale-free output waist ($L/\lambda = 1$) (b) and the $27\mu m$ diffraction output ($L/\lambda = 0$) (c). Analogously, in a weaker paraxial condition ($w_0/\lambda \sim 10$), the input $7.8\mu m$ Gaussian beam (d) is compared to the $9\mu m$ scale-free output waist ($L/\lambda = 1$) (e) and the $38\mu m$ diffraction output ($L/\lambda = 0$) (f). (From [92]).

$w_0/\lambda = 0.8 - 20$. To fulfill the scale-free condition in the non-paraxial regime we make use of thermal shocks causing a transient $L(t)$ on a photorefractive disordered ferroelectric KLTN. The experimental setup is illustrated in Fig. 7.2. A $0.8mW$ (measured before L3) He-Ne laser operating at $\lambda = 632.8nm$ is expanded (L1 and L2) and subsequently focused (L3) down to a spot at the input face of a sample, using spherical lenses for the paraxial regime or microscope objectives ($NA = 0.50, 0.80$) for the non-paraxial regime. The crystal is a zero-cut $2.6 \times 3.0 \times 6.0$ mm sample with a composition of $K_{1-x}Li_xTa_{1-y}Nb_yO_3$ with $x = 0.003$, $y = 0.36$. Cu impurities (~ 0.001 atoms per mole) support photorefraction in the visible, whereas focusing and cross-polarizer experiments give $n_0 = 2.2$ and $g = 0.14m^4C^{-2}$. At visible wavelengths, the crystal absorption coefficient is $\alpha \simeq 2cm^{-1}$. The beam is polarized in the x direction and propagates inside the crystal for a distance of $L_z \simeq 3.0$mm. The crystal is rotated to a desired angle θ in the x, z plane. The output intensity distribution of the beam is imaged by a CCD camera through an imaging lens (L4, NA$\simeq 0.35$). The $L = \lambda$ condition forms during a transient by operating near $T_m = 287.5K$ using a specific thermal shock protocol [207] shown in Fig. 7.2. The
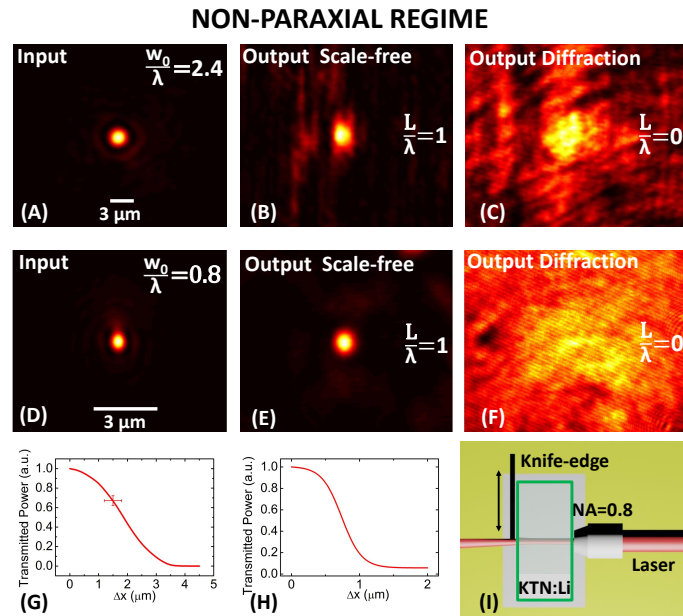
Figure 7.3. Non-paraxial scale-free propagation. A non-paraxial $w_0 = 1.5\mu m$ ($w_0/\lambda = 2.4$) input beam (a) is compared with the $1.7\mu m$ scale-free output waist ($L/\lambda = 1$) (b) and the $> 60\mu m$ greatly delocalized output ($L/\lambda = 0$) (c). Analougosly, in the highly non-paraxial condition ($w_0/\lambda = 0.8$), the input $0.49\mu m$ beam (d) is compared with the $0.66\mu m$ scale-free output waist ($L/\lambda = 1$) (e) and the $> 90\mu m$ delocalized output ($L/\lambda = 0$) (f). (g-h) Knife-edge scan for (a) and (d) cases. (i) Knife-edge scheme for output distributions. (From [92]).

method is based on a general property of glassy phases known as Kovacs, or cross-over, effect [165, 156, 15, 193] and requires operating the sample in its non-ergodic phase. The shock leads to transient anomalous response with even more elevated values of χ_{PNR} [216]. However, we stress that the thermal shock we adopt is just an experimental technique; ferroelectric crystals with a larger equilibrium response would allow avoiding thermal treatment of the sample. The same statement holds for the transient nature of the phenomena observed. The crystal was first cleaned of photorefractive space-charge by illuminating it with a microscope illuminator. Using a temperature controller that drives the current of a Peltier junction placed directly below the crystal in the y-direction, we brought the sample to thermalize at $T_A = 303$K. The sample is then cooled from $T_A = 303$K at the rate of $0.06K/s$ to a temperature $T_D = 287$K, where it is kept for $60s$. Then the sample is heated once again at a rate of $0.1K/s$ to the operating temperature ($> T_D$) $T_B = 290$K, with $\Delta T = T_B - T_D$ defining the shock amplitude. The crystal is kept in air at atmospheric pressure and is subjected to a temperature gradient orthogonal to the beam propagation ($z - x$ plane). The thermal gradient may pins the polar-nanoregions inducing a polarization selective nonlinearity. Hence, in our sample we are limited to a scale-free regime for x-polarized beams. Once T_B is reached, the temperature cycle $T(t)$ is complete and we switched on the laser beam, recording front view images of the captured intensity distribution. The strong transient response

is observed to have a characteristic response time of $10 - 30s$. The time scale of the transition into the diffraction cancellation regime starting from the diffractive regime is, in our conditions, approximately peak-intensity-independent. This means that the time dynamics are associated to the relaxation of the metastable dipolar state, while the photorefractive build-up is faster and the space-charge field is at all times approximately at the steady state. We evaluate the value of L by measuring the output and input waist ratio; when this ratio reaches unity we have $L \simeq \lambda$. An independent evaluation of L can ideally be obtained through time-resolved dielectric constant measurements at low frequencies of χ (and hence χ_{PNR}). However, these measurements will only capture an averaged value of the χ_{PNR}, which, in proximity of the peak, leads naturally to a lower value of the enhanced dielectric constant and a diffused peak.

In Fig. 7.2 we report scale-free propagation for paraxial beams. As shown in Fig. 7.2(a-c) the $w_0 = 12 \mu m$ ($w_0/\lambda = 19$) input beam diffracts to $27 \mu m$ as it propagates to the output facet at the initial $T_A = 303K$. After the cooling/heating cycle, the output beam shrinks to $13 \mu m$. Analogously in Fig. 7.2(d-f), the $w_0 = 7.8 \mu m$ ($w_0/\lambda = 12$) input beam diffracts to $38 \mu m$, then shrinking to $9 \mu m$. Confirmation that it is associated to diffraction-free propagation all along the sample is provided by top view images of scattered light. In Fig. 7.3 we report scale-free propagation for the non-paraxial beams. In Fig. 7.3(a-c), a $w_0 = 1.5 \mu m$ input beam ($w_0/\lambda = 2.4$) is launched directly from a zero-working-distance immersion microscope objective ($NA = 0.8$, used without oil with $\theta = 0$) placed at the input face of the sample. After we enacted the thermal cycle, in the scale-free regime we measured a $1.7 \mu m$ output waist. In Fig. 7.3(d-f), the narrower input beam with $w_0 = 0.49 \mu m$ ($w_0/\lambda = 0.8$) is achieved using a fully illuminated long-working-distance dry objective ($NA = 0.8$, $\theta = 11°$ to avoid the effect of growth-related striations). In the nonlinear regime we measured a $0.66 \mu m$ output waist. The beam width is measured using a knife-edge technique in proximity of the input plane, from the transmitted power plot (Fig. 7.3(g-h)) by fitting the data with what is expected for a two-dimensional gaussian beam intensity shape of width w_0. In detail, we mounted a plate on a 3-axis nanopositioning stage, aligned it to the plane orthogonal to the z-axis and placed it in proximity of the output plane of the objective, to a precision below $1 \mu m$ (the confocal parameter of the beam is on the order of tens of micrometers). The power of the transmitted light as a function of the lateral x-displacement of the plate edge δx was then detected using a silicon-head power-meter. The transmitted power P_{out} normalized to the maximum transmission P_{max} follows $P(\Delta x)_{out}/P_{max} = (1/2)(1 - \text{erf}(\sqrt{2}\Delta x/w_0))$, so that the displacement d that brings the normalized fraction from 0.75 to 0.25 quantifies the beam width $w_0 \simeq \sqrt{2}d$.

In Fig. 7.4 we combine results and illustrate in its full the breaking of the conventional optical spatial hierarchy. We note that a similar scale-invariant picture has been recently found also in nonlinear paraxial propagation of light in gases [138]. These findings can form the basis for super-resolved imaging. In fact, in standard optical propagation a finite angular spread implies loss of original resolution during propagation and hence a distortion of images. The diffraction-cancellation regime allows the preservation of the spatial resolution of light emitted from a plane as propagates to collecting optics. Hence, in principle, we can interpose a slab of KLTN inbetween the objective of the microscope and the sample to analyze. The increase
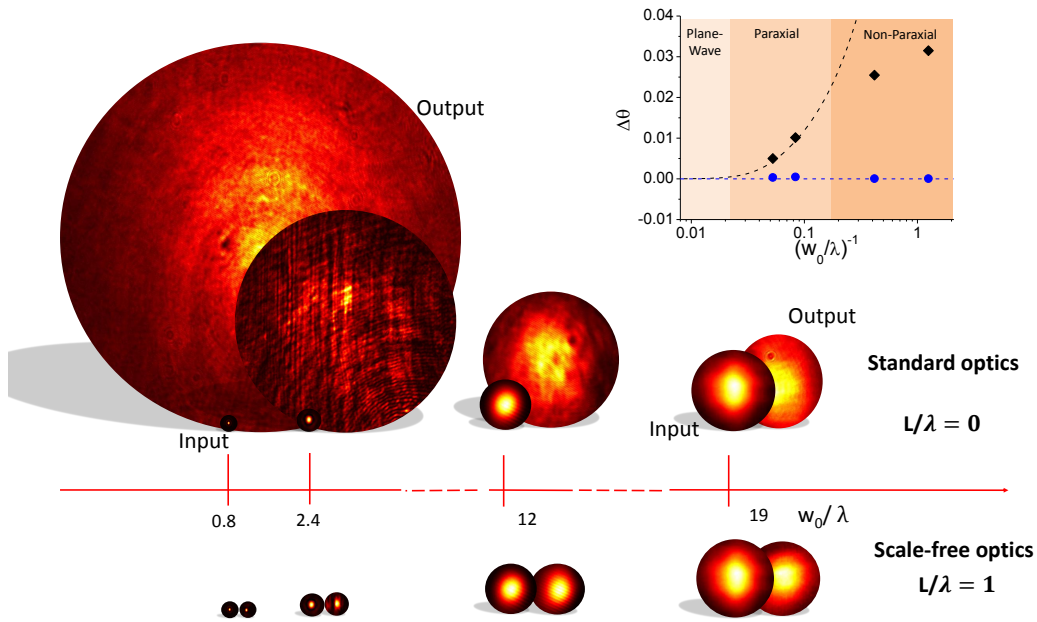
Figure 7.4. Scale-invariant optics: the full picture. Comparison of input versus output beam intensity distribution (see inset) in standard optics ($L/\lambda = 0$, top sequence) and in the scale-free optics regime ($L/\lambda = 1$, bottom sequence), as function of w_0/λ. The use of a single common spatial scale illustrates the fundamental difference between the standard scale-hierarchy (top) and scale-free case (bottom) across the entire span of optical regimes, i.e., from plane-waves to non-paraxial waves. (From [92]).

in depth-of-focus for a fixed collecting numerical aperture amounts to an increase of the overall effective resolution [28]. For example, a visible pixel ceases to represent an independent source of information when it becomes equal to or smaller than a micrometer, in which case $\Delta\theta \sim 1$ and its emission is mingled to that of other pixels after just a few micrometers of propagation. No such distortion will occur if the pixels were to transmit light in a system supporting scale-free optics. Summing up, although Maxwell's equations are free of any spatial scale, in all practical devices this scale-symmetry is broken by the wavelength λ around which a specific device operates. The wavelength introduces a hierarchy of different propagation phenomena as measured in terms of the ratio between the light beam width w_0 and λ, as quantified by the angular spread of the beam $\Delta\theta$. Starting from the quasi-monochromatic reduction of the electromagnetic wave equation, we can distinguish a so-called non-paraxial regime described by the Helmholtz equation for $w_0/\lambda \sim 1$, a paraxial regime described by the parabolic propagation equation for $w_0/\lambda \sim 10$, and a plane-wave geometrical optics regime for $w_0/\lambda \gg 10$. In a diffusive nonlinearity supported by a disordered photorefractive ferroelectric crystal, we are able to observe beams without diffraction independently of size and intensity across the entire span of these commonly accepted wave-propagation regimes. In other words, in the present nonlinear wave propagation, all light beams obey geometrical-optics-like laws.

7.2 Anti-diffracting wave propagation

Wave propagation in diffusive nonlinearity can be extended to regimes with $L > \lambda$. In these conditions a more general effect would be involved: the observation of beams that literally anti-diffract as they propagate in a medium. In such a system, beams will naturally converge instead of spreading, irrespective of direction of propagation and for a wide range of beam sizes, even with a considerable angular spectrum. In distinction to self-focusing, which depends on intensity and generally becomes stronger up to breaking as beams shrink, anti-diffraction should be intensity-independent. In this section we theoretically predict anti-diffraction supported by the diffusive nonlinearity and report its first observation in lithium-enriched potassium-tantalate-niobate (KLTN) [93].

7.2.1 Collapse length

According with Eq. (7.3), the slowly varying optical amplitude A, self-interacting through a diffusive nonlinearity, in the paraxial approximation obeys the equation

$$2ik\frac{\partial A}{\partial z} + \nabla_\perp^2 A - \frac{L^2}{\lambda^2}\left(\frac{\nabla_\perp |A|^2}{2|A|^2}\right)^2 A = 0, \tag{7.6}$$

with $\nabla_\perp \equiv (\partial_x, \partial_y)$. Separating the variables, $A(x,y,z) = \alpha(x,z)\beta(y,z)$, α evolves according with

$$2ik\frac{\partial \alpha}{\partial z} + \frac{\partial^2 \alpha}{\partial x^2} - \frac{L^2}{\lambda^2}\frac{(\partial_x |\alpha|^2)^2}{4|\alpha|^4}\alpha = 0, \tag{7.7}$$

and the same equation holds for β replacing x with y. Eq. (7.7) is satisfied by the solution

$$\alpha(x,z) = \frac{\alpha_0}{\sqrt{w_x(z)}} e^{-\frac{x^2}{w_x^2(z)} + i\left[\phi_0(z) + \frac{1}{2}\phi_2(z)x^2\right]} \tag{7.8}$$

with

$$\phi_0(z) = -\frac{1}{kw_{0x}^2}\frac{\tan^{-1}(\sqrt{a}z)}{\sqrt{a}} \tag{7.9}$$

and

$$\phi_2(z) = \frac{az}{1 + az^2}. \tag{7.10}$$

Here $a \equiv (1 - L^2/\lambda^2)/k^2 w_{0x}^4$, w_{ox} is the initial beam in the $x-$direction, and α_0 is a constant. For a round launch beam with $w_{ox} = w_{oy} = w_0$, the evolution of the beam waist in two transverse dimensions along the propagation direction z is given by

$$w(z) = w_0\sqrt{1 + \frac{4}{k^2 w_0^4}\left[1 - \left(\frac{L^2}{\lambda^2}\right)\right]z^2}. \tag{7.11}$$

As $L > \lambda$, Eq. (7.11) foresees beams that shrink itself during propagation up to an ideal point-like focus at a characteristic collapse length

$$z_c = \frac{n\pi w_0^2}{\lambda}\frac{1}{\sqrt{(L/\lambda)^2 - 1}}, \tag{7.12}$$

which is independent of the beam intensity.

7.2.2   Observation of light anti-diffraction

To experimentally demonstrate diffusive anti-diffraction described by Eq. (7.12) we use the setup illustrated in Fig. 7.5, which is analogous to the one described in the previous section. However, in the present case light scattered in the vertical y-direction is captured by a second CCD camera placed above the sample in the y-direction through a high aperture microscope (NA$\simeq 0.8$) positioned to image the plane of propagation. We are able to achieve $L > \lambda$ during a transient by operating near $T_m = 287.5$K and enacting a non-monotonic temperature trajectory $T(t)$. In fact, considering the values of n, g, and $k_B T/q \simeq 25$ mV, $L \sim \lambda$ for $\chi_{PNR} \sim \lambda/(4\pi n^2 \epsilon_0 \sqrt{g}(k_B T/q)) \simeq 10^5$, i.e., an anomalously large value of susceptibility only observable through the Kovacs effect in proximity of the dielectric peak (see Fig. 7.2). In fact, this regime is not otherwise accessible with our apparatus by a standard rapid cooling (i.e., from T_A directly to T_B). Once T_B is reached, the temperature cycle $T(t)$ is complete and we switched on the laser beam, recording top-view and front view images of the captured intensity distribution. All intervals of time t are indicated such that the laser is turned on at $t = 0$. In Fig. 7.6 we show a condition of strong anti-diffraction observed when $T_D = 283K$. The $w_0 = 7.8\mu m$ input beam diffracts to $38\mu m$ as it propagates to the output facet at the initial $T_A = 303K$. After the cooling/heating cycle, the output beam shrinks to $5\mu m$ ($L \simeq 0.64\mu m$). Snapshots of the top-view scattered light illustrate the transition from the diffracting Fig. 7.6(d-f) to the shrinking beam condition Fig. 7.6(g), and ultimately to the once again spreading phase Fig. 7.6(h-i) with strongly reduced scattering. In this case, the crystal is rotated by $\theta = 11°$. The beam profiles of the input and output distributions (at $t = 15$s) are compared in Fig. 7.6(j). From Eqs. (7.11)-(7.12) we deduce a value of $z_c = 3.9mm$. To confirm the approximate intensity-independent and angle-independent nature of the effect, we repeated the experiment with different levels of beam power and propagation angles. We found same levels of anti-diffraction repeating experiments with $8, 30, 240, 800\mu W$ beams and for launch angles $\theta = 5° - 11°$. For example, at a fixed angle $\theta = 11°$, increasing
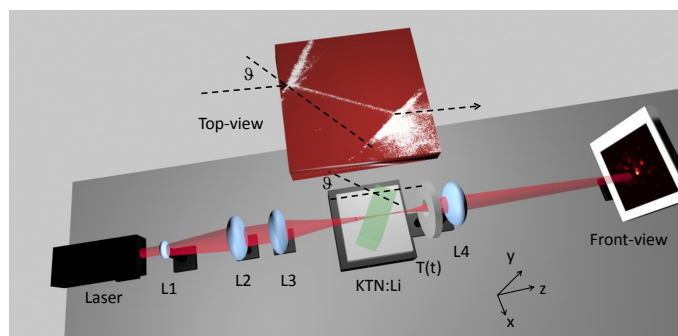
Figure 7.5. Anti-diffraction setup. A $633nm$ He-Ne laser is enlarged and focused down to an $8\mu m$ spot at the input facet of the KLTN, rotated by a variable angle θ respect to the z-axis and brought through a temperature cycle $T(t)$. (Front-view) The input and output facets are imaged through lens L4 onto a CCD camera. (Top-view) Scattered light is captured above the sample and imaged through a microscope. (From [93]).
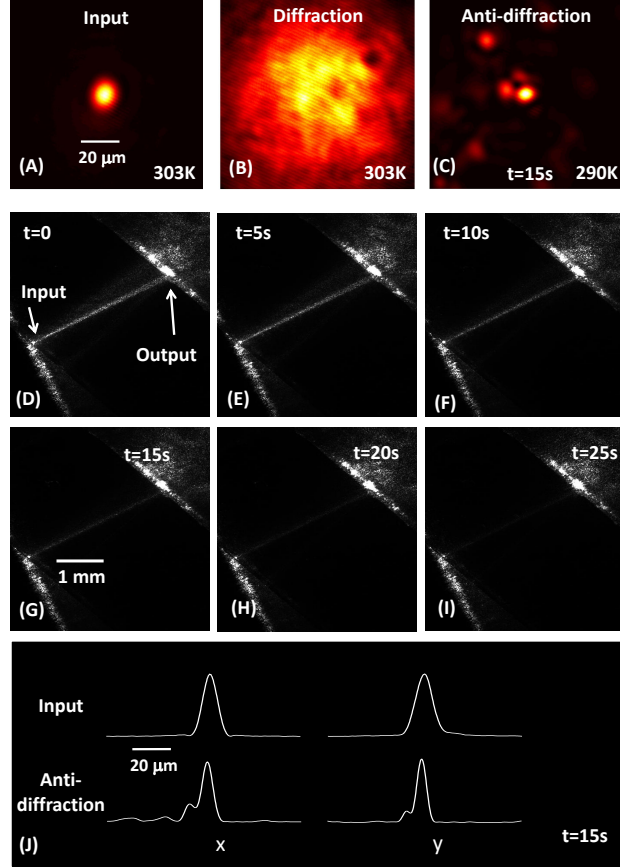
Figure 7.6. Observation of strong anti-diffraction. The input $800\mu W$, $8\mu m$ Gaussian beam (a) diffracts to $38\mu m$ at $T_A = 303K$ (b). For $T_D = 283K$ it then shrinks after $15s$ to a waist of $5\mu m$ (c), before relaxing once again into a strongly spreading beam. (d-i) Top-view images of the stray light emitted by the beam showing the transition, in time, from a diffracting (d) to an anti-diffracting beam (g), and once again to a diffracting one (i). Intensity profiles of the input beam compared to the anti-diffracting beam at $t = 15$s (j). (From [93]).

the beam power from $30\mu W$ to $240\mu W$, alters the minimum waist by less than 12%. The only relevant systematic effect associated with different beam powers was a lengthening of the anti-diffraction response time, as expected for the cumulative nature of the photorefractive response. However, the paraxial theory will break down if $L_z \simeq z_c$, where the strong-focusing requires a fully non-paraxial treatment and further novel effects are expected to emerge.

7.3   Subwavelength anti-diffracting beams

Propagating light beams with widths down to and below the optical wavelength require bulky large-aperture lenses and remain focused only on micrometric distances [136, 147]. Anti-diffraction into the subwavelength regime allows the observation of light beams that violate this localization/depth-of-focus law by shrinking as

they propagate so that resolution is maintained and increased over macroscopic propagation lengths [89]. The non-paraxial propagation of a sub-micrometer-sized beam for over 10^3 diffraction lengths in disordered ferroelectrics represents the narrowest visible beam to date reported [89]. The effect is possible as nonlinearity transforms the leading optical wave equation into a Klein-Gordon-type equation that describes a massive particle field [182].

7.3.1 Klein-Gordon-type wave behavior

To obtain the wave description for non-paraxial anti-diffracting beams we consider the full Helmholtz equation with a diffusive nonlinearity

$$\nabla^2\mathbf{E} - (L/\lambda)^2(|\nabla|\mathbf{E}|^2|/2|\mathbf{E}|^2)^2\mathbf{E} + k^2\mathbf{E} = 0. \tag{7.13}$$

To grasp intuitively how this model reproduces the Klein-Gordon (KG) regime typical of massive particles, we can consider localized Gaussian bubbles of light with $E \propto \exp\left(-r^2/w_0^2\right)$, where w_0 is the spatial extent of the optical excitation and $r^2 = x^2 + y^2 + z^2$. The evolution equation reduces to

$$\nabla^2\mathbf{E}(1 - (L/\lambda)^2) + (k^2 - (L/\lambda)^2(6/w_0^2))\mathbf{E} = 0, \tag{7.14}$$

so that for $1 < L/\lambda < (w_0 k/\sqrt{6})$ we have a relative change in sign in the terms of the equation, i.e., the time-independent KG equation $(\nabla^2 - n_m^2 k_0^2)\mathbf{E} = 0$, with

$$n_{\mathrm{m}}^2(L) = n^2(1 - (L/\lambda)^2(6/k^2 w_0^2))/((L/\lambda)^2 - 1). \tag{7.15}$$

For beam propagation along the z axis we can consider gaussian filaments $E \propto \exp\left(-r_\perp^2/w_0^2\right)B(z)$, where $r_\perp^2 = x^2 + y^2$. The wave equation now becomes

$$-\partial_{z'z'}^2 + \nabla_\perp^2\mathbf{E} - ((L/\lambda)^2 - 1)^{-1}(k^2 - (L/\lambda)^2(4/w_0^2))\mathbf{E} = 0, \tag{7.16}$$

where $z' \equiv z\sqrt{(L/\lambda)^2 - 1}$. For $1 < L/\lambda < (w_0 k/2)$ we have the KG equation

$$([] - n_m^2 k_0^2)\mathbf{E} = 0, \tag{7.17}$$

which corresponds to a relativistic particle with mass given by the Einstein relation $mc^2 = \hbar n_{\mathrm{m}} k_0 c$, with

$$n_{\mathrm{m}}^2(L) = n^2(1 - (L/\lambda)^2(4/k^2 w_0^2))/((L/\lambda)^2 - 1), \tag{7.18}$$

$[] \equiv -\partial_{z'z'}^2 + \nabla_\perp^2$, time being played by z'. This approximate treatment also indicates that, for a given $L/\lambda > 1$, the KG equation will once again be superseded by the Helmholtz equation for beam widths below $w_0 = (L/\lambda)2/k$. We stress that anomalous light behavior is activated without affecting the values of material susceptibility, without nanostructuring, or absorption, and consistently through the small nonlinear optical response regime (the maximum local value of index modulation is $\Delta n \ll n$ ($\Delta n/n \sim 10^{-4}$ for $w_0 \sim 10\mu m$). The breaking of the conventional diffraction limits can be understood in terms of the passage from the Helmholtz to the KG equation. In standard optics, expanding the optical electric field in its transverse Fourier components $\mathbf{E} = \int_{k_x,k_y}\mathbf{E}(k_x, k_y)\exp\left(ik_z z + ik_x x + ik_y y\right)$, the propagating waves

are bound to obey the relation that $k_x^2 + k_y^2 \leq k_0^2$, so that $\lambda/2$ constitutes the lower limit to spatial resolution (in air). In turn, this limit is absent in the KG regime, where the relative sign of the Laplacian term flips. We note that in the simplified paraxial case, both anti-diffraction of Eq. (7.18) and diffraction of Eq.(7.1) can be formally unified into a single description considering the effective permittivity $\epsilon_{\mathrm{m}} = \epsilon_r/(1 - \left(\frac{L}{\lambda}\right)^2)$, that reduces to the standard definition of the relative dielectric permittivity at optical frequencies $\epsilon_{\mathrm{m}} = \epsilon_r = n^2$ $(\mu = \mu_0)$ for $L \ll \lambda$. When $\epsilon_{\mathrm{m}} < 0$ beams do not have an "uncertainty" diffraction relation that fixes the minimum beam angular spread $\Delta\theta$ for a given beam size w_0 and the gaussian beam naturally converges. In distinction to linear response theory, ϵ_{m} is not the real part of a complex response function: it is a product of photorefraction and nonlinear beam propagation.

7.3.2   Sub-micrometer-sized propagating beams

Anti-diffraction of subwavelength beams is observed with setup and methods in close analogy with the non-paraxial scale-free and paraxial anti-diffraction experiments (section 7.1.2 and 7.2.2). Specifically, the peak value of L/λ depends on the thermal history of dipolar glass and is transient, so that when the appropriate shock is enacted, the KG regime emerges with its negative effective permittivity ϵ_{m}. The strong susceptibility and its associated large value of L/λ appears only if the thermal shocks are larger than a threshold amplitude ΔT. We launch a laser beam exiting a saturated high-aperture microscope objective, as reported in Fig. 7.7. The knife-edge super-resolution technique used to detect the non-paraxial beam width is illustrated in Fig. 7.7(a). After the thermal shock, a non-paraxial propagation emerges with the ultra-tight input $w_0 = 1.5\mu m$ spot (Fig.7.7(b)) shrinking to $1.3\mu m$ after a $3mm$ propagation (Fig. 7.7(c)), amounting to 134 diffraction (Rayleigh) lengths. When no thermal shock is enacted, the beam engulfs the entire sample, illuminating it (Fig. 7.7(d)). In the anti-diffracting case, we observe the narrowest propagating visible light beam hereto reported. To violate the limits of diffractive optics on spot size during propagation, we experimented with even narrower input launch beams using a fully illuminated long-working-distance dry objective ($NA = 0.8$). As reported in Fig. 7.8, the subwavelength beam input of $0.49\mu m$ shrinks to $0.28\mu m$ as it leaves the sample output facet, below the $\lambda/2 = (0.633/2)\mu m = 0.32\mu m$ limit, but still above the limit where the KG equation breaks down at $w_0 \simeq 0.1\mu m$, for $L/\lambda \simeq 1.1$ (Eq. (7.18)). For the $L_z \simeq 3mm$ distance, $w_0 = 0.49$ μm, $n = 2.2$, at $\lambda = 0.633\mu m$, this corresponds to approximately 1150 Rayleigh lengths of propagation, where the Rayleigh length $L_D = nw_0^2\pi/\lambda \simeq 2.62\mu m$. These beam obeys to the KG equation, so that light spots shrink as they propagate, irrespective of their intensity [89]. In distinction to previously demonstrated subwavelength focusing [205], this occurs for a propagation up to several millimeters, with a strong violation of the width/depth-of-focus constraint of diffractive optics. To place our study in context, we note that the laws of optical propagation are also strongly modified to lead to anti-diffractive regimes in nano-fabricated metamaterials [213, 101, 251, 227]. In comparison, our solution does not fundamentally involve wavelength-selectivity, directionality, resonances and absorption.
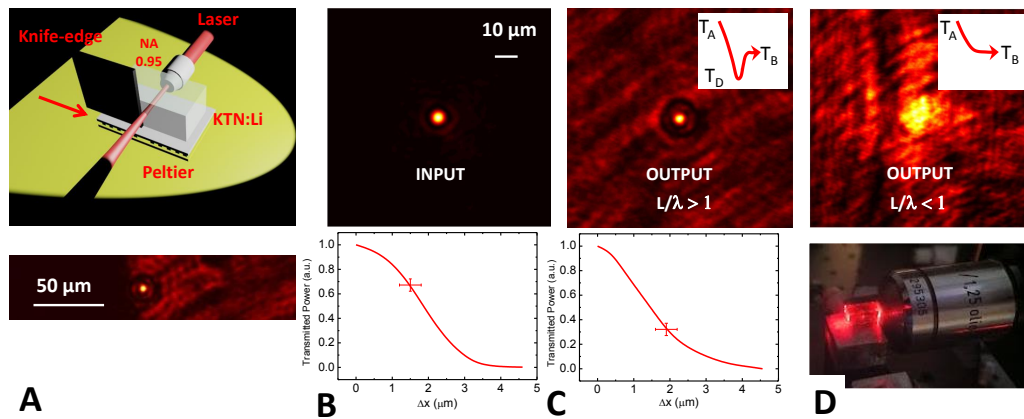
Figure 7.7. Micron-sized anti-diffractive light beams. (a) Schematic of experimental setup and image of transmitted light with the knife-edge in proximity of the output beam, showing the effect (an illuminated background) of the knife-edge that is placed directly onto the output crystal facet (at a distance below the diffraction length estimate $\simeq 22\mu m$). (b) (Top) Input intensity distribution as collected by the on axis CCD camera through the collecting lens (NA$\simeq$0.35) and (Bottom) high-resolution detection of the input beam size through the knife-edge technique that provides an input width of $1.5\mu m$. (c) Output beam characterization after an above-threshold thermal shock at the operating temperature T_B ($L/\lambda > 1$): (Top) transverse intensity distribution and (Bottom) the super-resolved output intensity spot of $1.3\mu m$. Note the difference in the shape tails of the detected beam, as also testified by the behavior in the knife-edge data, compared to the input. (d) Output for $L/\lambda \ll 1$: (Top) output intensity distribution and (Bottom) photograph of the crystal showing how the beam can fill the entire sample as it diffracts (From [89]).
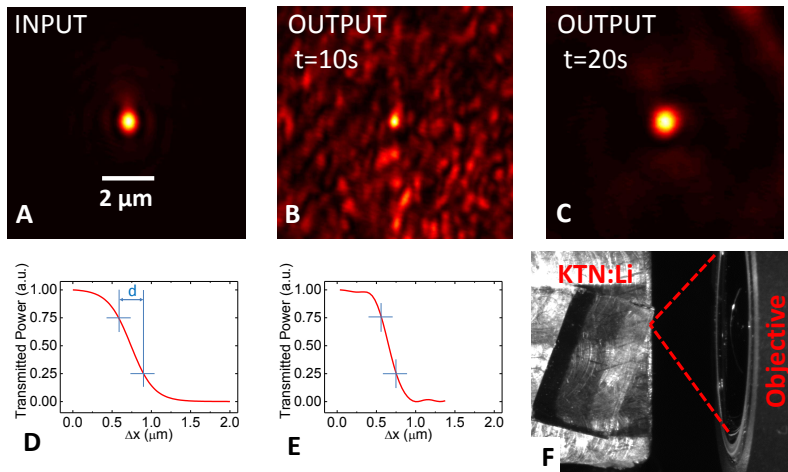
Figure 7.8. Reaching below the limits of diffractive optics. (a) Input beam intensity distribution of width $0.49\mu m$ that (b) shrinks to $0.28\mu m$ at the output facet and (c) begins relaxing to once again weakly diffracting spot as time passes. (d) Super-resolved knife-edge calibration of the input and (e) output beam. Crosshairs serve to identify the 0.75 and 0.25 transmitted power ratios, so that $w_0 = \sqrt{2}d$. (f) Top-view image of the long-working distance objective and KLTN sample. (From [89]).

Chapter 8

Negative mass dynamics from nonlinearity

Anti-diffracting beams are investigated in the presence of an optical potential well. With this study we propose and provide experimental evidence of a mechanism able to support negative intrinsic effective mass [94]. In fact, exploiting the change of the sign in the leading propagation equation discussed in Chapter 7, we report intrinsic negative mass dynamics for light beams in a ferroelectric crystal waveguide, where the diffusive photorefractive nonlinearity leads to a negative-mass Schrödinger Equation. The signature of inverted dynamics is the observation of beams repelled from strongly the guiding integrated structure irrespective of wavelength, specific direction or energy, thus suggesting shape-sensitive nonlinearity as a basic mechanism leading to intrinsic negative mass.

8.1 Negative-mass Schrödinger equation

Negative mass particles should be repelled from attractive potentials and attracted from repelling ones. With a mass $m < 0$, the particle subject to a potential U suffers a force $F = -\nabla U$ but manifests the inverted acceleration $a = \nabla U/|m|$ (Fig. 8.1). Although all known particles have a positive or zero mass, conditions can be found in which the interaction of a particle with its environment leads to an effective mass $m^* \neq m$ that can, in precise conditions, also be negative. To date, $m^* < 0$ has been demonstrated in periodic systems [171, 238, 303, 29, 105, 255], where the periodicity in the $\epsilon(k)$ band structure causes there to be a finite region of wave-vectors for which the Bloch-modes have a constant negative $d^2\epsilon/dk^2 < 0$ and with it, a behavior described by a negative effective mass $m^* = \hbar^2(d^2\epsilon/dk^2)^{-1} < 0$. Intuitively, internal components move out-of-phase with respect to the global resonance of the system and lead to a negative momentum response for a positive-momentum excitation [297]. Negative mass in these periodic systems is not intrinsic to the particle or wave, but only occurs for precise wavevectors at the edge of the Brillouin zone. It is important to note that, at present, no mechanism has been proposed and demonstrated able to support negative mass as a property of a localized wave with inverted dynamics irrespective of particle energy or wavevector.
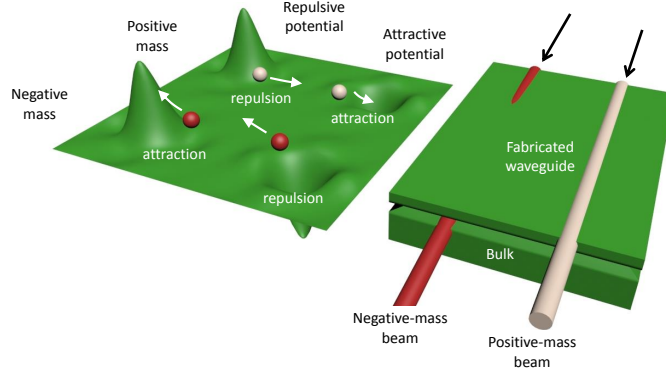
Figure 8.1. Intrinsic inverted dynamics and a negative-mass Schrödinger Equation (SE).
(Left) In contrast to a positive mass particle (lightly-shaded sphere), a negative mass
particle (dark sphere) will be attracted by a repelling potential and repelled by a binding
one. (Right) A propagating light beam described by a positive-mass SE (bright beam)
will be guided by an integrated waveguide whereas a negative-mass light beam (dark
beam) will be repelled by it and scattered into the bulk of the substrate. (From [94]).

Consider the Schrödinger equation (SE)

$$(i\partial_t + (\hbar/2m)\nabla^2)\psi = (V/\hbar)\psi, \tag{8.1}$$

where $m > 0$. As an axiom, the SE is linear, but assume that there is some
mechanism that violates this linearity so that, in general, the potential has two
components, $V + V_{nl}$, with V just a standard potential and V_{nl} a specific form of
self-action. Indeed, although nonlinearity is absent in quantum mechanics, it is
naturally built into the Einstein equations for which negative mass may have some
important role. If V_{nl} is a small local perturbation associated to $|\psi|^2$, such as a Kerr
effect with $V_{nl} \propto |\psi|^2$, the SE turns into a Nonlinear Schrodinger Equation (NLSE)
for which no negative mass dynamics emerges. Nonlinearity, in turn, can take many
forms and also be nonlocal, involving integrals and derivatives of $|\psi|^2$. If self-action
is approximated by $V_{nl}\psi \simeq (\hbar/2m')\nabla^2\psi$, then this will radically transform Eq. (8.1)
into

$$(i\partial_t + (\hbar/2m^*)\nabla^2)\psi = (V/\hbar)\psi, \tag{8.2}$$

that, when $m' < m$, corresponds to a negative mass SE with $m^* = mm'/(m'-m) < 0$.
On the other hand, the paraxial wave equation

$$(i\partial_z + (1/2k)\nabla_\perp^2)A = -(k\Delta n/n)A, \tag{8.3}$$

maps into the (2+1)D version of the SE of Eq. (8.1) for $t \equiv z/c$, $\psi \equiv A$, $m^* \equiv \hbar k/c$
and $V \equiv -\hbar c(k\Delta n/n)$. Hence, the causal relationship between the index of refraction
pattern and the paraxial propagation of a light beam is equivalent to that of a
particle with finite energy in an appropriate potential. In other words, although
photons have no mass, the description of a light field inside an inhomogeneous
transparent material naturally leads to the introduction of $m^* \neq 0$. In the present
case, the index modulation has two distinct components, $\Delta n = \delta n_{nl} + \delta n$, where
δn_{nl} is the diffusive nonlinear response caused by the propagating light, and $\delta n(\mathbf{r})$
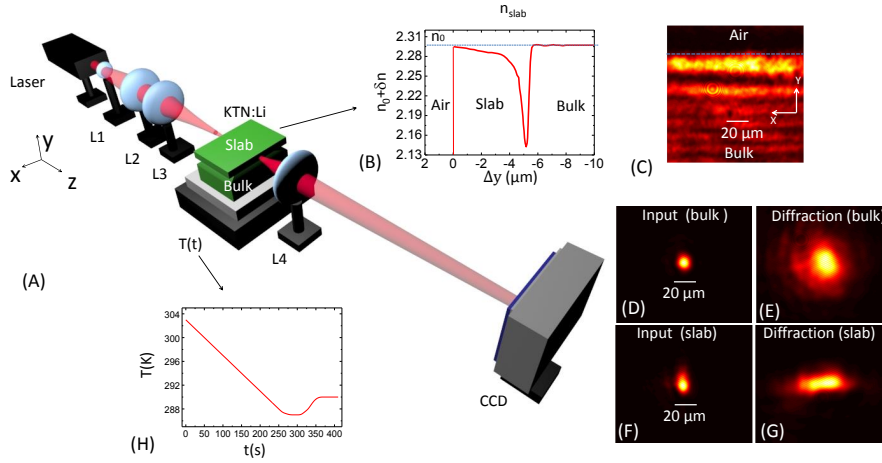
Figure 8.2. Nonlinear beam dynamics in a slab waveguide: experimental setup, materials and protocol. (a) A laser beam is launched into the KLTN waveguide and imaged on a CCD using lenses L1-L4 (L4 has NA$\simeq 0.35$). (b) Waveguide index profile for $532nm$. (c) Typical graded waveguide output intensity distribution for an expanded plane-wave input. (d-g) Input and diffraction intensity distribution pattern in the bulk crystal and in the waveguide ($L/\lambda \simeq 0$). At a constant $T_A = 303K$, the $100\mu W$ input beam (waist $w_{0x} \sim w_{0y} = 8\mu m$) (d) diffracts to $22\mu m$ (e) after propagating a distance of $L_z \simeq 2.4mm$ through the bulk crystal. In the waveguide, the input beam (f) diffracts to $w_{0x} = 9.8$ and $w_{0y} = 31.7\mu m$ (g). (h) Supercooling protocol $T(t)$ to achieve $L/\lambda > 1$. (From [94]).

is the index modulation of the fabricated slab waveguide acting as a fixed potential well. The propagation equation reads

$$\left(i\partial_z + \frac{1}{2k}\nabla_\perp^2\right) A = -\frac{k\delta n}{n_0}A + \frac{1}{2k}\frac{L^2}{4\lambda^2}\left(\frac{\nabla_\perp I}{I}\right)^2 A, \tag{8.4}$$

where $L = 4\pi n^2\epsilon_0\sqrt{g}\chi_{PNR}(k_BT/q)$, that, for gaussian-like beams, is well approximated by the linear wave equation

$$(i\partial_z + (1/2k)(1 - L^2/\lambda^2)\nabla_\perp^2)A = -(k\delta n/n)A. \tag{8.5}$$

For $L > \lambda$ Eq. (8.5) maps to the (2+1)D version of the SE of Eq. (8.2) with

$$m^* = -\frac{\hbar k}{c}\frac{1}{\frac{L^2}{\lambda^2} - 1} < 0. \tag{8.6}$$

The $m^* < 0$ regime is here a product of nonlinearity, is localized around the beam, and is not limited to specific wavelengths, directions, or resonances of the system. We note that the passage from the nonlinear Eq. (8.4) to the linear Eq. (8.5) is rigorously valid only for gaussian beams for which the peak intensity factors out of the term ($\nabla_\perp I/I$). Consistently, even though beams may be spreading or becoming tighter during propagation, they will have only one specific value of m^* (as per Eq. (8.6)). Since the passage to Eq. (8.5) is valid for gaussian beam shapes, it follows that the effective negative mass will arise only if the δn is comparable or larger to

the gaussian beam itself. Fabricated waveguides considerably smaller than the beam waist will correspond to a potential well as in Fig. 8.1 that is smaller than the size of the particle itself and not necessarily lead to inverted dynamics. A flag to this spatial requirement is that Eq. (8.4) is spatially nonlocal whereas Eq. (8.5) is not.

8.2 Observation of inverted light dynamics

8.2.1 Experiments in a ferroelectric slab waveguide

We carry out experiments with the setup illustrated in Fig. 8.2(a). An x-polarized TEM$_{00}$ beam from a He-Ne laser with ($\lambda_1 = 633nm$) or from a doubled Nd:YAG laser ($\lambda_2 = 532nm$) is first expanded and subsequently focused down onto the input facet of a sample of potassium-lithium-tantalate-niobate doped with copper (KLTN:Cu) crystal with a layer of He$^+$ ions implanted beneath its surface. Its composition is determined by electron micro-probe analysis and is found to be K$_{0.985}$Li$_{0.015}$Ta$_{0.63}$Nb$_{0.37}$O$_3$. The copper concentration is determined by Inductively Coupled Plasma (ICP) mass spectrometry and is found to be $68ppm$ (in weight). A sample of $3.9^{(x)} \times 0.9^{(y)} \times 2.4^{(z)}$ mm^3 in size is cut along the [001] crystallographic axis. The ferroelectric phase transition of the sample is derived from dielectric measurements, and is found to be at $T_C = 285K$. At the operating temperature range of $286K - 305K$ the sample maintains high optical quality with refractive index of $n = 2.3$, and quadratic electro-optic coefficient $g = 0.14m^4C^{-2}$. The He$^+$ ions are implanted at $2.3MeV$ with fluence of $0.8 \cdot 10^{16}ions/cm^2$ which yields a partially amorphous layer with refractive index distribution as presented in Fig. 8.2(b) [127]. This forms a slab waveguide between the surface of the sample and the implanted layer that acts as the cladding [126]. The transverse intensity distribution of the beam is imaged using a CCD camera through the imaging lens. The diffraction pattern at the output facet of the crystal $L/\lambda \simeq 0$, in the bulk and in the slab waveguide respectively, is shown in Fig. 8.2(d-g). In Fig. 8.2(h) we report the thermal shock protocol $T(t)$ near the peak in the dielectric response at $T_m = 287.5K$ that allows a transient $L/\lambda > 1$. The sample is cooled from $T_A = 303K$ at the rate of $0.06K/s$ to a temperature $T_D = 287K$ and it is then reheated at a rate of $0.1K/s$ to the operating temperature ($> T_D$) $T_B = 290K$. Once T_B is reached and the temperature cycle $T(t)$ is complete, we switch on the laser beam, recording front view images of the intensity distribution.

In Fig. 8.3(a) we report the basic signature of intrinsic negative mass SE dynamics: a beam expelled from the fabricated waveguide and scattered into the substrate. The beam is launched into the waveguide at $t = 0$ after the sample has undergone supercooling (the $T(t)$ in Fig. 8.2(h)). It is first observed to focus down, anti-diffract, and then suffer a strong repulsion, when it is scattered into the metastable bulk. Ultimately, the beam is observed to relax back into a linear diffraction, diffracting in the x-direction and guided in the y. The sequence of events is further detailed in Fig. 8.3(b), where the beam peak intensity is plotted versus time. For comparison, we include the same curve when the same beam is launched into the bulk of the substrate. In the slab the beam suffers a transient scattering, whereas in the bulk it suffers anti-diffraction dynamics. The connection between this transient repulsion from the waveguide and the change in sign of the
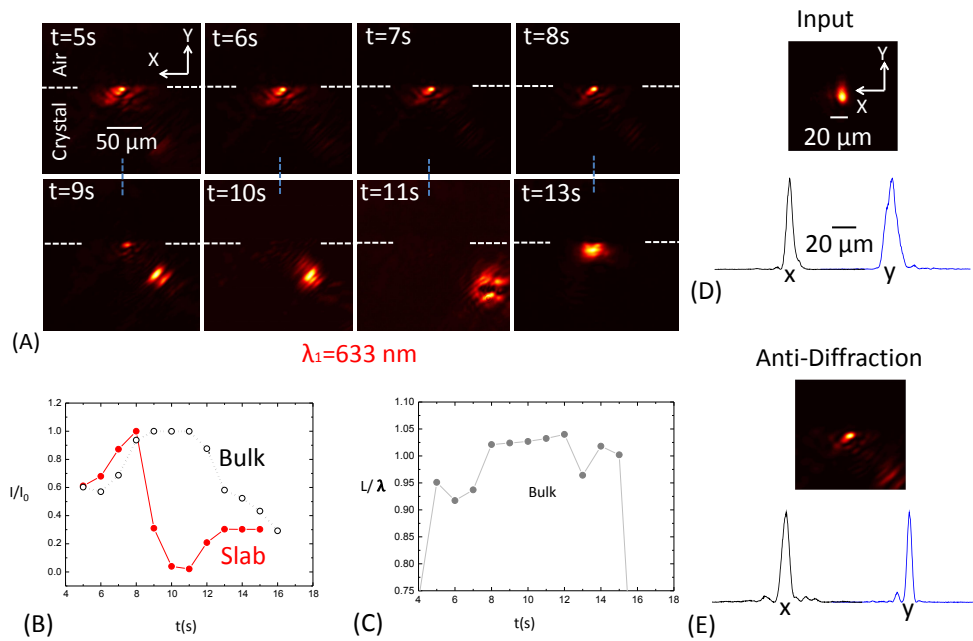
Figure 8.3. Observation of inverted dynamics: a fabricated waveguide repels light as it acquires an intrinsic negative mass. (a) Time sequence of the output intensity distributions for $\lambda_1 = 633nm$. (b) Comparison between the maximum peak intensity of the beam in the waveguide and in the bulk during the transient. (c) Time dependence of the L/λ in bulk. (d-e) Transient anti-diffraction in the waveguide: the input beam (waist $w_{0x} = 9.9\mu m$, $w_{0y} = 9.3\mu m$) (d) and the output beam (minimum $w_{0x} = 6.8\mu m$, $w_{0y} = 7.1\mu m$, $L/\lambda \simeq 1.05$) during the aftershock (e).(From [94]).

beam mass in the equivalent SE is investigated in Fig. 8.3(c). Using the bulk anti-diffraction and the analytical anti-diffraction theory, L/λ as a function of time is evaluated. As expected, the instants of time during which the dipolar relaxation leads to $L/\lambda > 1$ coincide with the repulsive regime. In other words, the behavior of the light beam is drastically different between the guided and bulk conditions, as shown in Fig. 8.3(b), in one case leading to a strong repulsion and scattering, in the other to strong spatial localization. The intensity distribution of input and anti-diffracting light corresponding to the $L/\lambda > 1$ stage before light is repelled by the waveguide is reported in Fig. 8.3(b-e). To validate the negative mass SE model of Eq. (8.5) we repeated experiments for different intensities. The strong transient response reported in Figs. 8.3 and 8.4 has a characteristic response time of tens of seconds. Experiments using beams with different powers $(10, 20, 40, 80, 100\mu W)$ lead to similar results and time scales. This approximate intensity-independent nature of the phenomenon is compatible with the overall effective linear nature of the effect as described in Eq. (8.2). Weak dependence of time scales on peak intensity indicates that even in this case time dynamics are principally associated to the relaxation of the metastable state of the material, while the photorefractive build-up is relatively faster and the space-charge field can be considered at all times at steady state. The value of the L parameter is always estimated by measuring the output and input waist ratio. To prove the effect is not limited to a specific region of wavevectors, in
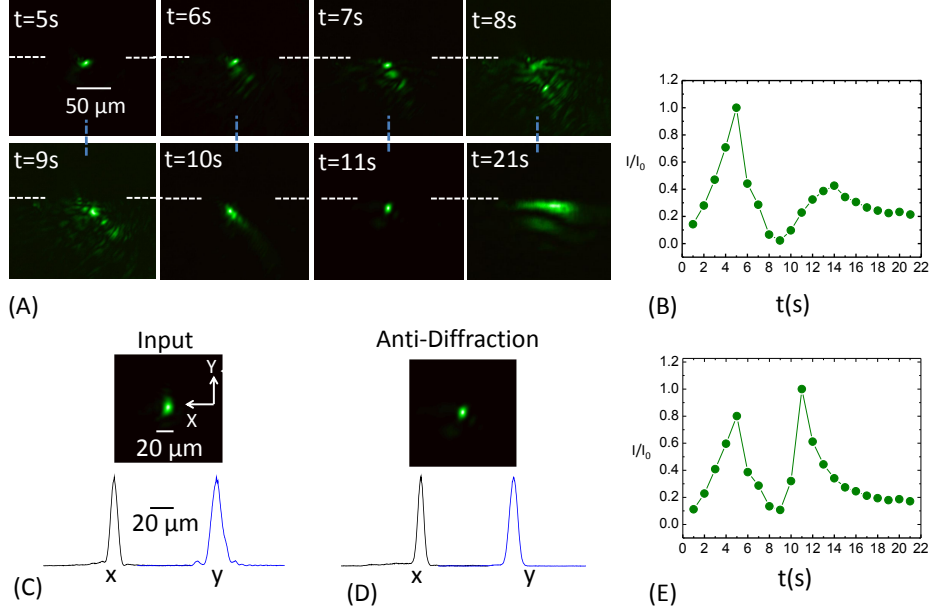
Figure 8.4. Negative mass dynamics for $\lambda_2 = 532nm$. (a) Time sequence of the output intensity distribution. (b) Maximum beam peak intensity in the waveguide during the transient. (c-d) Anti-diffraction in the waveguide: (c) the input beam (waist $w_{0x} = 6.8\mu m$, $w_{0y} = 9.9\mu m$) and (d) the output beam during the aftershock (minimum beam width $w_{0x} = 7.1\mu m$, $w_{0y} = 5.6\mu m$, $L/\lambda \simeq 1.04$). (e) Maximum beam peak intensity of the output beam during the transient. (From [94]).

Fig. 8.4 we report beam repulsion for $\lambda = 532nm$. The effect is analogous to the previous one, even though the details of the time evolution vary for each thermal shock, and only an average relaxation has a precise dynamical meaning. Specifically, the estimated value of L/λ for the two cases is comparable even though the thermal shock is the same and the wavelengths are different. Fluctuations are further exalted during the transition from the diffractive positive mass SE to the anti-diffractive negative mass SE, as the waveguide goes from being guiding to anti-guiding and allows light to explore its surroundings. An interesting difference in the dynamics of Fig. 8.3 and Fig. 8.4 is that the shorter wavelength case manifests a second focused stage reported in Fig. 8.4(e), displaced outside the original waveguide, where no second peak is found (Fig. 8.4(b)). Precisely, the second peak is displaced approximately $4\mu m$ in the y-direction, inside the amorphous region (see Fig. 8.4(b)). This may indicates that the antiguiding amorphous layer becomes guiding in the negative effective mass regime. Unfortunately, the amorphous layer is only $\simeq 1\mu m$ wide and its effect on the beam cannot be fully described by the passage from Eq. (8.4) to Eq. (8.5). Congruently, for the longer wavelength cases, no analogous effect is observed.

8.2.2 Numerical results

Numerical simulations of the stationary full-nonlinear Eq. 8.4 are performed to validate the effective linear SE behavior and the experimentally observed negative
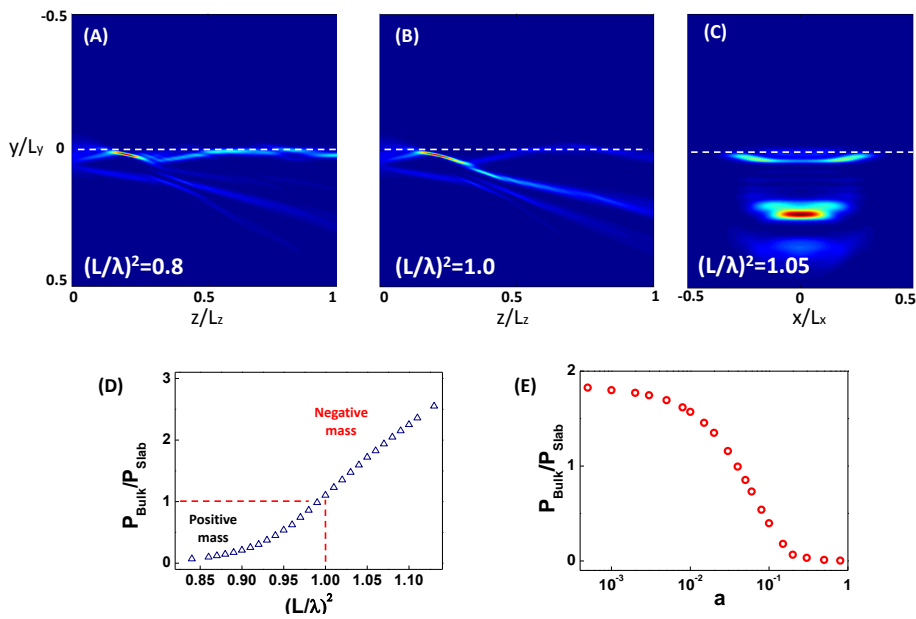
Figure 8.5. Inverted dynamics numerically simulated using the fully-nonlinear model (Eq. (8.4)). Dynamics of the beam along z ($L_x = 80\mu m$, $L_z = 2.4mm$, $\lambda = 633nm$) (a) for $(L/\lambda)^2 = 0.85$ and (b) $(L/\lambda)^2 = 1.05$. (c) Output intensity distribution in the negative effective mass case. (d) Ratio of total power scattered into the bulk P_{Bulk} to that retained by the slab P_{Slab} versus $(L/\lambda)^2$. An effective positive mass is compatible with $P_{Bulk}/P_{Slab} < 1$, whereas a negative mass is compatible with inverted dynamics and $P_{Bulk}/P_{Slab} > 1$. (e) Dependence of inverted dynamics on beam shape: the P_{Bulk}/P_{Slab} ratio for ever more distorted and squared-off gaussian inputs ($\exp\left[-(x^2 + y^2)/w_0^2\right] - a(x^4 + y^4)/w_0^4]$, w_0 is the input beam width), showing the breakdown of the effective linear Eq. 8.5 for squared field distributions. (From [94]).

mass dynamics. We use a split-step Fourier method with parameters matching our experimental conditions and the slab-waveguide profile. To avoid discontinuities of the linear refractive index, the interface air/crystal is slightly softened in the numerical modelling. Results well agree with our observations and are reported in Fig. 8.5. They allow us to inspect the details of the propagation during evolution (Fig. 8.5(a-d)) that cannot be directly detected optically and the resilience of the effect on distortions in the input gaussian beam shape (Fig. 8.5(e)). In particular, a continuous transition from positive to negative-mass dynamics is reproduced as a function of (L/λ), with the expulsion of the beam from the waveguide to the substrate for $(L/\lambda) > 1$ that well fits experimental observation. We note that this expulsion is fundamentally different respect to the phenomenon of soliton ejection and tunneling from a potential, where the refractive-index well is modified by the nonlinear dynamics [169, 26, 212]. In our present phenomenon, no available nonlinearity could even marginally modify the huge fabricated index modulation (index modulations up to $\delta n \simeq 0.15$), and expulsion is a consequence of a change in the sign of the effective-mass of the light beam. A similar negative-mass SE has been recently predicted in hyperbolic materials as a result of hyperbolic dispersion [16].

Conclusions

We have reported several new phenomena in nonlinear optics arising from the interplay of disordered ferroelectrics and nonlinear wave propagation. In particular, exploiting the unique photorefractive properties of critical states in proximity of the ferroelectric phase transition, we have opened important routes to study spatial dynamics of optical waves in regimes ruled by instabilities and stochastic features. The appearance of abnormal waves, an open issue common to different noisy nonlinear systems from hydrodynamics to acoustics, has been experimentally discovered in spatial wave propagation in optical crystals. A deep investigation of the phenomenon, aimed at clarifying extreme waveform properties and the role of scales in their formation, have allowed us to understand the origin of rogue waves in our system in terms of chaotic spatiotemporal soliton dynamics in saturable nonlinearities. This dynamics is observed as the unstable optical flow undergoes a transition to optical turbulence, corresponding to loss of coherence of the propagating field. In this respect, our results introduces a new and rich experimental setting for the study of wave turbulence in conditions dominated by large fluctuations and extreme nonlinearity. Using extreme material responses, we demonstrate how a giant diffusive photorefractive nonlinearity can lead to the overcoming of the diffractive limit of waves, with diffraction cancellation and anti-diffraction of light up to subwavelength propagation regimes. These results, closely connected to effects typical of metamaterials, profoundly impact imaging and super-resolution techniques and allow experimental access to fundamental physical problems. In fact, we discover how nonlinearity can modify the nature of the underlying wave equation leading to a negative mass dynamics, where the optical wavefunction escapes from a trapping potential independently of its wavevector and energy. These findings have been accompanied by electro-optical results shedding new light on the condensed matter physics of disordered perovskites, such as properties of their ferroelectric phase-transition, complex dielectric relaxation and dipolar states. We have reported an anomalous electro-optic effect having its signature in local symmetry-breaking and, above all, the observation a new ordered ferroelectric phase characterized by polar domains forming spontaneously a coherent and macroscopic crystalline structure. Our results further point out how the meeting between nonlinear optical waves and disordered ferroelectric represent a system that, together with the possibility of new optical and electronics technological functionalities, includes fundamental and general physics yet to be explored from optics, nonlinear dynamics and condensed matter to many other research fields.

References

[1] H.D.I.Abarbanel, R.Brown, J.J.Sidorowich and L.S.Tsimring, The analysis of observed chaotic data in physical systems, *Rev. Mod. Phys.* **65**, 1331 (1993).

[2] M.J.Ablowitz and H.Segur, *Solitons and the Inverse Scattering Transform*, SIAM Philadelphia, 1981.

[3] M.J.Ablowitz and P.A.Clarkson, *Solitons, nonlinear evolution equations and Inverse Scattering*, London Math. Society Lecture Note Series, vol. 194, Cambridge University Press, Cambridge, 1991.

[4] T.A.Adcock and P.H.Taylor, The physics of anomalous ('rogue') ocean waves, *Rep. Prog. Phys.* **77**, 105901 (2014).

[5] D.S.Agafontsev and V.E.Zakharov, Integrable turbulence and formation of rogue waves, *Nonlinearity* **28**, 2791 (2015).

[6] A. Agranat, R.Hofmeister, and A.Yariv, Characterization of a new photorefractive material: Kl-yLyT 1-xNx, *Opt. Lett.* **17**, 713 (1992).

[7] A.J.Agranat, R.Kaner, G.Perpelitsa and Y.Garcia, Stable electro-optic striation grating produced by programmed periodic modulation of the growth temperature, *Appl. Phys. Lett.* **90**, 192902 (2007).

[8] A.J.Agranat, C.E.M.deOliveira and G.Orr, Dielectric electrooptic gratings in potassium lithium tantalate niobate, *J. Non-Cryst. Sol.* **353**, 4405 (2007).

[9] G.P.Agrawal,*Nonlinear fiber optics*, Academic press, 2007.

[10] M.Ahart *et al.*, Origin of morphotropic phase boundaries in ferroelectrics, *Nature* **451**, 545 (2008).

[11] A.R.Akbarzadeh, S.Prosandeev, E.J.Walter, A.Al-Barakaty, and L.Bellaiche, Finite-temperature properties of Ba(Zr,Ti)O3 relaxors from first principles, *Phys. Rev. Lett.* **108**, 257601 (2012).

[12] N.Akhmediev, A.Ankiewicz, and M.Taki, Waves that appear from nowhere and disappear without a trace, *Phys. Lett. A* **373**, 675 (2009).

[13] N.Akhmediev *et al.*, Roadmap on optical rogue waves and extreme events, *J. Opt.* **18**, 063001 (2016).

[14] M.R.Alam, Predictability horizon of oceanic rogue waves, *Geophysical Research Letters* **41**, 8477 (2015).

[15] F.Alberici-Kious, J.P.Bouchaud, L.F.Cugliandolo, P.Doussineau, A.Levelut, Aging in $K_{1-x}Li_xTaO_3$: A Domain Growth Interpretation, *Phys. Rev. Lett.* **81**, 4987 (1998).

[16] A.Alberucci, C.P.Jisha, A.D.Boardman, and G.Assanto, Anomalous diffraction in hyperbolic materials, *Phys. Rev. A* **94**, 033830 (2016).

[17] S.Y.Annenkov and V.I.Shrira, On the predictability of evolution of surface gravity and gravity capillary waves, *Physica D* **152**, 665 (2001).

[18] A.Aragoneses, L.Carpi, N.Tarasov, D.V.Churkin, M.C.Torrent, C.Masoller, and S.K.Turitsyn, Unveiling Temporal Correlations Characteristic of a Phase Transition in the Output Intensity of a Fiber Laser, *Phys. Rev. Lett.* **116**, 033902 (2016).

[19] F.T.Arecchi, U.Bortolozzo, A.Montina and S.Residori, Granularity and Inhomogeneity Are the Joint Generators of Optical RogueWaves, *Phys. Rev. Lett.* **106**, 153901 (2011).

[20] A.Armaroli, C.Conti and F.Biancalana, Rogue solitons in optical fibers: a dynamical process in a complex energy landscape?, *Optica* **2**, 497 (2015).

[21] A.Ashkin, G.D.Boyd, J.M.Dziedric, R.G.Smith, A.A.Ballman, J.J.Levinstein, K.Nassau, Optically-induced refractive index inhomogeneities in LiNbO3 and LiTaO3, *Appl. Phys. Lett.* **9**, 72 (1966).

[22] E.Aurell, G.Boffetta, A.Crisanti, G.Paladin, and A.Vulpiani, Predictability in the large: an extension of the concept of Lyapunov exponent, *Journal of Physics A* **30**, 1 (1997).

[23] K.Avila, D.Moxey, A.de Lozar, M.Avila, D.Barkley and B.Hof, The onset of turbulence in pipe flow, *Science* **333**, 192-196 (2011).

[24] M.Ayoub, J.Imbrock, and C.Denz, Second harmonic generation in multi-domain $\chi 2$ media: from disorder to order, *Opt. Express* **19**, 11340 (2011).

[25] V.Baledent, S.Chattopadhyay, P.Fertey, M.B.Lepetit, M.Greenblatt, B.Wanklyn, F.O.Saouma, J.I.Jang and P.Foury-Leylekian, Evidence for Room Temperature Electric Polarization in RMn2O5 Multiferroics, *Phys. Rev. Lett.* **114**, 117601 (2015).

[26] A.Barak, O.Peleg, C.Stucchio, A.Soffer, and M.Segev, Observation of soliton tunneling phenomena and soliton ejection, *Phys. Rev. Lett.* **100**, 153901 (2008).

[27] F.Baronio, A.Degasperis, M.Conforti, and S.Wabnitz, Solutions of the vector nonlinear Schrdinger equations: evidence for deterministic rogue waves, *Phys. Rev. Lett.* **109**, 044102 (2012).

[28] C.Barsi and J.W.Fleischer, Nonlinear Abbe theory, *Nat. Photon.***7**, 639 (2013).

[29] S.Batz and U.Peschel, Diametrically Driven Self-Accelerating Pulses in a Photonic Crystal Fiber, *Phys. Rev. Lett* **110**, 193901 (2013).

[30] M.Baudrier-Raybaut, R.Haidar, P.Kupecek, P.Lemasson, and E.Rosencher, Random quasi-phase-matching in bulk polycrystalline isotropic nonlinear materials, *Nature* **432**, 374 (2004).

[31] L.Bergamasco, M.Serio, A.R.Osborne, and L.Cavaleri, Finite Correlation Dimension and Positive Lyapunov Exponents for Surface Wave Data in the Adriatic Sea near Venice, *Fractals* **3**, 55 (1995).

[32] A.Biancoli, C.M.Fancher, J.L.Jones and D.Damjanovic, Breaking of macroscopic centric symmetric in paraelectric phases of ferroelectric materials and implications for flexoelectricity, *Nat. Mater.* **14**, 224 (2014).

[33] S.Birkholz, E.T.J.Nibbering, C.Bree, S.Skupin, A.Demircan, G.Genty and G.Steinmeyer, Spatiotemporal Rogue Events in Optical Multiple Filamentation, *Phys. Rev. Lett.* **111**, 243903 (2013).

[34] S.Birkholz, C.Bree, A.Demircan and G.Steinmeyer, Predictability of Rogue Events, *Phys. Rev. Lett.* **114**, 213901 (2015).

[35] A.Bitman, N.Sapiens, L.Secundo, A.J.Agranat, G.Bartal and M.Segev, Electroholographic tunable volume grating in the g 44 configuration, *Optics Lett.* **31**, 2849 (2006).

[36] G.Boffetta, M.Cencini, M.Falcioni, and A.Vulpiani, Predictability: a way to characterize complexity, *Physics reports* **356**, 367 (2002).

[37] A.A.Bokov and Z.G.Ye, Recent progress in relaxor ferroelectrics with perovskite structure, *J. Mater. Sci* **41**, 31 (2006).

[38] A.A. Bokov, Z.-G. Ye, Dielectrical relaxation in relaxor ferroelectrics, *J. Adv. Dielectrics* **2**, 1241010 (2012).

[39] C.Bonatto, M.Feyereisen, S.Barland, M.Giudici, C.Masoller, J.R.Rios Leite and J.R. Tredicce, Deterministic Optical RogueWaves, *Phys. Rev. Lett.* **107**, 053901 (2011).

[40] A.Y.Borisevich *et al.*, Atomic-scale evolution of modulated phases at the ferroelectric-cantiferroelectric morphotropic phase boundary controlled by flexoelectric interaction, *Nat. Commun.* **3**, 775 (2012).

[41] M. Born and E. Wolf, *Principles of Optics*, Pergamon, 6th ed., 1980.

[42] U.Bortolozzo, J.Laurie, S.Nazarenko and S.Residori, Optical wave turbulence and the condensation of light. *JOSA B* **26**, 2280 (2009).

[43] E.Bousquet, M.Dawber, N.Stucki, C.Lichtensteiger, P.Hermet, S.Gariglio, J.M.Triscone and P.Ghosez, Improper ferroelectricity in perovskite oxide artificial superlattices, *Nature* **452**, 732 (2008).

[44] R.W.Boyd, *Nonlinear Optics*, Academic Press, 2008.

[45] F.Boyer and E.Falcon, Wave turbulence on the surface of a ferrofluid in a magnetic field, *Phys. Rev. Lett.* **101**, 244502 (2008).

[46] C.Bree, G.Steinmeyer, I.Babushkin, U.Morgner, and A.Demircan, Controlling formation and suppression of fiber-optical rogue waves, *Opt. Lett.* **41**, 3515 (2016).

[47] Y.Bromberg, Y.Lahini, E.Small, and Y.Silberberg, Hanbury Brown and Twiss interferometry with interacting photons, *Nature Photon.* **4**, 721-726 (2010).

[48] N.Bulso and C.Conti, Effective dissipation and nonlocality induced by nonparaxiality, *Phys. Rev. A* **89**, 023804 (2014).

[49] G.Burns and F.H.Dacol, Crystalline ferroelectrics with glassy polarization behavior, *Phys. Rev. B* **28**, 2527 (1983).

[50] L.Cai, J.Toulouse, L.Harriger, R.G.Downing, and L.A.Boatner, Origin of the crossover between a freezing and a structural transition at low concentration in the relaxor ferroelectric K1-xLixTaO3, *Phys. Rev. B* **91**, 134106 (2015).

[51] S.J.Callori, J.Gabel, D.Su, J.Sinsheimer, M.V.Fernandez-Serra and M.Dawber, Ferroelectric PbTiO3/SrRuO3 Superlattices with Broken Inversion Symmetry, *Phys. Rev. Lett.* **109**, 067601 (2012).

[52] G.Catalan, A.Janssens, G.Rispens, S.Csiszar, O.Seeck, G.Rijnders, D.H.A.Blank and B.Noheda, Polar domains in lead titanate films under tensile strain, *Phys. Rev. Lett.* **96**, 127602 (2006).

[53] G.Catalan, A.Lubk, A.H.G.Vlooswijk, E.Snoeck, C.Magen, A.Janssens, G.Rispens, G.Rijnders, D.H.A.Blank and B.Noheda, Flexoelectric rotation of polarization in ferroelectric thin films, *Nat. Mater.* **10**, 963 (2011).

[54] M.Cencini, F.Cecconi, A.Vulpiani, *Chaos*, World Scientific, Series on Advances in Statistical Mechanics **17**, (2010).

[55] M.Cencini, M.Falcioni, E.Olbrich, H.Kantz, and A.Vulpiani, Chaos or noise: Difficulties of a distinction, *Phys. Rev. E* **62**, 427 (2000).

[56] Y-C.Chang, C.Wang, S.Yin, R.C.Hoffman, and A.G.Mott, Kovacs effect enhanced broadband large field of view electro-optic modulators in nanodisordered KTN crystals, *Opt. Express* **21**, 17760-17768 (2013).

[57] Y-C.Chang, C.Wang, S.Yin, R.C.Hoffman, and A.G.Mott, Giant electro-optic effect in nanodisordered KTN crystals, *Opt. Lett.* **38**, 4574-4577 (2013).

[58] L.Q.Chen, Phase-Field Method of Phase Transitions/Domain Structures in Ferroelectric Thin Films: A Review, *Journal of the American Ceramic Society* **91**, 1835 (2008).

[59] Z.G.Chen, M.H.Garrett, G.C.Valley, M.Mitchell, M.F.Shih, and M.Segev, Steady-state dark photorefractive screening solitons, *Opt. Lett.* **22**, 629 (1996).

[60] Z.G.Chen, M.Segev, D.N.Christodoulides, Optical spatial solitons: historical overview and recent advances, *Rep. Prog. Phys.* **75**, 086401 (2012).

[61] Z.Chen, M.Segev, and D.N.Christodoulides, Experiments on partially coherent photorefractive solitons, *J. Opt. A: Pure Appl. Opt.* **5**, S389 (2003).

[62] K.J.Choi, M.Biegalski, Y.L.Li, A.Sharan, J.Schubert, R.Uecker, P.Reiche, Y.B.Chen, X.Q.Pan, V.Gopalan, L.-Q.Chen, D.G.Schlom, C.B.Eom, Enhancement of Ferroelectricity in Strained BaTiO3 Thin Films, *Science* **306**, 1005 (2004).

[63] D.N.Christodoulides, T.H.Coskun, M.Mitchell, and M.Segev, Theory of incoherent self-focusing in biased photorefractive media. *Phys. Rev. Lett.* **71**, 646 (1997).

[64] D.N.Christodoulides and T.H.Coskun, Diffraction-free planar beams in unbiased photorefractive media, *Opt. Lett.* **21**, 1460 (1996).

[65] P.Chu, D.P.Chen, Y.L.Wang, Y.L.Xie, Z.B.Yan, J.G.Wan, J.-M.Liu and J.Y.Li, Kinetics of 90 domain wall motions and high frequency mesoscopic dielectric response in strained ferroelectrics: A phase-field simulation. *Scientific reports* **4**, (2014).

[66] D.V.Churkin, O.A.Gorbunov and S.V. Smirnov, Extreme value statistics in Raman fiber lasers, *Opt. Lett.* **36**, 3617 (2011).

[67] A.Ciattoni, C.Rizza, E.DelRe and E.Palange, Photorefractive solitons embedded in gratings in centrosymmetric crystals, *Opt. Lett.* **31**, 1690 (2006).

[68] A.Ciattoni, C.Rizza, E.DelRe, and A.Marini, Light-induced dielectric structures and enhanced self-focusing in critical photorefractive ferroelectrics, *Opt. Lett.* **34**, 3295 (2009).

[69] A.Clauset, C.R.Shalizi and M.E.Newman, Power-law distributions in empirical data, *SIAM review* **51**, 661 (2009).

[70] A.Coillet, J.Dudley, G.Genty, L.Larger and Y.K.Chembo, Optical rogue waves in whispering-gallery-mode resonators, *Phys. Rev. A* **89**, 013835 (2014).

[71] M.Conforti, A.Mussot, J.Fatome, A.Picozzi, S.Pitois, C.Finot, M.Haelterman, B.Kibler, C.Michel, and G.Millot, Turbulent dynamics of an incoherently pumped passive optical fiber cavity: Quasisolitons, dispersive waves, and extreme events, *Phys. Rev. A* **91**, 023823 (2015).

[72] C.Conti, A.Fratalocchi, M.Peccianti, G.Ruocco, and S.Trillo, Observation of a gradient catastrophe generating solitons, *Phys. Rev. Lett.* **102**, 083902 (2009).

[73] C.Conti, Complex light: Dynamic phase transitions of a light beam in a nonlinear nonlocal disordered medium, *Phys. Rev. E* **72**, 066620 (2005).

[74] C.Conti, A.J.Agranat, and E.DelRe, Subwavelength optical spatial solitons and three-dimensional localization in disordered ferroelectrics: Toward metamaterials of nonlinear origin, *Phys. Rev. A* **84**, 043809 (2011).

[75] B.Crosignani, A.Degasperis, E.DelRe, P.DiPorto, and A.J. Agranat, Nonlinear optical diffraction effects and solitons due to anisotropic charge-diffusion based self-interaction, *Phys. Rev. Lett.* **82**, 1664 (1999).

[76] C.Dari-Salisburgo, E.DelRe, and E.Palange, Molding and stretched evolution of optical solitons in cumulative nonlinearities, *Phys. Rev. Lett.* **91**, 263903 (2003).

[77] M.Dawber, K.M.Rabe and J.F.Scott, Physics of thin-film ferroelectric oxides, *Rev. Mod. Phys.* **77**, 1083 (2005).

[78] M.Dehghan and A. Taleei, A compact split-step finite difference method for solving the nonlinear Schrdinger equations with constant and variable coefficients, *Comput. Phys. Commun* **181**, 43 (2010).

[79] E.DelRe, B.Crosignani, M.Tamburrini, M.Segev, M.Mitchell, E.Refaeli, and A.J.Agranat, One-dimensional steady-state photorefractive spatial solitons in centrosymmetric paraelectric potassium lithium tantalate niobate, *Opt. Lett.* **23**, 421 (1998).

[80] E.DelRe, A.Ciattoni, B.Crosignani, and M.Tamburrini, Approach to space-charge field description in photorefractive crystals, *JOSA B* **15**, 1469 (1998).

[81] E.DelRe, M.Tamburrini, M.Segev, R.Della Pergola, and A.J. Agranat, Spontaneous self-trapping of optical beams in metastable paraelectric crystals, *Phys. Rev. Lett.* **83**, 1954 (1999).

[82] E.DelRe, A.DErcole, and A.J.Agranat, Emergence of linear wave segments and predictable traits in saturated nonlinear media, *Opt. Lett.* **28**, 260 (2003).

[83] E.DelRe, G.De Masi, A.Ciattoni and E.Palange, Pairing space-charge field conditions with self-guiding for the attainment of circular symmetry in photorefractive solitons, *Appl. Phys. Lett.* **85**, 5499 (2004).

[84] E.DelRe and E.Palange, Optical nonlinearity and existence conditions for quasi-steady-state photorefractive solitons, *JOSA B* **23**, 2323 (2006).

[85] E.DelRe, A.Ciattoni, and E.Palange, Role of charge saturation in photorefractive dynamics of micron-sized beams and departure from soliton behavior, *Phys. Rev. E* **73**, 017601 (2006).

[86] E.DelRe, B.Crosignani and P.Di Porto, Photorefractive Solitons and Their Underlying Nonlocal Physics, *Progress in Optics* **53**, 153 (2009).

[87] E.DelRe, A.DErcole, and E.Palange, Mechanisms supporting long propagation regimes of photorefractive solitons, *Phys. Rev. E* **71**, 036610 (2005).

[88] E.DelRe, E.Spinozzi, A.J.Agranat and C.Conti, Scale-free optics and diffractionless waves in nanodisordered ferroelectrics, *Nat. Photonics* **5**, 39 (2011).

[89] E.DelRe, F.Di Mei, J.Parravicini, GB.Parravicini, A.J.Agranat and C.Conti, Sub-wavelength anti-diffracting beams propagating over more than 1,000 Rayleigh lengths, *Nature Photon. Nature Photon.* **9**, 228 (2015).

[90] S.Derevyanko and E. Small, Nonlinear propagation of an optical speckle field, *Phys. Rev. A* **85**, 053816 (2012).

[91] A.De Rossi, S.Trillo, A.V.Buryak and Y.S.Kivshar, Symmetry-breaking instabilities of spatial parametric solitons, *Phys. Rev. E* **56**, R4959 (1997).

[92] F.Di Mei, D.Pierangeli, J.Parravicini, C.Conti, A.J.Agranat and E.DelRe, Observation of diffraction cancellation for nonparaxial beams in the scale-free-optics regime, *Phys. Rev. A* **92**, 013835 (2015).

[93] F.Di Mei, J.Parravicini, D.Pierangeli, C.Conti, A.J.Agranat and E.DelRe, Anti-diffracting beams through the diffusive optical nonlinearity, *Opt. Express* **22**, 31434 (2014).

[94] F.DiMei, P.Caramazza, D.Pierangeli, G.Di Domenico, H.Ilan, A.J.Agranat, P.Di Porto, and E.DelRe, Intrinsic negative mass from nonlinearity, *Phys. Rev. Lett.* **116**, 153902 (2016).

[95] J.M.Dudley, F.Dias, M.Erkintalo and G.Genty, Instabilities, breathers and rogue waves in optics, *Nat. Photonics* **8**, 775 (2014).

[96] J.M.Dudley, G.Genty and B.J.Eggleton, Harnessing and control of optical rogue waves in supercontinuum generation, *Opt. Express* **16**, 3644 (2008).

[97] G.C.Duree et al., Observation of self-trapping of an optical beam due to the photorefractive effect, *Phys. Rev. Lett.* **71**, 533 (1993).

[98] N.Efremidis, S.Sears, D.Christodoulides, J.Fleischer and M.Segev, Discrete solitons in photorefractive optically induced photonic lattices *Phys. Rev. E* **66**, 046602 (2002).

[99] H.S.Eisenberg, Y.Silberberg, R.Morandotti, A.R.Boyd, and J.S.Aitchison, iscrete Spatial Optical Solitons in Waveguide Arrays, *Phys. Rev. Lett.* **81**, 3383 (1998)

[100] H.S.Eisenberg, Y.Silberberg, R.Morandotti and J.S. Aitchison, Diffraction Management *Phys. Rev. Lett.* **85**, 1863 (2000).

[101] N.Fang, H.Lee, C.Sun, X.Zhang, Sub-diffraction-limited optical imaging with a silver superlens, *Science* **308**, 534 (2005).

[102] F.Fedele, J.Brennan,S.P.de Leen, J.Dudley and F.Dias, Real world ocean rogue waves explained without the modulational instability, *Sci. Rep.* **6**, 27715 (2016).

[103] G.Fibich, Y.Sivan and M.I.Weinstein, Bound states of nonlinear Schrodinger equations with a periodic nonlinear microstructure, *Physica D: Nonlinear Phenomena* **217**, 31 (2006).

[104] O.Firstenberg, P.London, M.Shuker, A.Ron, and N.Davidson, Elimination, reversal and directional bias of optical diffraction, *Nature Phys.* **5**, 665 (2009).

[105] O.Firstenberg, T.Peyronel, Q.Y. Liang, A.V.Gorshkov, M.D.Lukin, and V.Vuletic, Attractive photons in a quantum nonlinear medium, *Nature* **502**, 71 (2013).

[106] R.Fischer, S.M.Saltiel, D.N.Neshev, W.Krolikowski, and Yu.S.Kivshar, Broadband femtosecond frequency doubling in random media, *Appl. Phys. Lett.* **89**, 191105 (2006).

[107] R.A.Fisher and W. Bischel, The role of linear dispersion in plane-wave self-phase modulation, *Appl. Phys. Lett.* **23**, 661 (1973).

[108] J.Fleischer, G.Bartal, O.Cohen, T.Schwartz, O.Manela, B.Freedman, M.Sagev and N.Efremidis, Spatial photonics in nonlinear waveguide arrays, *Opt. Express* **13**, 1780 (2005).

[109] J.Fleischer, T.Carmon, M.Segev, N.Efremidis and D.Christodoulides, Observation of Discrete Solitons in Optically Induced Real Time Waveguide Arrays, *Phys. Rev. Lett.* **90**, 023902 (2003).

[110] V.Folli, E.DelRe, and C.Conti, Beam Instabilities in the Scale-Free Regime, *Phys. Rev. Lett.* **108**, 033901 (2012).

[111] N.Fressengeas, D.Wolfersberger, J.Maufoy, and G.Kugel, Build up mechanisms of (1+1)-dimensional photorefractive bright spatial quasi-steady-state and screening solitons, *Opt. Commun* **145**, 393 (1998).

[112] B.Frisquet, B.Kibler and G.Millot, Collision of Akhmediev Breathers in Nonlinear Fiber Optics, *Phys. Rev. X* **3**, 041032 (2013).

[113] R.A.Fuerst, D.M.Baboiu, B.Lawrence, W.E.Torruellas, G.I.Stegeman, S.Trillo and S.Wabnitz, Spatial modulational instability and multisolitonlike generation in a quadratically nonlinear optical medium, *Phys. Rev. Lett.* **78**, 2756 (1997).

[114] V.Garcia, S.Fusil, K.Bouzehouane, S.Enouz-Vedrenne, N.D.Mathur, A.Barthelemy and M.Bibes, Giant tunnel electroresistance for non-destructive readout of ferroelectric states, *Nature* **460**, 81 (2005).

[115] A.N.Ganshin, V.B.Efimov, G.V.Kolmakov, L.P.Mezhov-Deglin, and P.V.McClintock, Observation of an inverse energy cascade in developed acoustic turbulence in superfluid helium, *Phys. Rev. Lett.* **101**, 065303 (2008).

[116] S.Gentilini, M.C.Braidotti, G.Marcucci, E.DelRe, and C.Conti, Physical realization of the Glauber quantum oscillator, *Sci. Rep.* **5**, 15816 (2015).

[117] N.Ghofraniha, C.Conti, G.Ruocco, and S.Trillo, Shocks in nonlocal media, *Phys. Rev. Lett.* **99**, 043903 (2007).

[118] N.Ghofraniha, I.Viola, F.Di Maria, G.Barbarella, G.Gigli, L.Leuzzi, and C.Conti, Experimental evidence of replica symmetry breaking in random lasers, *Nat. Commun.* **6**, 6058 (2015).

[119] J.W.Goodman, *Statistical properties of laser speckle patterns*, Springer Berlin Heidelberg, (1975)

[120] A.S.L.Gomes *et al.*, Glassy behavior in a one-dimensional continuous-wave erbium-doped random fiber laser, *Phys. Rev. A* **94**, 011801(R) (2016).

[121] H.Guo, X.Liu, F.Xue, L.Q.Chen, W.Hong, and X.Tan, Disrupting long-range polar order with an electric field, *Phys. Rev. B* **93**, 174114 (2016).

[122] M.D.Glinchuk, E.A.Eliseev, and A.N.Morozovska, Superparaelectric phase in the ensemble of noninteracting ferroelectric nanoparticles, *Phys. Rev. B* **78**, 134107 (2008).

[123] N.M.Granese, A.Lacapmesure, M.B.Aguero, M.G.Kovalsky, A.A.Hnilo, and J.R.Tredicce, Extreme events and crises observed in an all-solid-state laser with modulation of losses, *Opt. Lett.* **41**, 3010 (2016).

[124] P.Grassberger and I.Procaccia, Characterization of Strange Attractors, *Phys. Rev. Lett.* **50**, 346 (1983).

[125] S.Grossmann, The onset of shear flow turbulence, *Rev. Mod. Phys.* **72**, 603b (2000).

[126] A.Gumennik, A.J.Agranat, I.Shachar, and M.Hass, Thermal stability of a slab waveguide implemented by α particles implantation in KLTN, *Appl. Phys. Lett.* **87**, 251917 (2005).

[127] A.Gumennik, G.Perepelitsa, A.Israel and A.J.Agranat, A tunable channel waveguide array fabricated by the implantations of He+ ions in an electrooptical KLTN substrate, *Opt. Express* **17**, 6166 (2009).

[128] A.Gumennik, Y.Kurzweil-Segev, and A.J.Agranat, Electrooptical effects in glass forming liquids of dipolar nano-clusters embedded in a paraelectric environment, *Opt. Mat. Express* **1**, 332 (2011).

[129] P.Günter and J.P. Hiugnard, *Photorefractive Materials and Their Application 1,* Springer, 2006.

[130] M. Haahr, *True Random Number Service*, https://www.random.org .

[131] A.Hadjihosseini, J.Peinke, and N.P.Hoffmann, Stochastic analysis of ocean wave states with and without rogue waves, *New Journal of Physics* **16**, 053037 (2014).

[132] A.Hadjihosseini, M.Wachter, N.P.Hoffmann, and J.Peinke, Capturing rogue waves by multi-point statistics, *New Journal of Physics* **18**, 013017 (2016).

[133] K.Hammani, B.Kibler, C.Finot and A.Picozzi, Emergence of rogue waves from optical turbulence. *Phys. Lett. A* **374**, 3585 (2010).

[134] S.Haver, A possible freak wave event measured at the Draupner Jacket January 1 1995, *Proceedings of Rogue Waves*, edited by M. Olagnon and M. Prevosto, Brest, France (Institut francais de recherche pour l'exploitation de la mer (IFREMER), Brest, 2004).

[135] S.Haver and D.Karunakaran, Probabilistic description of crest heights of ocean waves, *Proceedings of the 5th International Workshop of Wave Hindcasting and Forecasting*, Melbourne, FL (Environment Canada, Atmospheric Environment Service, Downsview, Ontario, 1998).

[136] S.W.Hell, R.Schmidt, A.Enger, Diffraction-unlimited three-dimensional optical nanoscopy with opposing lenses, *Nat. Photonics* **3**, 381 (2009).

[137] C.Herzog, S.Aravazhi, A.Guarino, A.Schneider, G.Poberaj, and P.Gnter, Epitaxial K 1- x Na x Ta 0.66 Nb 0.34 O 3 thin films for optical waveguiding applications, *JOSA B 24*, 829 (2007).

[138] C.M.Heyl *et al.*, Scale-invariant nonlinear optics in gases, *Optica* **3**, 75 (2016).

[139] M.A.Hoefer, M.J.Ablowitz, I.Coddington, E.A.Cirnell, P.Engels, and V.Schweikhard, Dispersive and classical shock waves in Bose-Einstein condensates and in gas dynamics, *Phys. Rev. A* **74**, 023623 (2006).

[140] R.Hohmann, U.Kuhl, H.-J.Stickmann, L.Kaplan, and E.J.Heller, Freak waves in the linear regime: a microwave study, *Phys. Rev. Lett.* **104**, 093901 (2010).

[141] H.Ilan and A.J.Agranat, Electrically controlled absorption in a slab waveguide formed by the implantation of protons in a potassium lithium tantalate niobate substrate, *Appl. Phys. Lett.* **101**, 261101 (2012).

[142] T.Imai, S.Toyoda, J.Miyazu, J.Kobayashi and S.Kojima, Changes in permittivity of KTa1-xNbxO3 crystals induced by electron injection in relation to nonlinear dielectric response, *Appl. Phys. Express* **7**, 071501 (2014).

[143] P.B.Ishai, C.E.M de Oliveira, Y.Ryabov, Y.Feldman, and A.J.Agranat, Glass-forming liquid kinetics manifested in a KTN:Cu crystal, *Phys. Rev. B* **70**, 132104 (2004).

[144] P.B.Ishai, A.J.Agranat, and Y.Feldman, Confinement kinetics in a KTN:Cu crystal: experiment and theory. *Phys. Rev. B* **73**, 104104 (2006).

[145] R.L.Jin, Y.H.Yu, H.Yang, F.Zhu, Q.D.Chen, M.B.Yi, and H.B.Sun, Anomalous Electro-Optic Effect in Polar Liquid Films, *IEEE J. Quant. Electron.* **48**, 1310 (2012).

[146] Y.V.Kartashov, B.A.Malomed and L.Torner, Solitons in nonlinear lattices *Rev. Mod. Phys.*, **83**, 247 (2011).

[147] S.Kawata, Y.Inouye, P.Verma, Plasmonics for near-field nano-imaging and superlensing, *Nat. Photonics* **3**, 388 (2009).

[148] Y.S.Kivshar and G.Agrawal, *Optical solitons: from fibers to photonic crystals*, Academic press, 2003.

[149] Y.S.Kivshar and D.E.Pelinovsky, Self-focusing and transverse instabilities of solitary waves, *Physics Reports* **331**, 117 (2000).

[150] C.Kharif, E.Pelinovsky, and A.Slunyaev, *Rogue Waves in the Ocean*, Springer Verlag, 2009.

[151] W. Kleemann, Relaxor ferroelectrics: Cluster glass ground state via random fields and random bonds, *Phys. Status Solidi B* 1-10 (2014).

[152] L.A.Knauss, R.Pattnaik, and J.Toulouse, Polarization dynamics in the mixed ferroelectric KTa1-xNbxO3, *Phys. Rev. B* **55**, 3472 (1997).

[153] H.Kogelnik, Coupled wave theory for thick hologram gratings, *Bell System Technical Journal* **48**, 2909 (1969).

[154] A.B.Kounga, T.Granzow, E.Aulbach, M.Hinterstein and J.Rödel, High-temperature poling of ferroelectrics, *J. App. Phys.* **107**, 024116 (2008).

[155] H.Kosaka, T.Kawashima, A.Tomita, M.Notomi, T.Tamamura, T.Sato, and S.Kawakami, Self-collimating phenomena in photonic crystals, *Appl. Phys Lett.* **74**, 1212 (1999).

[156] A.J.Kovacs, Glass transition in amorphous polymers: a phenomenological study, *Adv. Polym. Sci.* **3**, 394 (1963).

[157] N.Kukhtarev, Kinetics of hologram recording and erasure in electrooptic crystals, *Sov. Tech. Phys. Lett.* **2**, 438 (1976).

[158] Z. Kutnjak, R. Blinc, and J.Petzelt, The giant electromechanical response in ferroelectric relaxors as a critical phenomenon, *Nature* **441**, 956 (2006).

[159] L.D.Landau and E.M.Lifshitz, *Fluid Mechanics*, Pergamon, 2nd edn (1987).

[160] J.Laurie, U.Bortolozzo, S.Nazarenko and S.Residori, One-dimensional optical wave turbulence: Experiment and theory, *Phys. Rep.* **514**, 121 (2012).

[161] C.Lecaplain, Ph.Grelu, J.M.Soto-Crespo and N.Akhmediev, Dissipative RogueWaves Generated by Chaotic Pulse Bunching in a Mode-Locked Laser, *Phys. Rev. Lett.* **108**, 233901 (2012).

[162] H.N.Lee, H.M.Christen, M.F.Chisholm, C.M.Rouleau and D.H.Lowndes, Strong polarization enhancement in asymmetric three-component ferroelectric superlattices, *Nature* **433**, 395 (2005).

[163] M.Leonetti and C.Conti, Observation of three dimensional optical rogue waves through obstacles, *Appl. Phys. Lett.* **106**, 254103 (2015).

[164] M.Leonetti, S.Karbasi, A.Mafi, and C.Conti, Light focusing in the Anderson regime, *Nat. Commun.* **5**, 4534 (2014).

[165] L.Leuzzi and T.M.Nieuwenhuizen, *Thermodynamics of the Glassy State*, Taylor and Francis, 2008.

[166] B.L.Li, X.P.Liu, F.Fang, J.L.Zhu and J.M.Liu, Monte Carlo simulation of ferroelectric domain growth, *Phys. Rev. B* **73**, 014107 (2006).

[167] Y.L.Li, S.Y.Hu, Z.K.Liu, and L.Q.Chen, Phase-field model of domain structures in ferroelectric thin films, *Appl. Phys. Lett.* **78**, 3878 (2001).

[168] Q.Li, Y.Cao, P.Yu, R.K.Vasudevan, N.Laanait, A.Tselev, N.Balke, F.Xue, L.Q.Chen, P.Maksymovych, S.V.Kalinin and N.Balke, Giant elastic tunability in strained BiFeO3 near an electrically induced phase transition, *Nature Commun.* **6**, (2015).

[169] Y.Linzon, R.Morandotti, M.Volatier, V.Aimez, R.Ares, and S.Bar-Ad, Nonlinear scattering and trapping by local photonic potentials, *Phys. Rev. Lett.* **99**, 133901 (2007).

[170] C.Liu, R.E.C.van derWel, N.Rotenberg, L.Kuipers, T.F.Krauss, A.Di Falco and A.Fratalocchi, Triggering extreme events at the nanoscale in photonic seas, *Nat. Physics* **11**, 358 (2015).

[171] Z.Liu, X.Zhang, Y.Mao, Y.Y.Zhu, Z.Yang, C.T.Chan, and P.Sheng, Locally Resonant Sonic Materials, *Science* **289**, 1734 (2000).

[172] C.Lou, X.Wang, J.Xu, Z.Chen and J.Yang, Nonlinear Spectrum Reshaping and Gap-Soliton-Train Trapping in Optically Induced Photonic Structures, *Phys. Rev. Lett.* **98**, 213903 (2007).

[173] E.Louvergneaux, V.Odent, M.I.Kolobov and M.Taki, Statistical analysis of spatial frequency supercontinuum in pattern forming feedback systems, *Phys. Rev. A* **87**, 063802 (2013).

[174] Q.Lu, J.Han, H.Dai, B.Ge, and S.Zhao, Visualization of Spatial-Temporal Evolution of Light-Induced Refractive Index in Mn: Fe: KTN Co-Doped Crystal Based on Digital Holographic Interferometry, *IEEE Phot. J.* **7**, 1 (2015).

[175] T.T.A.Lummen *et al.*, Thermotropic phase boundaries in classic ferroelectrics, *Nat. Commun.* **5**, 3172 (2014).

[176] P.M.Lushnikov and N.Vladimirova, Non-Gaussian statistics of multiple filamentation, *Opt. Lett.* **35**, 1965 (2010).

[177] D.Majus, V.Jukna, G.Valiulis, D.Faccio, and A.Dubietis, Spatiotemporal rogue events in femtosecond filamentation, *Phys. Rev. A* **83**, 2 (2011).

[178] A.V.Mamaev, M.Saffman, D.Z.Anderson and A.A.Zozulya, Propagation of light beams in anisotropic nonlinear media: From symmetry breaking to spatial turbulence, *Phys. Rev. A* **54**, 870 (1996)

[179] A.V.Mamaev, M.Saffman and A.A.Zozulya, Break-up of two-dimensional bright spatial solitons due to transverse modulation instability, *Europhys. Lett.* **35**, 25 (1996).

[180] D.Mandelik, H.S.Eisenberg, Y.Silberberg, R.Morandotti and J.S.Aitchison, Band-Gap Structure of Waveguide Arrays and Excitation of Floquet-Bloch Solitons, *Phys. Rev. Lett.* **90**, 053902 (2003).

[181] D.Mandelik, R.Morandotti, J.S.Aitchison and Y.Silberberg, Gap Solitons in Waveguide Arrays, *Phys. Rev. Lett.* **92**, 093904 (2004).

[182] F.Mandl, *Quantum field theory*, Wiley, 1984.

[183] M.E.Manley, J.W.Lynn, D.L.Abernathy, E.D.Specht, O.Delaire, A.R.Bishop, R.Sahul, and J.D.Budai, Phonon localization drives polar nanoregions in a relaxor ferroelectric, *Nature Commun.* **5**, 3683 (2014).

[184] N.Marsal, V.Caullet, D.Wolfersberger and M.Sciamanna, Spatial rogue waves in a photorefractive pattern-forming system, *Opt. Lett.* **39**, 3690 (2014).

[185] N.Marsal, D.Wolfersberger, M.Sciamanna and G.Montemezzani, Noise- and dynamics-sustained patterns in a nonlinear photorefractive system, *Phys. Rev. A* **81**, 031804(R) (2010).

[186] A.Mathis, L.Froehly, S.Toenger, F.Dias, G.Genty, and J.M.Dudley, Caustics and Rogue Waves in an Optical Sea, *Sci. Rep.* **5**, 12822 (2015).

[187] J.M.Medina and J.A.Diaz, Extreme reaction times determine fluctuation scaling in human color vision, *Physica A* **461**, 125 (2016).

[188] M.Mitchell, M.Segev, T.H.Coskun, and D.N.Christodoulides, Theory of self-trapped spatially incoherent light beams, *Phys. Rev. Lett.* **79**, 4990 (1997).

[189] M.Mitchell, Z.Chen, M.F.Shih, and M.Segev, Self-trapping of partially spatially incoherent light, *Phys. Rev. Lett.* **77**, 490 (1996).

[190] F.Mitschke, G.Steinmeyer and A.Schwache, Generation of one-dimensional optical turbulence, *Physica D: Nonlinear Phenomena* **96**, 251-258 (1996).

[191] A.Montina, U.Bortolozzo, S.Residori and F.T.Arecchi, Non-Gaussian Statistics and Extreme Waves in a Nonlinear Optical Cavity, *Phys. Rev. Lett.* **103**, 173901 (2009).

[192] J.Mork, B.Tromborg, and J.Mark, Chaos in semiconductor lasers with optical feedback: theory and experiment, *IEEE J. Quant. Electron* **28**, 93-108 (1992).

[193] S.Mossa and F.Sciortino, Crossover (or Kovacs) effect in an aging molecular liquid, *Phys. Rev. Lett.* **92**, 045504 (2004).

[194] A.Mussot, A.Kudlinski, M.Kolobov, E.Louvergneaux, M.Douay, and M.Taki, Observation of extreme temporal events in CW-pumped supercontinuum, *Opt. Express* **17**, 17010 (2009).

[195] S.Nazarenko, *Wave Trubulence*, *Lecture Notes in Physics* **825**, Springer, 2011.

[196] S.Nemoto, Nonparaxial Gaussian beams, *Appl. Opt.* **29**, 1940 (1990).

[197] D.Neshev, E.Ostrovskaya, Y.Kivshar and W.Krolikowski, Spatial solitons in optically induced gratings, *Opt. Lett.* **28**, 710 (2003).

[198] C.E.M.de Oliveira, G.Orr, N.Axelrold and A.J.Agranat, Controlled composition modulation in potassium lithium tantalate niobate crystals grown by off centered TSSG method, *J. Cryst. Growth.* **273**, 203 (2004).

[199] M.Onorato, S.Residori, U.Bortolozzo, A.Montina, F.T.Arecchi, Rogue waves and their generating mechanisms in different physical contexts, *Phys. Reports* **528**, 47 (2013).

[200] M.Onorato, A.Osborne, M.Serio, and S.Bertone, Freak wave in random oceanic sea states, *Phys. Rev. Lett.* **86**, 5831 (2001).

[201] M.Onorato, et al., Statistical properties of directional ocean waves: the role of the modulational instability in the formation of extreme events, *Phys. Rev. Lett.* **102**, 114502 (2009)

[202] G.-L.Oppo, A.M.Yao and D.Cuozzo, Self-organization, pattern formation, cavity solitons, and rogue waves in singly resonant optical parametric oscillators, *Phys. Rev. A* **88**, 043813 (2013).

[203] C.J.Gibson, A.M.Yao, and G.L.Oppo, Optical Rogue Waves in Vortex Turbulence, *Phys. Rev. Lett.* **116**, 043903 (2016).

[204] G.Parisi, *Statistical field theory*, New York: Addison-Wesley (1988).

[205] J.H.Park *et al.*, Subwavelength light focusing using random nanoparticles, *Nat. Photon.* **7**, 454 (2013).

[206] J.Parravicini, F.Di Mei, C.Conti, A.J.Agranat, E.DelRe, Diffraction cancellation over multiple wavelengths in photorefractive dipolar glasses, *Opt. Express* **19**, 24109 (2011).

[207] J.Parravicini, A.J. Agranat, C. Conti, and E. DelRe, Equalizing disordered ferro-electrics for diffraction cancellation,*Appl. Phys. Lett.* **101**, 111104 (2012).

[208] J.Parravicini, D.Pierangeli, F.Di Mei, C.Conti, A.J.Agranat, and E.DelRe, Aging solitons in photorefractive dipolar glasses, *Opt. Express* **21**, 30573 (2013).

[209] J.Parravicini, E.DelRe, A.J.Agranat, and G.Parravicini, Macroscopic response and directional disorder dynamics in chemically substituted ferroelectrics, *Phys. Rev. B* **93**, 094203 (2016).

[210] J.Parravicini, F.Di Mei, R.M.Lorente, D.Pierangeli, A.J.Agranat and E.DelRe, Volume integrated phase-modulator based on funnel waveguides for reconfigurable miniaturized optical circuits, *Opt. Lett.* **40**, 1386 (2015).

[211] R.Pattnaik and J.Toulouse, New Dielectric Resonances in Mesoscopic Ferroelectrics, *Phys. Rev. Lett.* **79**, 4677 (1997).

[212] M.Peccianti, A.Dyadyusha, M.Kaczmarek, and G.Assanto, Escaping solitons from a trapping potential, *Phys. Rev. Lett.* **101**, 153902 (2008).

[213] J.B.Pendry, Negative refraction makes a perfect lens, *Phys. Rev. Lett.* **85**, 3966 (2000).

[214] D.Phelan, C.Stock, J.A.Rodriguez-Rivera, S.Chi, J.Leao, X.Long, Y.Xie, A.A.Bokov, Z.Ye, P.Ganeshe, and P.M.Gehring, The role of random electric fields in relaxors, *PNAS* **111**, 1754 (2014).

[215] A.Picozzi, J.Garnier, T.Hansson, P.Suret, S.Randoux, G.Millot and D.N. Christodoulides, Optical wave turbulence: Towards a unified nonequilibrium ther-modynamic formulation of statistical nonlinear optics, *Physics Reports* **542**, 1-132 (2014).

[216] D.Pierangeli, J.Parravicini, F.DiMei, GB.Parravicini, A.J.Agranat, and E.DelRe, Photorefractive light needles in glassy nanodisordered KNTN, *Opt. Lett.* **39**, 1657 (2014).

[217] D.Pierangeli, M.Flammini, F.Di Mei, J.Parravicini, C.E.M.de Oliveira, A.J.Agranat, and E.DelRe, Continuous solitons in a lattice nonlinearity, *Phys. Rev. Lett.* **114**, 203901 (2015).

[218] D.Pierangeli, F.Di Mei, J.Parravicini, GB.Parravicini, A.J.Agranat, C.Conti and E.DelRe, Observation of an intrinsic nonlinearity in the electro-optic response of freezing relaxors ferroelectrics, *Opt. Mat. Express* **4**, 1487 (2014).

[219] D.Pierangeli, M.Ferraro, F.Di Mei, G.Di Domenico, C.E.M.de Oliveira, A.J.Agranat and E.DelRe, Super-crystals in composite ferroelectrics, *Nat. Commun* **7**, 10674 (2016).

[220] D.Pierangeli, F.DiMei, C.Conti, A.J.Agranat and E.DelRe, Spatial Rogue Waves in Photorefractive Ferroelectrics, *Phys. Rev. Lett.*, **115** 093901 (2015).

[221] D.Pierangeli, F.Di Mei, C.Conti, and E.DelRe, Evidence of the universal dynamics of rogue waves, arXiv preprint arXiv:1511.01390 (2015).

[222] D.Pierangeli, F.Di Mei, G.Di Domenico, A.J.Agranat, C.Conti and E.DelRe, Turbulent transitions in optical wave propagation, *Phys. Rev. Lett.* **117**, 183902 (2016).

[223] D.Pierangeli, G.Musarra, F.Di Mei, G.Di Domenico, A.J.Agranat, C.Conti, and E.DelRe, Enhancing optical extreme events through input wave disorder, ***Phys. Rev. A*** **94**, 063833 (2016).

[224] R.Pirc and R.Blinc, Vogel-Fulcher freezing in relaxor ferroelectrics, *Phys. Rev. B* **76**, 020101(R) (2007).

[225] R.Pirc and Z.Kutnjak, Electric-field dependent freezing in relaxor ferroelectrics, *Phys. Rev. B* **89**, 184110 (2014).

[226] A.N.Pisarchik, R.Jaimes-Reategui, R. Sevilla-Escoboza, G.Huerta-Cuellar and M.Taki, Rogue Waves in a Multistable System, *Phys. Rev. Lett.* **107**, 274101 (2011).

[227] D.A.Powell, I.V.Shadrivov, and Y.S.Kivshar, Nonlinear electric metamaterials, *Appl. Phys. Lett.* **95**, 084102 (2009).

[228] S.Prosandeev, D.Wang, A.R.Akbarzadeh, B.Dkhil, and L.Bellaiche, Field-induced percolation of polar nanoregions in relaxor ferroelectrics, *Phys. Rev. Lett.* **110**, 207601 (2013).

[229] A.Pugachev *et al.*, Broken local symmetry in paraelectric BaTiO3 proved by second harmonic generation, *Phys. Rev. Lett.* **108**, 247601 (2012).

[230] K.M.Rabe, C.H.Ahn and J.M.Triscone, Physics of ferroelectrics: a modern perspective, *Springer Science & Business Media*, Vol. 105 (2007).

[231] M.M.Rahaman, T.Imai, T.Sakamoto, S.Tsukada, and S.Kojima, Fano resonance of Li-doped KTa1-xNbxO3 single crystals studied by Raman scattering, *Sci. Rep.* **6**, 23898 (2016).

[232] G.N.Ramachandran, Advanced Methods of Crystallography, *Academic Press*, (1964).

[233] S.Randoux, P.Walczak, M.Onorato, and P.Suret, Intermittency in Integrable Turbulence, *Phys. Rev. Lett.* **113**, 113902 (2014).

[234] S.Randoux, P.Walczak, M.Onorato and P.Suret, Nonlinear random optical waves: Integrable turbulence, rogue waves and intermittency, *Physica D: Nonlinear Phenomena* , doi:10.1016/j.physd.2016.04.001 (2016).

[235] V.Roppo *et al.*, The role of ferroelectric domain structure in second harmonic generation in random quadratic media, *Opt. Express* **18**, 4012 (2010).

[236] D.Ruelle, Deterministic chaos: the science and the fiction, *Proc. R. Soc. London Ser. A, Math. Phys. Sci.* **427**, 241 (1990).

[237] Y.Saito and H.Takao, High Performance Lead-free Piezoelectric Ceramics in the (K,Na)NbO3-LiTaO3 Solid Solution System, *Ferroelectrics* **338**, 17-32 (2006).

[238] H.Sakaguchi and B.A.Malomed, Dynamics of positive- and negative-mass solitons in optical lattices and inverted traps, *J. Phys. B* **37**, 1443 (2004).

[239] T.Sakamoto, M.Sasaura, S.Yagi, K.Fujiura and Y.Cho, In-Plane Distribution of Phase Transition Temperature of KTa1-xNbxO3 Measured with Single Temperature Sweep, *Appl. Phys. Express* **1**, 101601 (2008).

[240] G.Samara, The relaxational properties of compositionally disordered ABO$_3$ perovskites, *J.Phys.:Condens.Matter* **15**, R367 (2003).

[241] M.Sano and K.Tamai, A universal transition to turbulence in channel flow, *Nature Phys.* **12**, 249253 (2016).

[242] N.Sapiens, A.Weissbrod, and A.J. Agranat, Fast electroholographic switching, *Opt. Lett.* **34**, 353 (2009).

[243] T.Schreiber and A.Schmitz, Improved Surrogate Data for Nonlinearity Tests, *Phys. Rev. Lett.* **77**, 635 (1996).

[244] T.Schreiber, Constrained Randomization of Time Series Data, *Phys. Rev. Lett.* **80**, 2105 (1998).

[245] M.Segev, B.Crosignani, A.Yariv, and B.Fischer, Spatial solitons in photorefractive media, *Phys. Rev. Lett.* **68**, 923 (1992).

[246] M.Segev and A.J.Agranat, Spatial solitons in centrosymmetric photorefractive media, *Opt. Lett.* **22**, 1299 (1997).

[247] M.Segev, B.Crosignani, P.Di Porto, A.Yariv, G.Duree, G.Salamo, and E.Sharp, Stability of photorefractive spatial solitons, *Opt. Lett.* **19**, 1296 (1994).

[248] M.Segev, G.C.Valley, B.Crosignani, P.DiPorto, and A.Yariv, Steady-state spatial screening solitons in photorefractive materials with external applied field, *Phys. Rev. Lett.* **73**, 3211 (1994).

[249] M.Segev, Y.Silberberg, and D.N.Christodoulides, Anderson localization of light, *Nat. Photonics* **7**, 197 (2013).

[250] F.Selmi, S.Coulibaly, Z.Loghmari, I.Sagnes, G.Beaudoin, M.G.Clerc, and S.Barbay, Spatiotemporal chaos induces extreme events in an extended microcavity laser, *Phys. Rev. Lett.* **116**, 013901 (2016).

[251] V.M.Shalaev, Optical negative-index metamaterials, *Nat. Photon.* **1**, 41 (2007).

[252] M.Shats, H.Punzmann and H.Xia, Capillary rogue waves, *Phys. Rev. Lett.* **104**, 104503 (2010).

[253] F.W.Sheu and M.F.Shih, Spatial coherence of an optical turbulent beam in a biased photorefractive crystal due to the spatiotemporal modulation instability, *Optics communication* **278**, 187 (2007).

[254] M.F.Shih, C.C.Jeng, F.W.Sheu and C.Y.Lin, Spatiotemporal optical modulation instability of coherent light in noninstantaneous nonlinear media, *Phys. Rev. Lett.* **88**, 133902 (2002).

[255] A.V.Shorokhov, M.A.Pyataev, N.N.Khvastunov, T.Hyart, F.V.Kusmartsev, and K.N.Alekseev, Physical principles of the amplification of electromagnetic radiation due to negative electron masses in a semiconductor superlattice, *JETP Lett.* **100**, 766 (2015).

[256] V.V.Shvartsman and D.C.Lupascu, Lead-Free Relaxor Ferroelectrics, *J. Am. Ceram. Soc.* **95**, 1-26 (2012).

[257] L.A.Smith, Intrinsic limits on dimension calculations, *Phys. Lett. A* **133**, 283 (1988).

[258] D.R.Solli, C.Ropers, P.Koonath1 and B.Jalali, Optical rogue waves, *Nature* **450**, 1054 (2007).

[259] D.R.Solli, C.Ropers and B.Jalali, Rare frustration of optical supercontinuum generation, *Appl. Phys. Lett.* **96**, 151108 (2010).

[260] D.R.Solli, G.Herink, B.Jalali and C.Ropers, Fluctuations and correlations in modulation instability, *Nat. Photonics* **6**, 463 (2012).

[261] D.R.Solli, C.Ropers, and B.Jalali, Active Control of RogueWaves for Stimulated Supercontinuum Generation, *Phys. Rev. Lett.* **101**, 233902 (2008).

[262] L.Solymar, D.J.Webb and A.Grunnet-Jepsen, *The physics and applications of photorefractive materials*, Oxford University Press, (1996).

[263] J.M.Soto-Crespo, N.Devine, and N. Akhmediev, Integrable Turbulence and Rogue Waves: Breathers or Solitons?, *Phys. Rev. Lett.* **116**, 103901 (2016).

[264] K.Staliunas and R.Herrero, Nondiffractive propagation of light in photonic crystals, *Phys. Rev. E* **73**, 016601 (2006).

[265] G.Stone *et al.*, Atomic scale imaging of competing polar states in a RuddlesdenPopper layered oxide, *Nat. Commun.* **7**, 12572 (2016).

[266] C.Sun, S.Jia, C.Barsi, S.Rica, A.Picozzi and J.W.Fleischer, Observation of the kinetic condensation of classical waves, *Nat. Phys.* **8**, 470 (2012).

[267] P.Suret, R.El Koussaifi, A.Tikan, C.Evain, S.Randoux, C.Szwaj, and S.Bielawski, Single-shot observation of optical rogue waves in integrable turbulence using time microscopy, *Nat. Commun.* **7**, 13136 (2016).

[268] J.Theiler, S.Eubank, A.Longtin, B.Galdrikian, and J.D.Farmer, Testing for nonlinearity in time series: The method of surrogate data, *Physica D* **58**, 77 (1992).

[269] H.Tian, B.Yao, C.Hu, X.Meng, and Z.Zhou, Impact of polar nanoregions on the quadratic electro-optic effect in K0.95Na0.05Ta1xNbxO3 crystals near the Curie temperature, *Appl. Phys. Express* **7**, 062601 (2014).

[270] H.Tian, B.Yao, P.Tan, Z.Zhou, G.Shi, D.Gong and R.Zhang, Double-loop hysteresis in tetragonal $KTa_{0.58}Nb_{0.42}O_3$ correlated to recoverable reorientations of the asymmetric polar domains, *Appl. Phys. Lett.* **106**, 102903 (2015).

[271] H.Tian, B.Yao, L.Wang, P.Tan, X.Meng, G.Shi and Z.Zhou, Dynamic response of polar nanoregions under an electric field in a paraelectric KTa0.61Nb0.39O3 single crystal near the para-ferroelectric phase boundary, *Sci. Rep.* **5**, 13751 (2015).

[272] H.Tian, X.Meng, C.Hu, P.Tan, X.Cao, G.Shi, Z.Zhou, and R.Zhang, Origin of giant piezoelectric effect in lead-free K1-xNaxTa1-yNbyO3 single crystals, *Sci. Rep.* **6**, 25637 (2016).

[273] H.Tian, P.Tan, X.Meng, C.Hu, B.Yao, G.Shi, and Z.Zhou, Variable gradient refractive index engineering: design, growth and electro-deflective application of KTa1-xNbxO3, *Journal of Materials Chemistry C* **3**, 10968 (2015).

[274] M.Tlidi, Y.Gandica, G.Sonnino, E.Averlant, and K.Panajotov, Self-Replicating Spots in the Brusselator Model and Extreme Events in the One-Dimensional Case with Delay, *Entropy* **18**, 64 (2016).

[275] S.Toenger, T.Godin, C.Billet, F.Dias, M.Erkintalo, G.Genty, and J.M.Dudley, Emergent rogue wave structures and statistics in spontaneous modulation instability, *Sci. Rep.* **5**, 0380 (2016).

[276] J.Toulouse, P.DiAntonio, B.E.Vugmeister, X.M.Wang, L.A.Knauss, Precursor effects and ferroelectric macroregions in KTa1-xNbxO3 and K1-yLiyTaO3, *Phys. Rev. Lett.* **68**, 232 (1992).

[277] S.Trillo and W.Torruellas (Eds.), *Spatial Solitons*, Springer, Berlin, 2001.

[278] J.Trull *et al.*, Second-harmonic parametric scattering in ferroelectric crystals with disordered nonlinear domain structures, *Opt. Express* **15**, 15868 (2007).

[279] S.K.Turitsyn, S.A.Babin, E.G.Turitsyna, G.E.Falkovich, E.V.Podivilov and D.V.Churkin, Optical wave turbulence, *Advances in Wave Turbulence* **83**, 113 (2013).

[280] E.G.Turitsyna, S.V.Smirnov, S.Sugavanam, N.Tarasov, X.Shu, S.A.Babin, E.V.Podivilov, D.V.Churkin, G.Falkovich, S.K.Turitsyn, The laminar-turbulent transition in a fibre laser, *Nature Photon.* **7**, 783-786 (2013).

[281] J.Van Roey, J.Van der Donk, and P.E.Lagasse, Beam-propagation method: analysis and assessment, *JOSA* **71**, 803 (1981).

[282] S.Vergeles and S.K.Turitsyn, Optical rogue waves in telecommunication data streams, *Phys. Rev. A* **83**, 061801(R) (2011).

[283] X.Vidal and J.Martorell, Generation of Light in Media with a Random Distribution of Nonlinear Domains, *Phys. Rev. Lett.* **97**, 013902 (2006).

[284] D.Viehland, M.Wuttig, and L.E.Cross, The glassy behavior of relaxor ferroelectrics, *Ferroelectrics* **120**, 71 (1991).

[285] D.Viehland, S.J.Jang, L.E.Cross, and M.Wuttig, Freezing of the polarization fluctuations in lead magnesium niobate relaxors, *J. Appl. Phys.* **68**, 2916 (1990).

[286] D.Viehland, J.F.Li, S.Jang, M.Wuttig, and L.E.Cross, Dipolar-glass model for lead magnesium niobate, *Phys. Rev. B* **43**, 8316 (1991).

[287] D.Viehland, S.J.Jang, L.E.Cross, and M.Wuttig, Deviation from Curie-Weiss behavior in relaxor ferroelectrics, *Phys. Rev. B* **46**, 8003 (1992).

[288] B.E.Vugmeister and H.Rabitz, Kinetics of electric-field-induced ferroelectric phase transitions in relaxor ferroelectrics, *Phys. Rev. B* **65**, 024111 (2001).

[289] S.Wabnitz, Optical turbulence in fiber lasers, *Opt. Lett.* **39**, 1362 (2014).

[290] P.Walczak, S.Randoux and P.Suret, Optical rogue waves in integrable turbulence, *Phys. Rev. Lett.* **114**, 143903 (2015).

[291] W.Wan, S.Jia, and J.W.Fleischer, Dispersive superfluid-like shock waves in nonlinear optics, *Nature Phys.* **3**, 46 (2007).

[292] L.Wang, H.Tian, X.Meng, H.Chen, Z.Zhou, and Y.Shen, Field-induced enhancement of voltage-controlled diffractive properties in paraelectric iron and manganese co-doped potassium-tantalate-niobate crystal, *Appl. Phys. Express* **7**, 112601 (2014).

[293] Q.Wang, E.T.Rogers, B.Gholipour, C.M.Wang, G.Yuan, J.Teng, and N.I.Zheludev, Optically reconfigurable metasurfaces and photonic devices based on phase change materials,*Nat. Photon.* **10**, 60 (2016).

[294] M.F.Weber, C.A.Stover, L.R.Gilbert, T.J.Nevitt and A.J.Ouderkirk, Giant birefringent optics in multilayer polymer mirrors, *Science* **287**, 2451 (2000).

[295] S.H.Wemple and M.DiDomenico, Oxygen-Octahedra Ferroelectrics. II. Electro-optical and Nonlinear-Optical Device Applications, *J. Appl. Phys.* **40**, 735-752 (1969).

[296] G.B.Whitham, *Linear and Nonlinear Waves*, Wiley, 1974.

[297] M.Wimmer, A.Regensburger, C.Bersch, M.A.Miri, S.Batz, G.Onishchukov, D.N.Christodoulides and U.Peschel, Optical diametric drive acceleration through actionreaction symmetry breaking, *Nature Phys.* **9**, 780 (2013).

[298] M.Wuttig and N.Yamada,Phase-change materials for rewriteable data storage, *Nat. Materi.* **6**, 824 (2007).

[299] G.Xu, Z.Zhong, Y.Bing, Z.-G.Ye, and G.Shirane, Electric-field-induced redistribution of polar nano-regions in a relaxor ferroelectric, *Nat. Materials* **5**, 134 (2006).

[300] G.Xu, J.Wen, C.Stock, and P.M.Gehring, Phase instability induced by polar nanoregions in a relaxor ferroelectric system, *Nat. Materials* **7**, 562 (2008).

[301] G.Xu, D.Vocke, D.Faccio, J.Garnier, T.Roger, S.Trillo, and A. Picozzi, From coherent shocklets to giant collective incoherent shock waves in nonlocal turbulent flows, *Nat. Commun.* **6**, 8131 (2015).

[302] A.Yariv and P.Yeh, *Optical Waves in Crystals* Wiley, New York, 1984.

[303] S.Yao, X.Zhou and G.Hu, Experimental study on negative effective mass in a 1D mass spring system, *New J. Phys.* **10**, 43020 (2008).

[304] P.Yeh, *Introduction to photorefractive nonlinear optics*, Wiley, New York, 1993.

[305] H.Yokota, Y.Uesu, C.Malibert, and J.M.Kiat, Second-harmonic generation and x-ray diffraction studies of the pretransitional region and polar phase in relaxor K(1-x)LixTaO3, *Phys. Rev. B* **75**, 184113 (2007).

[306] Z.L.Yuan, B.Frhlich, M.Lucamarini, G.L.Roberts, J.F.Dynes, and A.J.Shields, Directly Phase-Modulated Light Source, *Phys. Rev. X* **6**, 031044 (2016).

[307] P.Zalden *et al.* , Picosecond Electric-Field-Induced Threshold Switching in Phase-Change Materials, *Phys. Rev. Lett.* **117**, 067601 (2016).

[308] J.Zamora-Munt, B.Garbin, S.Barland, M.Giudici, J.R.Rios Leite, C.Masoller, and J.R.Tredicce, Rogue waves in optically injected lasers: Origin, predictability, and suppression, *Phys. Rev. A* **87**, 035802 (2013).

[309] P.Zhang, S.Liu, J.Zhao, C.Lou, J.Xu and Z.Chen, Optically induced transition between discrete and gap solitons in a nonconventionally biased photorefractive crystal, *Opt. Lett.* **33**, 878 (2008).

[310] Y.Zhen-Ya, Financial rogue waves, *Commun. Theor. Phys.* **947**, 6 (2010).

[311] W.Zhu, J.H.Chao, C.J.Chen, S.Yin, and R.C.Hoffman, Three order increase in scanning speed of space charge-controlled KTN deflector by eliminating electric field induced phase transition in nanodisordered KTN, *Sci. Rep.* **6**, 33143 (2016).

[312] A.Zozulya and D.Anderson, Nonstationary self-focusing in photorefractive media, *Opt. Lett.* **22**, 837 (1995).